Electronic Thesis and Dissertation Repository

4-19-2016 12:00 AM

Doped TiO2 Nanowires for Applications in Dye Sensitized Solar Cells and Sacrifical Hydrogen Production

Qasem Alsharari
The University of Western Ontario

Supervisor
Dr. Mita Ray
The University of Western Ontario Joint Supervisor
Dr. Paul Charpentier
The University of Western Ontario

Follow this and additional works at: https://ir.lib.uwo.ca/etd

Part of the Catalysis and Reaction Engineering Commons, Engineering Science and Materials Commons, Environmental Sciences Commons, Inorganic Chemistry Commons, Nanoscience and Nanotechnology Commons, and the Semiconductor and Optical Materials Commons

Recommended Citation

Abstract

This thesis explores the synthesis of metal oxide 1-D nanowires using a sol-gel method in supercritical carbon dioxide (sc-CO_2), as an environmental friendly enabling solvent. Porous nanowires were synthesized and their performance was tested in dye sensitized solar cell and sacrifical hydrogen production. Titanium isopropoxide (TIP) was used as a precursor for titania synthesis while copper, bismuth and indium were examined as dopants, respectively. The sol-gel reactions were catalyzed by acetic acid in CO_2 at a temperature of 60 °C and pressure of 5000 psi. It was observed that acetic acid/monomer ratio > 4 produced nanowires while a lower ratio led to the formation of various morphologies, depending on reaction conditions. The synthesized undoped and doped nanowires were characterized by electron microscopy (SEM and TEM), N2 physisorption, FTIR, XRD, XPS, thermal analysis. These results showed high aspect ratio nanowires as observed by SEM (15-25) with surface areas ranging from 40 to 126 m^2/g. These surface areas are comparable and sometimes exceeded the surface area of Degussa P25 (i.e. 50 m^2/g).

Copper doped nanowires were examined as sacrificial photocatalytic catalysts in Chapter 3. It was found that the modified sol-gel synthesis approach in supercritical CO_2 produced primarily a single oxidation state (Cu (I)) of active Cu_2O/TiO_2, which was confirmed by XPS and XANES analyses. Wt % of copper and initial concentration of sacrificial agent were optimized to enhance hydrogen production with the results compared to undoped titanium nanowires and Degussa P25. The Cu_2O/TiO_2 nanowires showed improved hydrogen production at 1 % Cu (I) loading which produced about 10 times more hydrogen than Degussa P25 and 47 times more than undoped nanowires, respectively.

Chapter 4 discusses the synthesis and application of Indium (In) doped titania for DSSCs and sacrificial hydrogen production. Indium has high conductivity, transparency for visible light, and good electron mobility, making it an attractive dopant for such applications.

In Chapter 5, sacrificial hydrogen production by bismuth titanate nanowires using formaldehyde as the sacrificial agent is examined. Bismuth titanate was previously shown theoretically to have all the requirements to be an effective photocatalyst to produce hydrogen when doped with transition metals. However, little experimental work has been

reported on the performance of bismuth titanate nanowires. Bismuth titanate nanowires were synthesized using a sol-gel methodology in supercritical CO_2 with different levels of bismuth loading (1, 1.4, and 2 mol % bismuth). These nanowires were investigated for their sacrificial photocatalytic hydrogen production, which was compared to that of undoped titanium nanowires and P25.

Chapter 6 deals with the experimental results of bismuth titanate, which is known as an active visible light photocatalyst, with most of its applications focused on remediation of water and wastewater. However, very limited applications of bismuth titanate in DSSCs have been reported in the literature. The effect of Bi loading on TiO_2 nanowires for DSSCs was investigated by testing the J-V curves of the solar cells. The influence of Bi on the internal processes of electron transport was also evaluated by electrochemical impedance spectroscopy.

In order to integrate these nanowires into polymeric systems for easy processability and application, the synthesis of polysulfone polymers was examined inChapter 7. These polymers were designed to contain carboxylic functional groups to enable coordination with titanium and titanium doped photocatalyst. The goal was to produce an organic-inorganic membrane for photocatalytic membrane reactor that can reduce fouling by degradation of pollutants. The membrane was also examined to be cast as nanotubes using an anodic aluminum oxide (AAO) template method.

Keywords

Titanium, nanowires, metal oxides, dye sensitized solar cells (DSSC), hydrogen, photocatalyst, copper, indium, bismuth, nanomaterials, solar energy, supercritical, carbon dioxide, sol-gel method.

Co-Authorship Statement

Title: Bismuth Titanate Nanowires as a photoanode for dye sensitized solar cells

Authors: Qasem Alsharari, Paul A. Charpentier, Madhumita Bhowmick Ray

Experimental work and preparation of this manuscript was done by Qasem Alsharari and corrected by Dr. Madhumita B. Ray and Dr. Paul Charpentier. This manuscript is under preparation for publication.

Title: Photocatalytic hydrogen production using active Bismuth titanate nanowires

Authors: Qasem Alsharari, Paul A. Charpentier, Madhumita Bhowmick Ray

All experimental work and preparation of this manuscript were done by Qasem Alsharari and corrected by Dr. Madhumita B. Ray and Dr. Paul Charpentier. This manuscript is under preparation for publication.

Title: Cu_2O /TiO_2 Nanowires using Supercritical CO_2 for Photocatalytic Hydrogen Production

Authors: Qasem Alsharari, Osariemen Ogbeide, Zhiqiang Wang, Tsun-Kong Sham, Paul A. Charpentier, Madhumita Bhowmick Ray

Synthesis and characterizations of nanowires were conducted by Qasem Alsharari, 70% of sacrificial hydrogen experiments were conducted by Qasem Alsharari, and 30 % by Osariemen Ogbeide. XANES analyses were performed at Dr. Tsun-Kong Sham's facilities and interpretations were done by Dr. Zhiqiang Wang. Preparation of this manuscript was done by Qasem Alsharari and corrected by Dr. Madhumita B. Ray and Dr. Paul Charpentier. This manuscript is under preparation for publication.

Acknowledgments

Table of Contents

List of Tables

List of Figures

List of Appendices

Appendix A: copyright releases

Chapter 1

1 Introduction

1.1 Thesis Overview

The worlds increasing demand for energy is being driven by both an exponential increase of population and an increasing standard of living in emerging economies. The world's demand for electricity doubled between 2000 and 2012, while is expected to further increase by 70% by 2040. [1] Yet, almost 550 million people are projected to live without electricity in 2040, requiring new easy methods for harnessing energy which are renewable. The current electricity production is primarily based on non renewable coal, oil, natural gas and nuclear energy, while renewable sources such as wind and solar energy are rapidly growing.[2] Nuclear energy, although it is a relatively low cost source, has significant disadvantages of limited availability, high environmental impact for storing the waste materials while is also considered unsafe. In comparison, photovoltaic technology (PV) is considered an excellent sustainable energy source for our future, as solar energy is both low cost with high availability. Earth receives annually about 100,000 terawatts (TWs) of solar energy, which is more than 10,000 times our global energy demand. Theoretically, the world's energy demand can be met by capturing only about 0.1% of sunlight using PV cells with a conversion efficiency of 10%. [3]

Of the various PV technologies, dye sensitized solar cells (DSSC) are of increasing interest (see Figure 1-1). These are simple devices involving photoelectrochemical principles mimicking the photosynthetic processes in plants to generate electricity using a photosensitizer. These devices capture incident photons from sunlight through organic dye absorption, which generate electrons that are subsequently transported to a semiconductor material, usually TiO_2 nanoparticles. With the help of an electrolyte and counter electrode, the full cycle can be repeated for the duration of solar radiation. These are simple devices involving photoelectrochemical principles mimicking the photosynthetic processes in plants to generate electricity using a photosensitizer. These

devices capture incident photons from sunlight through organic dye absorption, which generate electrons that are transported to a semiconductor material, usually TiO_2 nanoparticles. With the help of an electrolyte and counter electrode, the full cycle can be repeated for the duration of solar radiation.

Transforming materials from bulk to the nanoscale influences materials' chemical and physical properties due to size changes. The nano-size of materials introduces unique properties such as quantum confinement, in which electron-hole pairs are confined to distances less than the Bohr excitation radius of the material.[4] This helps to improve the materials' surface area, optical and electrical properties for enabling either new applications or enhancing efficiencies for existing applications.

Although nanoparticles provide a high surface area for reactions to take place on, for many applications such as solar cells or photocatalytic applications, nanowires are gaining increased attention due to their 1D transport of electrons. This can provide both higher efficiencies and a better understanding of the various individual processes occurring within the DSSC. Not only are high surface areas required for dyes to adsorb, but also photogenerated electrons need to be transported to the transparent conductive oxide (TCO) layer for harvesting electrons while reducing their recombination rate. Nanowires might provide significant advantages by providing a direct electron percolation pathway, while providing a better distribution of dopant metals throughout the nanowire to reduce electron recombination, enhance light scattering, while providing a high surface area to volume ratio. However, the synthesis of nanowires with high aspect ratios, high surface areas, and easy distribution of dopant metals is challenging. Most published methods for preparing nanowires involve corrosive acids, harsh organic solvents, expensive reagents, and high or ultrahigh vacuum systems. The literature indicates an urgent need for a new scalable methodology for the synthesis of nanowires with a high degree of morphology control while utilizing environmentally friendly solvents.

In this work, a sol-gel method was examined to synthesize nanowires in supercritical CO_2 a green enabling solvent which helps in the synthesis procedure by stabilizing

reactant intermediates in the anisotropic growth process. This method enabled the successful synthesis of titanium dioxide nanowires with Cu, Bi, and In doping. Their performance was evaluated in both dye sensitized solar cells and sacrificial hydrogen production, which are of interest for energy production and water purification.

1.2 Dye Sensitized Solar Cells Structure

Since the first report of the dye sensitized solar cell (DSSC) in 1991 by O'Regan and Gratzel, these devices are becoming a promising third generation alternative to what are more generally known as inorganic p-n junction cells. Gratzels group has provided a basic understanding of the processes that govern DSSC's. As shown in Figure 1-1, a typical DSSC device consists of an active nanomaterial semiconductor with wide band gap energy, which is most commonly TiO_2 or a similar material deposited on glass. A thin layer of transparent conductive oxide (TCO) is normally deposited on the glass, followed by sintering. A light sensitive dye is then applied to these nanomaterials on TCO by adsorption of the dye to the surface from a dilute alcohol/organic solvent dye solution. The resulting nanomaterials on the TCO and dye form the photoanode of the DSSC. The sequence of events that takes place at different components of the solar cell during operation is described briefly below. The first and most important step of the DSSC process is light absorption by the dye at the photoanode surface. Attached dye molecules on the nanocrystalline semiconductor absorb incident light, and the excited electrons from the dye molecules are injected into the conduction band of the active nano-crystalline material. These electrons help generate oxidized dye molecules where positive charge is formed at the metal center. Effective injection of these electrons into the nanomaterial layer is a critical step for efficient charge separation. Electrons are then transported to the transparent conductive electrode, then to the external circuit. Excited dye molecules are regenerated by electron donation from iodide/tri-iodide electrolyte, which provides the required electrons to diffuse to the counter electrode. The tri-iodide is regenerated by electrons flowing from the external circuit to the platinum layer on the counter electrode to complete the electrical circuit of the DSSC.

Maximum photovoltage is a critical performance indicator of a DSSC, which is determined by the potential difference between the redox potential level of electrolyte

and the conduction band edge of semiconductor nanomaterials used to form the photoanode. Under illumination, injected electrons in the conduction band will shift the Fermi level of the semiconductor to rise near the edge of the conduction band. This new Fermi level of a cell under equilibrium determines the photo-electrochemical productivity of the DSSC. Selection of a semiconductor with the right conduction band edge, Fermi level, electron mobility, and redox electrolyte to regenerate excited dye and adequate potential are critical for high performance DSSC's.

The semiconductor is the material that provides the surface area for dye adsorption, and must be capable of collecting an electron from the excited dye and transporting it to the transparent conductive oxide of the photoanode. The conduction band edge of the semiconductor material should be more negative (lower level) than the excited dye by at least 0.2-0.3 eV for efficient electron injection from the dye to the conduction band of the semiconductor. The charge generation is proportional to dye concentration, which is related to the surface area of the semiconductor material. Thus, a high surface area increases the number of sites for dye adsorption as the dye adsorbs as a monolayer on the surface of the semiconductor. Furthermore, the semiconductor should be chemically stable in the fabricated dye sensitized solar cell. Porosity of the semiconductor is a critical factor as it provides sufficient contact of the dye and enhances internal light scattering increasing light utilization within the solar cell.
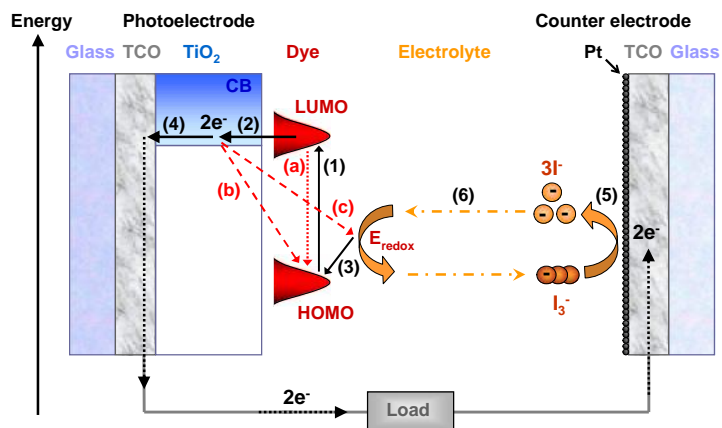
Figure 1-1: DSSC structure and operational principles.[5]

Light harvesting is the driving force in DSSC's as it is the source of photogenerated electrons producing photocurrent. Photoactive dyes such as N719 excite electrons excited from the highest occupied molecular orbital (HOMO) to a higher energy state the lowest unoccupied molecular orbital (LUMO), which should be more positive than nanocrystalline material conduction band edge. Dyes with maximum light absorption in the visible range of sunlight are effective photosensitizers. Organic linkers can be modified to ensure effective linkage to the surface of nanocrystalline semiconductor as monolayer to ensure injection of hot-carriers and regeneration of the excited photosensitizer. For example, N719 [cis-bis (isothiocyanato)-bis(2,2'-bipyridyl-4,4'-dicarboxylato)-ruthenium (11) bis-tetrabutylammonium] is a very efficient Ru based photosensitizers with two carboxylic groups attached to the surface of TiO_2 as shown in Figure 1-2. It absorbs in the visible range of sunlight and injects photogenerated electrons into the semiconductor through a metal to ligand transfer mechanism.
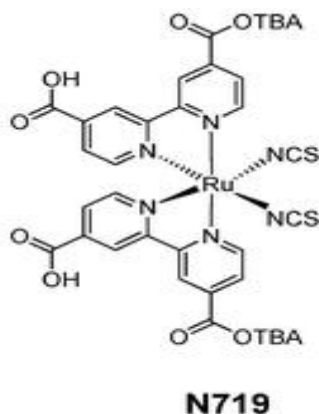
N719

Figure 1-2: Photosensitizer N719.

1.3 Photocatalytic Hydrogen Production

Hydrogen production using sunlight is a promising source of clean renewable energy by splitting water into hydrogen and oxygen. The formed energy can be used directly as a fuel or chemically transformed into different fuels. Water splitting requires a minimum energy of 1.23 eV to activate water for splitting into hydrogen and oxygen, which can be supplied by an external voltage. This can be done by a solar cell to drive the forward reaction of producing hydrogen. Light absorbing catalysts such as TiO_2 are used to

catalyze water splitting, which eliminate the externally applied potential used for electrolysis. The energy gap of TiO_2 is not only larger than 1.23 eV (about 3 eV) but also the conduction band edge is more negative than the water reduction potential and the valance band position is more positive than the oxidation potential of water, i.e., -0.82 V and +0.41 V vs NHE at pH7, respectively. The schematic presented below (Figure 1-3) shows these band positions for TiO_2 nanomaterials with the corresponding oxidation/ reduction potentials for water. [6-8]
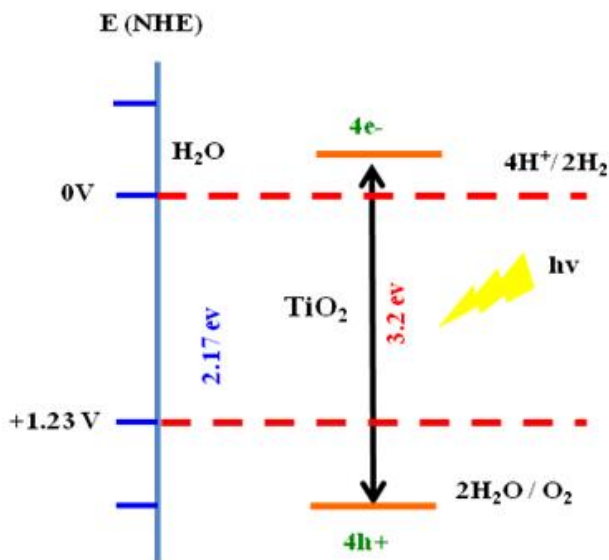
Figure 1-3: Conduction and valence band positions of TiO_2 versus theoretical water redox potentials on NHE scale.

In photocatalytic water splitting, photogenerated electrons migrate to the conduction band, where they reduce H^+ to H_2, and the holes on the surface of semiconductor decompose H_2O to O_2 and H^+. Oxygen needs to be eliminated via purging because it competes with H^+ ions for electrons [9]. However, a sacrificial reagent can be used to control this process as a hole scavenger. [10] Recent studies indicate that sacrificial reagents such as chorophenol, methanol, ethanol, lactic acid, and formaldehyde can prohibit rapid recombination of electron/hole pairs as well as recombination of hydrogen and oxygen. [11] In addition, sacrificial hydrogen production using wastewater also fulfills the dual purposes of water treatment with in-situ hydrogen production from the contaminant (s).

Due to its low splitting energy (16.1 kJ mol^{-1}), previously methanol has been investigated for sacrificial hydrogen generation. [12] However, formaldehyde with lower splitting energy of -48 kJ mol^{-1} compared to methanol is being increasingly used for sacrificial hydrogen production. Formaldehyde is present in several industrial effluents including paint, paper, chemical and petroleum industries as it is an important vital reagent for the manufacture of dyes, glass mirrors, textiles, disinfectants, and resins. [13] The presence of formaldehyde in wastewater treatment plants is detrimental to the bacterial activity, while under UV irradiation and in presence of oxygen, TiO_2 can effectively degrade formaldehyde to CO_2 and water. [14] Therefore, effective reduction of recombination of electron-hole is achieved by the dual actions of removal of electrons by a dopant on surface of TiO_2 and the removal of holes by a sacrificial agent.

1.4 References

1. Association, W.N., *Renewable Energy and Electricity.* 2016.

2. Sorrell, S., *Reducing energy demand: A review of issues, challenges and approaches.* Renewable & Sustainable Energy Reviews, 2015. **47**: p. 74-82.

3. Koberle, A.C., D.E.H.J. Gernaat, and D.P. van Vuuren, *Assessing current and future techno-economic potential of concentrated solar power and photovoltaic electricity generation.* Energy, 2015. **89**: p. 739-756.

4. Vogel, D.J. and D.S. Kilin, *First-Principles Treatment of Photoluminescence in Semiconductors.* Journal of Physical Chemistry C, 2015. **119**(50): p. 27954-27964.

5. Miettunen, K., J. Halme, P. Vahermaa, T. Saukkonen, M. Toivola, and P. Lund, *Dye Solar Cells on ITO-PET Substrate with TiO2 Recombination Blocking Layers.* Journal of The Electrochemical Society, 2009. **156**(8): p. B876-B883.

6. Kang, D., T.W. Kim, S.R. Kubota, A.C. Cardiel, H.G. Cha, and K.S. Choi, *Electrochemical Synthesis of Photoelectrodes and Catalysts for Use in Solar Water Splitting.* Chem Rev, 2015. **115**(23): p. 12839-12887.

7. Krishnappa, M., V.S. Souza, N. Ganganagappa, J.D. Scholten, S.R. Teixeira, J. Dupont, and R. Thippeswamy, *Mesoporous Foam TiO_2 Nanomaterials for Effective Hydrogen Production.* Chemistry, 2015. **21**(49): p. 17624-17630.

8. Ahmed, M.G., I.E. Kretschmer, T.A. Kandiel, A.Y. Ahmed, F.A. Rashwan, and D.W. Bahnemann, *A Facile Surface Passivation of Hematite Photoanodes with TiO_2 Overlayers for Efficient Solar Water Splitting.* ACS Appl Mater Interfaces, 2015. **7**(43): p. 24053-24062.

9. Teets, T.S. and D.G. Nocera, *Photocatalytic hydrogen production.* Chem Commun (Camb), 2011. **47**(33): p. 9268-9274.

10. Abe, R., K. Sayama, and H. Arakawa, *Significant effect of iodide addition on water splitting into H_2 and O_2 over Pt-loaded TiO_2 photocatalyst: suppression of backward reaction.* Chemical Physics Letters, 2003. **371**(3-4): p. 360-364.

11. Ni, M., M.K.H. Leung, D.Y.C. Leung, and K. Sumathy, *A review and recent developments in photocatalytic water-splitting using TiO_2 for hydrogen production.* Renewable & Sustainable Energy Reviews, 2007. **11**(3): p. 401-425.

12. Chowdhury, P., G. Malekshoar, M.B. Ray, J. Zhu, and A.K. Ray, *Sacrificial Hydrogen Generation from Formaldehyde with Pt/TiO_2 Photocatalyst in Solar Radiation.* Industrial & Engineering Chemistry Research, 2013. **52**(14): p. 5023-5029.

13.   Jia, Y.S., S. Shen, D.G. Wang, X. Wang, J.Y. Shi, F.X. Zhang, H.X. Han, and C. Li, *Composite $Sr_2TiO_4/SrTiO_3(La,Cr)$ heterojunction based photocatalyst for hydrogen production under visible light irradiation.* Journal of Materials Chemistry A, 2013. **1**(27): p. 7905-7912.

14.   Akbarzadeh, R., S.B. Umbarkar, R.S. Sonawane, S. Takle, and M.K. Dongare, *Vanadia-titania thin films for photocatalytic degradation of formaldehyde in sunlight.* Applied Catalysis a-General, 2010. **374**(1-2): p. 103-109.

Chapter 2

2 Literature Review

2.1 Nanomaterials and Their Applications

Nanostructured materials have gained significant attention, particularly in the field of photocatalytic applications such as water treatment, industrial wastewater, air purification, self-cleaning surfaces, degradation of organic pollutants, and hydrogen production. Processing traditional materials into nanodimensions increases their chemical and physical characteristics due to a higher surface area per unit volume providing more active sites for reactions.[1] Synthesis of these nanomaterials has opened a new frontier of chemical and physical properties of the materials compared to their bulk properties. As the size of the nanomaterial becomes smaller; electron mobility becomes more restricted, an effect called "quantum confinement". Quantum confinement is exploited in various nanomaterials such as quantum dots, providing new applications for traditional metals such as gold, cadmium, selenium, gallium and indium. Most of these so-called quantum dot materials are used to enhance harvesting of solar light or used as a photocatalyst.[2]

The ability to produce nanomaterials with controlled size and structure is critical in the development of effective and efficient photocatalyic and photo active materials. One of the most widely used photocatalysts is titanium dioxide, TiO_2 or titania, due to its high chemical and thermal stability, wide band gap, low cost, abundance, and nontoxicity. The pioneering work of Fujishima and Honda (1972) for water splitting paved the way for many applications of TiO_2 as the gold standard for photocatalysts. [3]

Titanium dioxide exists in three different phases namely, anatase, rutile, brookite, and TiO_2(B) as shown in Figure 2-1. Reduction in size of these three phases affects their surface defects, refractive index and the charge transfer across their interfaces and their resulting band gap. However, these changes make anatase the most commonly form used as a photocatalyst as it is the least thermodynamically stable in the bulk phase but most stable material with grain size below 13-16 nm and a surface energy of 1.32 Jm^{-2}. [4-6]

The most researched application of titanium dioxide is for the degradation of organic molecules by hydroxyl radicals produced by UVA irradiation. Hydroxyl radical is the second most oxidizing agent, and the amount of hydroxyl radical production is a measure of the photocatalyst efficiency. Upon irradiation with UVA radiation, excited electrons from the valence band of TiO_2 migrate to the conduction band, creating electron-holes on the surface of the photocatalyst, where water reacts to generate hydroxyl radical that degrades organic molecules indiscriminately.[7, 8] The superior photocatalytic properties of nanosize TiO_2 make it a promising and competitive photocatalyst for environmental applications, photo-electrochemical applications, e.g. solar cells and water splitting for hydrogen generation and gas sensors. [9-13]

Although it has many benefits, TiO_2 absorbs only about 5% of available sunlight, i.e. the ultraviolet light that matches it's band gap to generate electrons and hole pairs. Furthermore, the high rate of recombination of photo-generated electron/hole pairs is limiting its future development and efficiency.[14, 15] [16] Many investigations have been conducted to overcome charge recombination and the low efficiency of utilizing solar light. Doping TiO_2 using various noble and transition metals such as Pt, Au, Pd, Rh, Ni, Cu, Ag, etc. greatly reduces the possibility of electron-hole recombination, resulting in efficient separation and stronger photocatalytic activity of TiO_2.[17] [18] Doping TiO_2 also induces a red shift in the absorption spectrum, making it possible for visible light activation, enhancing the energy harvesting efficiency of this semiconductor.[19]
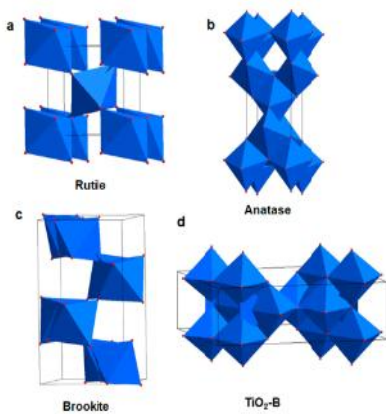
Figure 2-1: Cell structures of four TiO_2 polymorphs. (a) Rutile, (b) Anatase, (c) Brookite, and (d) TiO_2 (B). [20]

Synthesis of nanoparticles (NPs) has received great attention due to the advantage of higher surface area and consequently higher reaction sites for these materials. Many methods are used to prepare nanosize TiO_2 and doped TiO_2 including chemical, physical, solvo-thermal and hydro-thermal, and electrochemical processes, [21] which are reviewed in more detail below. Various morphologies have been prepared as shown in Figure 2-2, although nanoparticles are the most widely reported morphology. NPs provide high surface areas which give more reactive sites while reducing diffusion limitations. Recently one dimension (1D) forms such as nanowires are gaining special attention in many applications especially photovoltaic applications.[22-24]
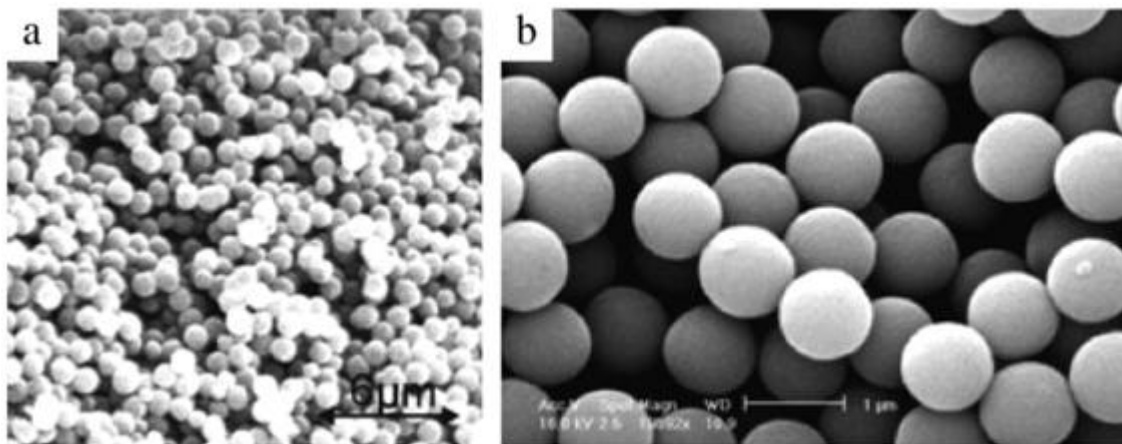
Figure 2-2: SEM images of spherical TiO_2 colloids synthesized by the sol –gel method with the addition of salts (a), and the addition of Lutensol ON 50 (b) (Eiden-Assmann et al., 2004).[25]
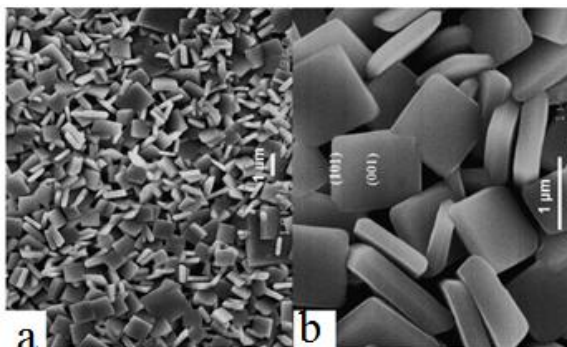
Figure 2-3: SEM images of the anatase TiO_2 nanosheets synthesized with a reaction time of 11 hr (Yang et al., 2009).[25]

2.2   Synthesis of Nanomaterials

This literature review will focus on a few selected methods based on their wide use and ease of application for the synthesis of doped titanium dioxide with a special focus on copper, bismuth and indium dopants, as examined in this thesis.

2.2.1   Direct oxidation method

This method is based on the combustion of titanium metal or nanoparticles. Kitamura et al. (2007) prepared titanium dioxide by flame treatment at temperatures exceeding the titanium boiling point in the presence of sodium perchlorate using a graphite crucible reactor under argon gas. They found that the size of nanomaterials depends on the starting materials' size as shown in Figure 2-4. Wu and Chen et al. (2014) used titanium plate to prepare fluorine doped titanium dioxide under oxidizing vapors of hydrogen peroxide and sodium fluoride and tested the synthesized materials for photodegradation of 4-nitrophenol under both UV and visible light (Figure 2-5). However, this method is not widely used due to the required high energy and low conversions. [26, 27]
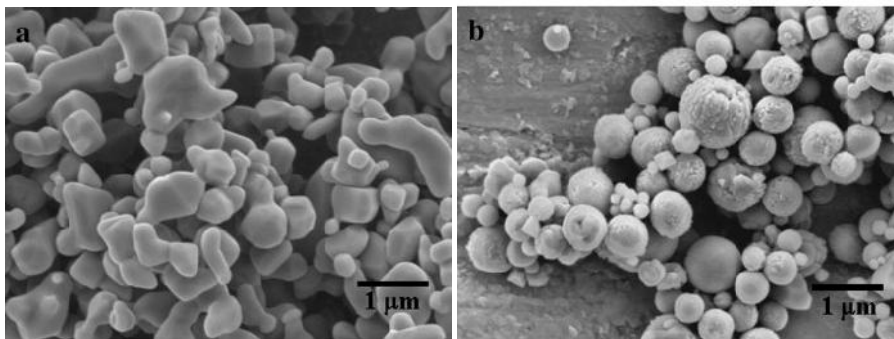
Figure 2-4: SEM images of two combustion-synthesized products from titanium for raw materials with different average particle sizes (a) 10 µm and (b) 25 µm. The products differed in shape. The former is irregular but the latter is spherical.[27]
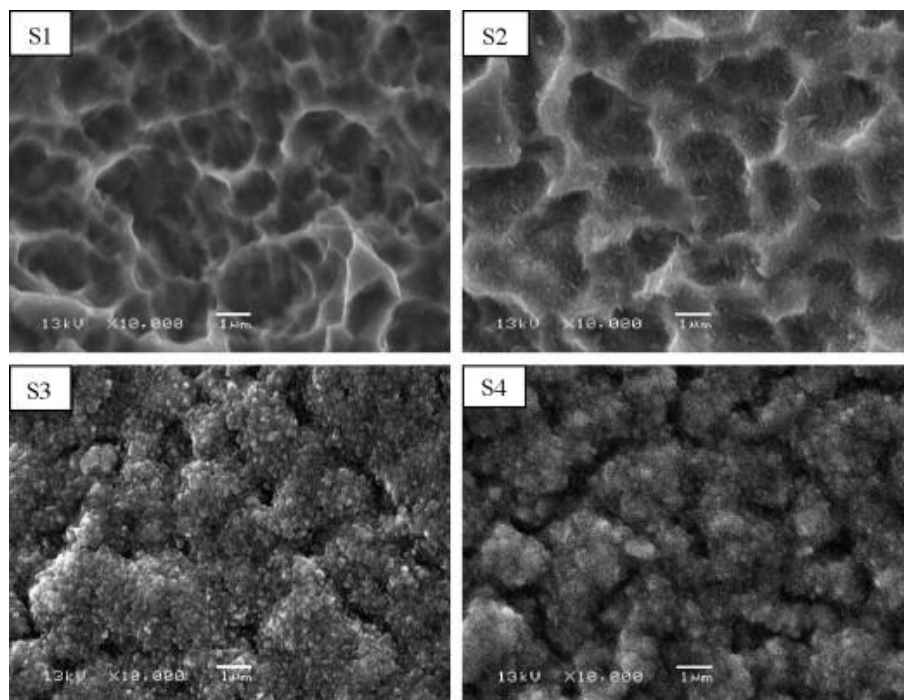
Figure 2-5: SEM images of the thin films grown on the titanium plates in the presence of water vapor assisted with NaF at different temperatures: (S1) 500 °C; (S2) 550 °C; (S3) 600 °C; and (S4) 650 °C.[26]

2.2.2   Chemical vapor deposition method

Chemical vapor deposition is generally used to prepare thin films of titanium dioxide on a substrate material by means of chemical reaction of gaseous species. This process uses thermally initiated reactions of a metal precursor on a heated surface. A volatile metal containing the precursor is thermally heated in a reactor with an inert gas flow where the metal vapor reaches the substrate, adsorbs to the substrate, then reacts creating seeds for more metal or metal oxide atoms to attach to the surface. Organometallic precursors such as tetraisopropoxide (TIP) are used in a cylindrical furnace to produce TiO_2 NPs with a size range from of 10-60 nm. Metal salts such as $TiCl_4$ were used to react with water vapors. Size control in CVD methods can be achieved by the control of the precursor's concentration, gas flow rate, temperature, and vacuum level. Figure 2-6 shows both a typical CVD reactor and SEM figures of titania samples prepared at various temperatures.[28] This method produces highly uniform films with reproducible morphologies, however, production is limited by the size of reactor while expensive volatile precursors are required.
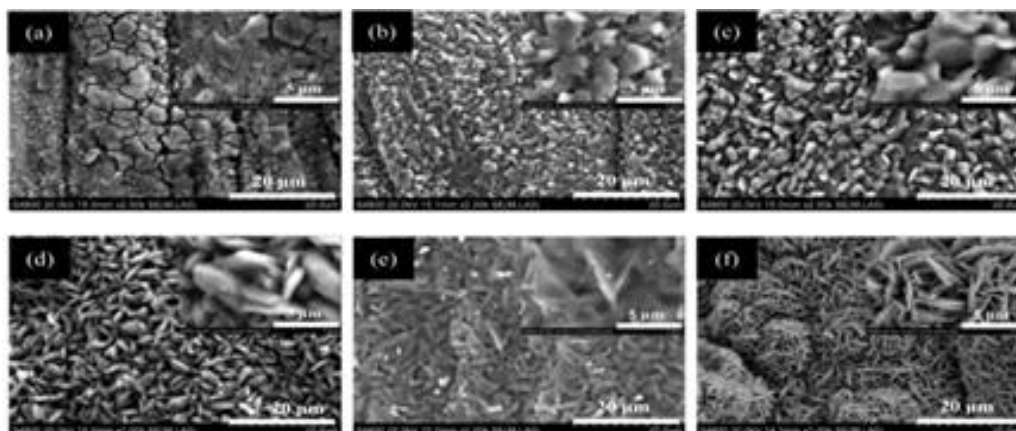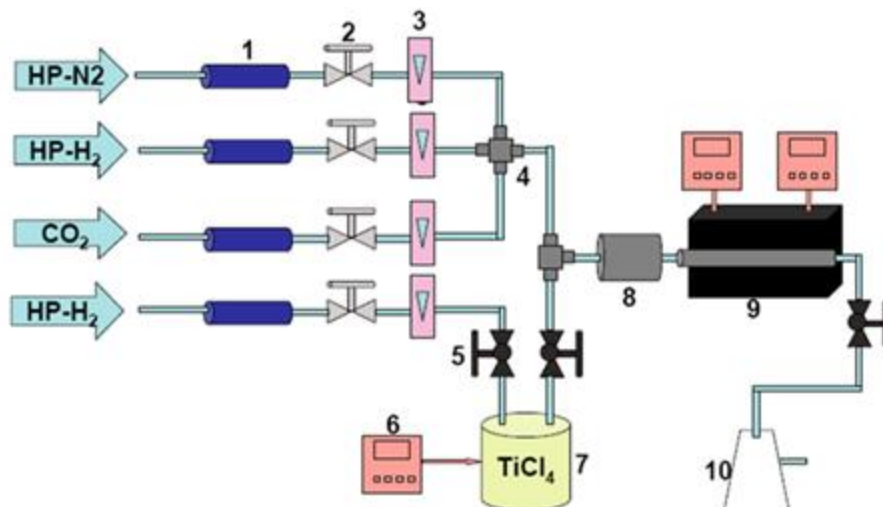
Figure 2-6: CVD reactor and SEM images of synthesized samples using this reactor at different temperatures (a) 650, (b) 700, (c)750, (d) 800, (e) 850, (f) 900 ℃ . [28]

2.2.3   Hydrothermal methods

The hydrothermal method is widely used to prepare nanostructured materials, specially 1D material such as nanotubes with wide pore and uniform tubular structures and single crystal titanium nanomaterials. For synthesis using this method, the metal precursor and alkali solution in water are heated in an autoclave reactor to initiate crystal growth. The resulting material is then calcined to transform the product from amorphous to crystalline phase. Temperature, pressure, and concentration are used as control parameters, affecting the final morphology of the material produced. [21] The growth mechanism is illustrated in Figure 2-7 below.
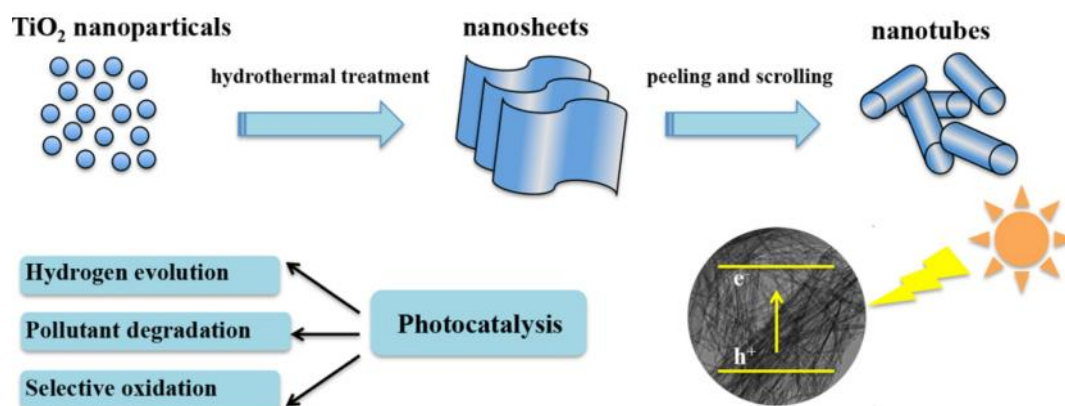
Figure 2-7: Schematic mechanisms for the hydrothermal formation of TNTs.[29]

Industrial production of NPs often uses the hydrothermal method due to its simplicity to obtain nanotubes, however, long reaction time to grow desired materials, use of harsh solvents and alkali such as NaOH, requirement for neutralization and waste treatment are some of the disadvantages of this method. Wang et al. (2014) published a review article covering most of the currently used methods to prepare nano sized titanium dioxide materials for environmental applications, expanding the understanding of hydrothermal and solvothermal synthesis. However, new approaches such as electrospinning, solution based routes and sol-gel chemistry seem to be gaining more interest due to their simplicity and less aggressive reaction conditions compared to hydrothermal or solvo-thermal methods.[30-34]

2.2.4   Sol-gel methods

Sol-gel chemistry is considered to be inexpensive, direct and relatively simple to prepare nanomaterials from precursors. This method is used to prepare a wide range of metal oxide nanomaterials. It involves the hydrolysis and condensation of metal precursors in a solvent (often alcohol) and the formation of a network of connected nanomaterials aged to form a gel. The solvent can be aqueous in which oxygen for the formation of oxide is provided by water molecules. The aqueous sol-gel method can be described by the following reaction:

$$M(OR)x + mH_2O \qquad M(OR)x\text{-}m(HO)m + mROH$$
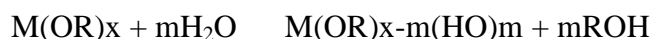
Total hydrolysis of the precursor can be achieved if x=m, and usually happens in two steps, either by water or alcohol condensation.[35-37]

$$2 \text{ M(OR)x-m(HO)m} \quad \text{(OH)m-1(OR)x-m-M-O-M(OR)x-m(OH)m-1} + H_2O$$

$$2 \text{ M(OR)x-m(HO)m} \quad \text{(OH)m-1(OR)x-m -M-O-M(OR)x-m-1} + ROH$$
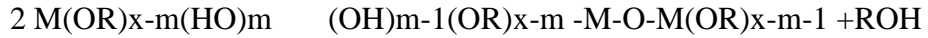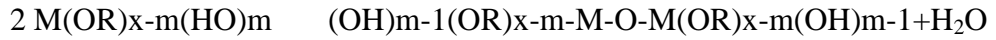
The overall reaction can be expressed as:

$$M \text{ (OR)x} + X/_2 \text{ } H_2O \quad MOx/2 + X \text{ R-OH}$$

In non-aqueous systems, oxygen is supplied by oxygenated solvents such as alcohol, ethers, ketones or by precursors such as alkoxide and acetylacetonate and will result in metal-oxygen-metal bonds by aldol-like condensation or by ether elimination.[38] Complete polymerization and solvent loss leads to the liquid "sol" transforming into a solid "gel" phase. This method involves hydrolysis of the metal alkoxide with water and a catalyst, i.e. an acid or a base, condensation into macromolecules, forming a colloidal sol and subsequently three-dimensional network, solvent exchange to remove water by alcohol, and then drying the wet gel using a supercritical fluid to produce the aerogel.

The properties of the sol-gel products depend on the precursors, processing temperature, catalyst, solvents, and solvent removal process [39]. This method also has several advantages over other methods, such as allowing impregnation or co-precipitation, which can be used to introduce dopants. The major advantages of the sol-gel technique include molecular scale mixing, high purity of the precursors, and homogeneity of the sol-gel products, with a high purity of physical, morphological, and chemical properties [40].

Sol-gel method is a promising solution based method to grow nanostructure materials in a reproducible way with relatively good control and a wide selection of precursors. Sol-gel can also be carried out in variety of solvents such as aqueous, organic or supercritical fluids. Supercritical carbon dioxide has been investigated in detail by the Charpentier group as a solvent for preparation of various nanostructures [25, 41, 42] which this thesis examines for the synthesis of nanowires.

2.3 Synthesis of Cu/TiO$_2$ Nanomaterials

Recently, copper doped titania has gained interest for sacrificial hydrogen production compared to rare and expensive noble metals due to its band gap edge position, cost effectiveness and abundance.[43] Research by Hara et al. (1998) highlighted the potential of Cu$_2$O under visible light to produce hydrogen. [44] Banadra et al. (2005) attributed the sacrificial hydrogen production to CuO, which effectively transferred photogenerated electrons to the copper (II) oxide surface, where water reduction took place.[45] Wu et al. prepared copper doped TiO$_2$ nanoparticles of mixed copper oxides by a wet impregnation method and tested for hydrogen production using a methanol-water mixture. Wang et al. prepared mixed copper oxides of CuO/TiO$_2$ and mentioned that CuO was not active to produce hydrogen. In their study a lag time of about 5 hours for hydrogen production (time to reduce CuO to Cu$_2$O) was clearly shown in Figure 2-9.[46]

The oxidation state of copper in Cu/TiO$_2$ is a critical factor in the hydrogen evolution reaction as it relates to both the chemical potential and electron-hole separation process. It was found that Cu$_2$O doped titania is the most active oxide for photocatalytic hydrogen production and Cu (II) is photocatalytically inactive. [47] Copper doped titanium dioxide catalyst was used in CO$_2$ conversion to produce fuels such as methanol as a green method to reduce the amount of global warming gas while producing energy at the same time.[48-54]

Several methods were explored to prepare copper doped titanium oxide resulting in mixed oxides or metallic copper with its oxides on the surface of titanium dioxide, as described below. In addition, these methods also produced different morphologies of copper doped titanium dioxide with varying photocatalytic activities.

Teseng et al (2004) used a sol-gel process to prepare mixed oxides of Cu/TiO$_2$ using copper chloride and copper acetate as the source of copper. Copper chloride precursor showed higher activities compared to copper acetate samples and Cu (I) is the primary active site for photoreduction of CO$_2$ to methanol. However, this study did not provide any details on catalyst morphology.[55] Parket al. (2015) investigated copper- titanium dioxide double layer film and copper loading for the reduction of CO$_2$, with Cu-TiO$_2$

being prepared by a solvothermal process. They observed that a double layer configuration was formed (TiO_2 at the bottom and Cu-TiO_2 as the top layer) at TiO_2/5.0 mol% Cu–TiO_2. This double layer effectively reduced charge recombination by enhancing surface charge transfer at TiO_2 and Cu–TiO_2 interface.[56]

Wu et al. (2004) prepared copper doped titania by an impregnation method where a titanium sulfate and copper nitrate mixture were reacted followed by calcination at 400 ℃. Highest amount of photocatalytic hydrogen was produced using 1.2 % wt Cu on titanium nanoparticles. [57] Yu et al. (2010) prepared nanorods of Cu-doped TiO_2 by injecting TTIP solution into heated copper (II) acetate in oleic acid. Temperature and reaction time were used to tune the synthesis process for the desired nanorods morphology. This approach produced copper (II) oxide nanorods of 2-5 nm diameter and 2-30 nm length.[58]

Foo et al. (2013) used a wet impregnation method to prepare CuO on the surface of TiO_2 which was then reduced under hydrogen stream to form a thin layer of Cu_2O on the surface of CuO that was transformed to metallic Cu. In the second step, the thick Cu_2O layer was produced by a short oxidation process, and in the final step, prolonged oxidation was used to produce Cu_2O on the surface of TiO_2 particles (Figure 2-8). Hydrogen production by the photocatalyst at different stages was tested using 40 ml of 10 vol % methanol and 0.04 g catalyst using a 300 watt Xe lamp. It was concluded that Cu-Cu_2O thin film was the most active photocatalyst, suggesting that was easy to be reduced to metallic Cu.[59]

 In addition to the oxidation state, the shape of nanomaterial, dispersion of dopant also has a strong effect on Cu/TiO_2 for hydrogen production. [60] Most currently prepared Cu doped TiO_2 morphologies are nanoparticles (NPs) [61], nanofilms [62], hollow spheres [63], nanosheets [64], and nanorods [65]. NPs are primarily used due to their relatively high surface areas to facilitate the required reactions. Nanowires provide a direct path for electron transport compared to the random tortuous path in NPs,[66] and are of great interest for photocatalytic applications. [67] However, to the best of our knowledge, the ability to produce pure Cu (I) doped titania is not reported in the literature.
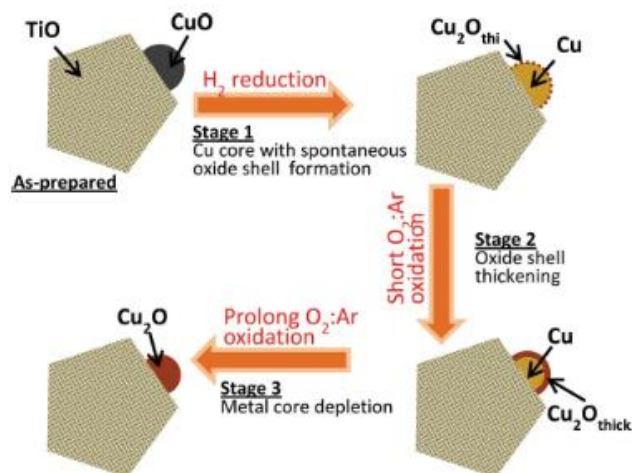
Figure 2-8: Schematic of structural-phase evolution of Cu loaded on TiO_2 photocatalyst at different stages.[59]
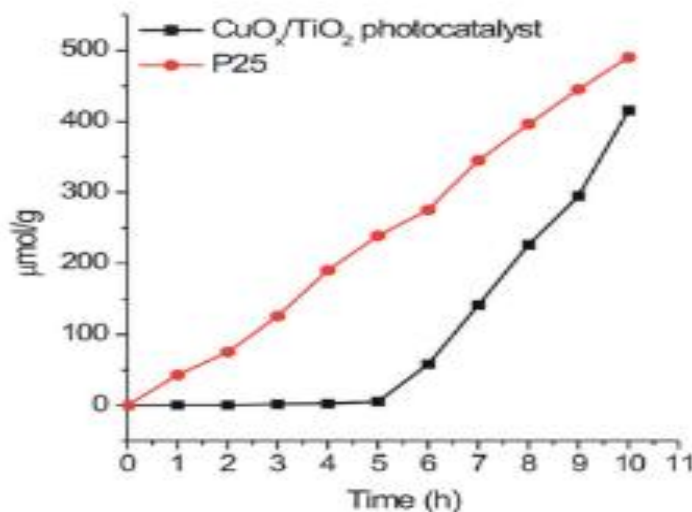
Figure 2-9: Photocatalytic activity of the as-synthesized CuOx-TiO_2 Photocatalyst and P25 in photocatalytic water reduction to H_2 under solar light irradiation. [46]

2.4 Synthesis of Bi/TiO_2

Bismuth is one of the most widely examined metals to dope titanium dioxide as it promotes visible light absorption and enhances photocatalytic activities. Enhanced visible light absorption is a result of hybridization of Bi (6p), Bi (6s) with Ti (3d), O (2p)

orbitals, respectively to provide the visible shift. It was found that bismuth titanate exhibits excellent photocatalytic performance for the degradation of methyl orange, Rhodamine B, and self cleaning under visible light conditions compared to undoped TiO_2.[68-70] In addition, bismuth titanate showed improved electrical conductivity and is used in piezoelectric devices and memory materials. [71, 72] Hydrothermal methods are commonly used to prepare different morphologies of bismuth titanate such as NPs, microspheres, nanowires, microflowers, nanosheets, nanofibers, nanocubes, nanobelts and nanorods. [73-75] The resulting morphology is governed by operating parameters such as the reaction temperature, pressure, time and the type of starting materials, concentration of reactants, pH, use of surfactant or additives. Hou et al. (2013) prepared different morphologies of $Bi_{12}TiO_{20}$ using bismuth nitrate and titanium tetra-isopropoxide as starting materials in a hydrothermal reactor.[75-84]

Bismuth titanate nanocubes were synthesized by a sol-gel hydrothermal method by An'amt et al (2010) where titanium tetra-isopropoxide and bismuth nitrate were used as precursors for titanium and bismuth, respectively.[85] In a typical experiment, the precursors were dissolved in tri-ethanolamine/water mixture then added into an autoclave and baked at 100 ℃ to produce nanocubes about 100 nm in size as shown in Figure 2-10.[81] Microspheres of $Bi_4Ti_3O_{12}$ were prepared using the hydrothermal method by Lin et al. (2012) which showed excellent photocatalytic activities under visible light.[86]
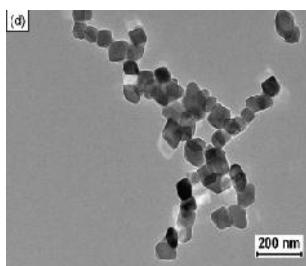
Figure 2-10: TEM image of Bi–TiO_2 synthesized by the sol–gel hydrothermal method. [81]

Nanosize bismuth titanate was prepared with varying shapes and sizes by Pei et al. (2014). They also synthesized bismuth titanate nanorods of 50-200 nm and a band gap of 2.58 eV using the hydrothermal method without any additives. They investigated the

growth mechanism by sampling the reactor at different time intervals during the synthesis process and analyzing them thoroughly. At low temperatures of 80 ℃ and even at long reaction times of 24 hours, only nanoparticles were observed. However, at increased temperatures of about 180 ℃, the results differed with time. At short reaction times, NPs were abundant with only a few short and thin nanorods (50 nm). However, as the reaction progressed with time, the diameter and length of these bismuth titanate nanorods increased significantly to reach 50-100 nm and 1 µm, respectively. It was concluded that NPs formed at the beginning of the hydrothermal process to create nucleation seeds, which then grew to nanorods with increased time, emphasizing the critical role of optimum temperature and reaction time as control parameters. These nanorods were tested for degradation of methylene blue dye and Rhodamine B with good photocatalytic performance.[70]

Electrospinning methods also have been used to prepare bismuth titanate nanorods, for example, Chen et al (2014) prepared titanium nanorods using electrospinning methods and combined it with the hydrothermal method to introduce bismuth into TiO_2 nanorods. These nanorods gave a higher photocatalytic activity to degrade methyl orange under visible light compared to electrospinned nanorods. The resulting assembly was found to be $Bi_4Ti_3O_{12}$ decorating the nanorods of TiO_2.[87] Wet chemical methods were also explored to prepare bismuth titanate pyrochlore nanorods. Oil-in water micro-emulsions were used by Murugesan et al. (2009) to prepare nanorods of 40-50 nm in diameter and about 500 nm in length. The reverse micelle approach was adopted to prepare 20 nm nanoparticles in oil bath at 350 ℃, which was rearranged to form nanorods during calcination at 500 ℃. [88]

The sol-gel method was utilized to prepare bismuth doped TiO_2 nanoparticles using titanium tetra-isopropoxide and bismuth nitrate as precursors in two steps by Sood et al.[89] First, titanium nanoparticles were prepared by mixing dissolved TTIP in ethanol and hydrolyzed in ethanol solution to form a gel. TiO_2 nanoparticles were then collected after the gel was aged for a day, and then were calcined at 450 ℃. Different amounts of bismuth nitrates were dissolved in ethanol-water mixtures, then catalyzed by nitric acid, and added to the prepared titanium sol and homogenized by ultrasonic probe and aged for

10 hours before drying and calcination. The resulting bismuth titanate nanoparticles were evaluated for Alizarin red S degradation with 1% Bi having the highest photocatalytic activity.

2.5 One-Dimensional Nanostructures

One-dimensional (1D) nanostructures (nanowires, nanotubes, nanobelts and nanoribbons) are of interest due to their fascinating physical properties and potential technological applications. [90-92] Recently elongated nanomaterials such as nanorods and nanowires have gained significant attention compared to nanoparticles and nanosheets, which are classified as zero and two dimensions, respectively. One dimension (1D) nanostructured materials are researched in many fields of application such as the photocatalytic degradation of organic pollutants, hydrogen generation, battery applications, chemical sensors, and photovoltaic applications. Their chemical and physical structures provide advantages over other structures such as a greater light to energy conversion, a reduction of electron and hole recombination, providing direct percolation pathways for electron transport (Figure 2-11), and light scattering to enhance photocatalytic performance, while improving the structure of the nanocomposite.[93-107] These materials come with special challenges of controlling growth in a specific direction for preparing desired structure. Although many synthesis methods have been reported in the literature, hydrothermal and solvo-thermal processes are mostly used for the preparation of 1D structure.
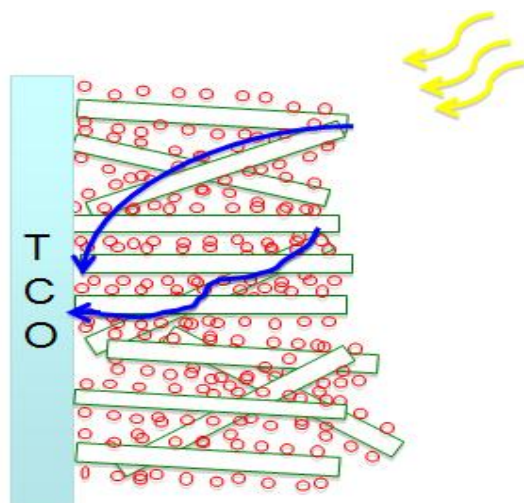
Figure 2-11: Schematic showing photoanode made of nanowires and direct percolation path represented by blue arrows.

Supercritical fluids to prepare nanomaterials are attracting the attention of many research groups as a non-toxic, green, and inexpensive solvent. They work in a less aggressive environment compared to hydrothermal and solvothermal methods that use base/acid or flammable organic solvents. Supercritical solvents such as CO_2 can produce highly uniform and complex morphology nanomaterials, especially those with pores. This is due to the excellent diffusion properties, zero surface tension and low viscosity of the supercritical fluids. CO_2 at a temperature and pressure about its critical point (31 ℃ and 7.4 MPa), is transformed to its supercritical state providing liquid-like solvent properties and gas like transport properties helping to maintain the structure and pores of synthesized nanomaterial from collapse. Wakayama et al. (2006) developed a novel template termed nanoscale casting with the help of supercritical CO_2 followed by burning the template at 600 ℃. Using CO_2 as the reaction solvent, they prepared alumina, platinum, platinum-ruthenium in acetone and titanium and calcium carbonate in 2-propanol and methanol, respectively.[108] A similar approach was recently used to deposit Pd on high surface area carbon for hydrogen storage applications using supercritical CO_2, which provided better dispersion of 2-5 nm Pd particles and increased hydrogen uptake [109] Also, supercritical CO_2 was used as an antisolvent to prepare different nanomaterials. [110, 111] For example, $AuPd/TiO_2$ was also prepared by using supercritical CO_2 as an antisolvent during precipitation of mixed precursors of gold,

palladium and titanium for hydrogen generation application. The resulting catalyst consisted of nanoparticles with bimodal distribution of 1-8 nm and 40-70 nm with the dopant forming sites mostly in the size of 0.5-1 nm.[112] In general, supercritical fluids are gaining more attention for preparation of nanomaterials with controlled morphologies as summarized in a recent review article by our research group.[113]

However, to the best of our knowledge, the synthesis of copper doped TiO_2 nanowires, bismuth titanate nanowires, and indium doped titanium nanowires prepared by sol-gel methods in supercritical CO_2 have not been reported in the literature. Of additional interest, it has been reported that indium doping has enhanced the performance of titania in UV and water splitting[114] [115] although In-TiO_2 nanowires have not been reported.

2.6 Polymeric Materials for Metal Oxide Nanowires

Organic polymers are of interest due their advantages of good flexibility, toughness, and separation properties. However, their poor resistance to fouling and high temperatures restricts their application in industrial processes such as membranes used for water purification. On the other hand, inorganic membranes such as ceramic membranes have higher thermal and chemical resistance and subsequently longer lifetimes, although they suffer from poor flexibility, low separation performance, and higher cost. [116-118]

There are many types of polymers to synthesize membranes with variable chemical and physical properties driven by the target application. Particularly, polymers for membranes have been examined which are non-fouling[119-125] Fouling causes deterioration of the membrane performance characterized by declining flux and water permeability by reversible or irreversible blockage of membrane pores from the fouling materials such as natural organic matter, extra cellular polymeric substances and microbial cells. In order to overcome membrane fouling, various approaches have been taken including developing new membrane materials or membrane cleaning processes using mechanical means such as the application of shear.

Polyethersulfone (PES) is widely used as an organic membrane due to its advantages such as high thermal stability and mechanical strength over other types of polymers. However, it suffers high fouling rates and low permeability due to its low hydrophilicity. Lee et al. (2007) conducted a series of experiments to study the relationship between hydrophobicity and fouling by natural organic matter. [117] Fouling by organic matter is strongly observed with hydrophobic membranes compared to hydrophilic ones. It is widely accepted that improving hydrophilicity will reflect positively on membrane flux and reduce adsorption of fouling materials to the membrane surface.[126] By copolymerization with hydrophilic compounds, improvements were made to enhance membrane resistance to fouling through improving hydrophilicity. [118, 127, 128]

Membrane modification is also used to enhance selectivity, reduce fouling, and improve flux by having a more hydrophilic membrane. Membranes can be modified by bulk modifications such as sulfonation, phosphonation, and carboxylation where corresponding functional groups are added to the polymer. [129-132] However, surface modifications are widely used for advantages by maintaining the original characteristics of bulk membrane and flexibility of modified surface of commercially available membranes.[133]

Introduction of carboxylic groups to the polymer backbone is an added advantage in terms of enhancing hydrophilicity; which can also be utilized for coordination of metal oxides and enhancing the thermal stability of the polysulfone polymer. [121] Typical reaction involves two steps to add a - COOH group to main polysulfone chain where polymer solution of polysulfone was activated with n-butyllithium and carboxylic group was introduced by the addition of carbon dioxide (CO_2). [134] Figure 2-12 shows a typical reaction of carboxylation of PES polymer. In this thesis, polysulfone polymers were prepared to be modified into nanotubes, functionalize with photocatalyst using available carboxylic and hydroxlyic groups on the polymer backbone. These polymers were selected based on available functional groups and with rigid backbone provided by aromatic rings compared to traditional membrane such as polyether sulfone.
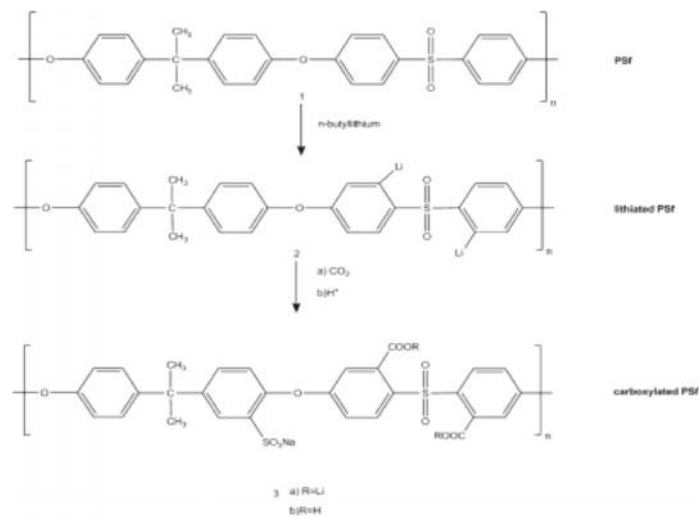
Figure 2-12: Mechanism of carboxylation of PES Membrane. [135]

2.7 Synthesis of Nanowires using Supercritical Carbon Dioxide

Supercritical fluids to prepare nanomaterials are attracting the attention of many research groups as a non-toxic, green, and inexpensive solvent. They work in a less aggressive environment compared to hydrothermal and solvothermal methods that use base/acid or flammable organic solvents. Supercritical solvents such as CO_2 can produce highly uniform and complex morphology nanomaterials, especially those with pores. This is due to the excellent diffusion properties, zero surface tension and low viscosity of the supercritical fluids. CO_2 at a temperature and pressure about its critical point (31 ºC and 7.4 MPa), is transformed to its supercritical state providing liquid-like solvent properties and gas like transport properties helping to maintain the structure and pores of synthesized nanomaterial from collapse. Wakayama et al. (2006) developed a novel nanoscale casting template with the help of supercritical CO_2 followed by burning the template at 600 ºC. Using CO_2 as the reaction solvent, they prepared alumina, platinum, platinum-ruthenium in acetone and titanium and calcium carbonate in 2-propanol and methanol, respectively.[108] A similar approach was recently used to deposit Pd on high surface area carbon for hydrogen storage applications using supercritical CO_2, which

provided better dispersion of 2-5 nm Pd particles. These increased hydrogen uptake from 12 to a maximum of 18.3 μmol/m^2 at an optimum loading of 0.4 wt % Pd. [109] Also, supercritical CO_2 was used as an antisolvent to prepare different nanomaterials. [110, 111] For example, AuPd/TiO_2 was also prepared by using supercritical CO_2 as an antisolvent during precipitation of mixed precursors of gold, palladium and titanium for hydrogen generation application. The resulting catalyst consisted of nanoparticles with bimodal distribution of 1-8 nm and 40-70 nm with the dopant forming sites mostly in the size of 0.5-1 nm.[112] In general, supercritical fluids are gaining more attention for preparation of nanomaterials with controlled morphologies as summarized in a recent review article by our research group.[113]

However, to the best of our knowledge, the synthesis of copper doped TiO_2 nanowires, bismuth titanate nanowires, and indium doped titanium nanowires prepared by sol-gel methods in supercritical CO_2 have not been reported in the literature. Of additional interest, it has been reported that indium doping has enhanced the performance of titania in UV and water splitting[114] [115] although In-TiO_2 nanowires have not been reported.

2.8   Objectives of the Research

The overall objective of this research is to investigate supercritical carbon dioxide (scCO$_2$) as a green solvent for the sol-gel synthesis of doped titanium nanowires using copper, bismuth and indium; while characterizing their photocatalytic and solar cell performance.

The following are the specific objectives of this research which are described in the following Chapters:

- Synthesis and application of bismuth titanate nanowires as photoanodes for dye sensitized solar cells (Chapter 6)

- Photocatalytic hydrogen production using bismuth titanate (Chapter 5Chapter 5)

- Synthesis of copper (I) doped TiO$_2$ nanowires using a sol-gel method in scCO$_2$ and its performance for sacrificial hydrogen production (Chapter 3)

- Synthesis of indium doped nanowires and their characterization for sacrificial hydrogen production and activity as photoanode in dye sensitized solar cells (Chapter 4)

- Synthesis of polysulfone membrane material for photocatalytic membrane applications (Chapter 7)

2.9 References

1. Zhang, X.Y. and Z.Y. Chen, *Enhanced photoelectrochemical performance of the hierarchical micro/nano-structured TiO$_2$ mesoporous spheres with oxygen vacancies via hydrogenation.* RSC Advances, 2015. **5**(13): p. 9482-9488.

2. Ansari, S.A., M.M. Khan, M.O. Ansari, and M.H. Cho, *Gold nanoparticles-sensitized wide and narrow band gap TiO$_2$ for visible light applications: a comparative study.* New Journal of Chemistry, 2015. **39**(6): p. 4708-4715.

3. Fujishima, A. and K. Honda, *Electrochemical Photolysis of Water at a Semiconductor Electrode.* Nature, 1972. **238**(5358): p. 37-+.

4. Carp, O., C.L. Huisman, and A. Reller, *Photoinduced reactivity of titanium dioxide.* Progress in Solid State Chemistry, 2004. **32**(1-2): p. 33-177.

5. Diebold, U., *The surface science of titanium dioxide.* Surface Science Reports, 2003. **48**(5-8): p. 53-229.

6. Henderson, M.A., *A surface science perspective on TiO$_2$ photocatalysis.* Surface Science Reports, 2011. **66**(6-7): p. 185-297.

7. Ajmal, A., I. Majeed, R.N. Malik, H. Idriss, and M.A. Nadeem, *Principles and mechanisms of photocatalytic dye degradation on TiO$_2$ based photocatalysts: a comparative overview.* RSC Advances, 2014. **4**(70): p. 37003-37026.

8. Saien, J. and A.R. Soleymani, *Feasibility of using a slurry falling film photo-reactor for individual and hybridized AOPs.* Journal of Industrial and Engineering Chemistry, 2012. **18**(5): p. 1683-1688.

9. Ai, G.J., R. Mo, Q. Chen, H. Xu, S. Yang, H.X. Li, and J.X. Zhong, *TiO2/Bi2S3 core-shell nanowire arrays for photoelectrochemical hydrogen generation.* RSC Advances, 2015. **5**(18): p. 13544-13549.

10. Saien, J., Z. Ojaghloo, A.R. Soleymani, and M.H. Rasoulifard, *Homogeneous and heterogeneous AOPs for rapid degradation of Triton X-100 in aqueous media via UV light, nano titania hydrogen peroxide and potassium persulfate.* Chemical Engineering Journal, 2011. **167**(1): p. 172-182.

11. Guo, W., Q.Q. Feng, Y.F. Tao, L.J. Zheng, Z.Y. Han, and J.M. Ma, *Systematic investigation on the gas-sensing performance of TiO$_2$ nanoplate sensors for enhanced detection on toxic gases.* Materials Research Bulletin, 2016. **73**: p. 302-307.

12. Al-Ahmed, A., B. Mukhtar, S. Hossain, S.M.J. Zaidi, and S.U. Rahman, *Application of titanium dioxide (TiO $_2$) based photocatalytic nanomaterials in solar and hydrogen energy: A short review*, in *Materials Science Forum*. 2012. p. 25-47.

13.   Sharifi, N., F. Tajabadi, and N. Taghavinia, *Recent developments in dye-sensitized solar cells.* ChemPhysChem, 2014. **15**(18): p. 3902-3927.

14.   Linsebigler, A.L., G.Q. Lu, and J.T. Yates, *Photocatalysis on Tio2 Surfaces - Principles, Mechanisms, and Selected Results.* Chemical Reviews, 1995. **95**(3): p. 735-758.

15.   Roose, B., S. Pathak, and U. Steiner, *Doping of TiO₂ for sensitized solar cells.* Chem Soc Rev, 2015. **44**(22): p. 8326-8349.

16.   Anpo, M. and M. Takeuchi, *The design and development of highly reactive titanium oxide photocatalysts operating under visible light irradiation.* Journal of Catalysis, 2003. **216**(1-2): p. 505-516.

17.   Mahlambi, M.M., A.K. Mishra, S.B. Mishra, R.W. Krause, B.B. Mamba, and A.M. Raichur, *Metal doped nanosized titania used for the photocatalytic degradation of rhodamine B dye under visible-light.* J Nanosci Nanotechnol, 2013. **13**(7): p. 4934-4942.

18.   Kim, S., S.J. Hwang, and W. Choi, *Visible light active platinum-ion-doped TiO2 photocatalyst.* J Phys Chem B, 2005. **109**(51): p. 24260-24267.

19.   Jia, Y.S., S. Shen, D.G. Wang, X. Wang, J.Y. Shi, F.X. Zhang, H.X. Han, and C. Li, *Composite Sr₂TiO₄/SrTiO₃(La,Cr) heterojunction based photocatalyst for hydrogen production under visible light irradiation.* Journal of Materials Chemistry A, 2013. **1**(27): p. 7905-7912.

20.   Wang, X., Z. Li, J. Shi, and Y. Yu, *One-dimensional titanium dioxide nanomaterials: nanowires, nanorods, and nanobelts.* Chem Rev, 2014. **114**(19): p. 9346-9384.

21.   Liu, N., X.Y. Chen, J.L. Zhang, and J.W. Schwank, *A review on TiO2-based nanotubes synthesized via hydrothermal method: Formation mechanism, structure modification, and photocatalytic applications.* Catalysis Today, 2014. **225**: p. 34-51.

22.   Wu, H.B., H.H. Hng, and X.W. Lou, *Direct Synthesis of Anatase TiO2 Nanowires with Enhanced Photocatalytic Activity.* Advanced Materials, 2012. **24**(19): p. 2567-2571.

23.   Tacchini, I., A. Ansón-Casaos, Y. Yu, M.T. Martinez, and M. Lira-Cantú, *Hydrothermal synthesis of 1D TiO ₂ nanostructures for dye sensitized solar cells.* Materials Science and Engineering: B, 2012. **177**(1): p. 19-26.

24.   Wen, L., Z. Wang, Y. Mi, R. Xu, S.H. Yu, and Y. Lei, *Designing Heterogeneous 1D Nanostructure Arrays Based on AAO Templates for Energy Applications.* Small, 2015. **11**(28): p. 3408-3428.

25.   Wang, Y., Y. He, Q. Lai, and M. Fan, *Review of the progress in preparing nano TiO$_2$: an important environmental engineering material.* J Environ Sci (China), 2014. **26**(11): p. 2139-2177.

26.   Wu, G.S. and A. Chen, *Direct growth of F-doped TiO$_2$ particulate thin films with high photocatalytic activity for environmental applications.* Journal of Photochemistry and Photobiology a-Chemistry, 2008. **195**(1): p. 47-53.

27.   Kitamura, Y., N. Okinaka, T. Shibayama, O.O.P. Mahaney, D. Kusano, B. Ohtani, and T. Akiyama, *Combustion synthesis of TiO2 nanoparticles as photocatalyst.* Powder Technology, 2007. **176**(2-3): p. 93-98.

28.   Tang, S., J. Wang, Q. Zhu, Y. Chen, and X. Li, *Preparation of rutile TiO($_2$) coating by thermal chemical vapor deposition for anticoking applications.* ACS Appl Mater Interfaces, 2014. **6**(19): p. 17157-17165.

29.   Liu, N., X. Chen, J. Zhang, and J.W. Schwank, *A review on TiO$_2$-based nanotubes synthesized via hydrothermal method: Formation mechanism, structure modification, and photocatalytic applications.* Catalysis Today, 2014. **225**: p. 34-51.

30.   Liu, S., Z.R. Tang, Y. Sun, J.C. Colmenares, and Y.J. Xu, *One-dimension-based spatially ordered architectures for solar energy conversion.* Chem Soc Rev, 2015. **44**(15): p. 5053-5075.

31.   Nalbandian, M.J., M. Zhang, J. Sanchez, S. Kim, Y.H. Choa, D.M. Cwiertny, and N.V. Myung, *Synthesis and optimization of Ag-TiO$_2$ composite nanofibers for photocatalytic treatment of impaired water sources.* J Hazard Mater, 2015. **299**: p. 141-148.

32.   Bao, C., J. Yang, H. Gao, F. Li, Y. Yao, B. Yang, G. Fu, X. Zhou, T. Yu, Y. Qin, J. Liu, and Z. Zou, *In situ fabrication of highly conductive metal nanowire networks with high transmittance from deep-ultraviolet to near-infrared.* ACS Nano, 2015. **9**(3): p. 2502-2509.

33.   Yu, M., Y.Z. Long, B. Sun, and Z. Fan, *Recent advances in solar cells based on one-dimensional nanostructure arrays.* Nanoscale, 2012. **4**(9): p. 2783-2796.

34.   Amna, T., M.S. Hassan, W.S. Shin, H. Van Ba, H.K. Lee, M.S. Khil, and I.H. Hwang, *TiO2 nanorods via one-step electrospinning technique: a novel nanomatrix for mouse myoblasts adhesion and propagation.* Colloids Surf B Biointerfaces, 2013. **101**: p. 424-429.

35.   Venkatachalam, N., M. Palanichamy, and V. Murugesan, *Sol-gel preparation and characterization of nanosize TiO$_2$: Its photocatalytic performance.* Materials Chemistry and Physics, 2007. **104**(2-3): p. 454-459.

36. Valencia, S., X. Vargas, L. Rios, G. Restrepo, and J.M. Marin, *Sol-gel and low-temperature solvothermal synthesis of photoactive nano-titanium dioxide.* Journal of Photochemistry and Photobiology a-Chemistry, 2013. **251**: p. 175-181.

37. Behnajady, M.A., H. Eskandarloo, N. Modirshahla, and M. Shokri, *Investigation of the effect of sol-gel synthesis variables on structural and photocatalytic properties of TiO2 nanoparticles.* Desalination, 2011. **278**(1-3): p. 10-17.

38. Sygkridou, D., A. Rapsomanikis, and E. Stathatos, *Quasi-Solid State Dye-Sensitized Solar Cells with Photoanodes Prepared by Different TiO₂ Precursors Using Sol–Gel Method.* Journal of Surfaces and Interfaces of Materials, 2014. **2**(4): p. 252-260.

39. Brinker, C.J.S., G. W., , *Sol-Gel Science.* The physics and Chemistry of Sol-Gel Processing Academic press, New York,1990

40. Kolen'ko, Y.V., K.A. Kovnir, A.I. Gavrilov, A.V. Garshev, P.E. Meskin, B.R. Churagulov, M. Bouchard, C. Colbeau-Justin, O.I. Lebedev, G. Van Tendeloo, and M. Yoshimura, *Structural, textural, and electronic properties of a nanosized mesoporous ZnxTi1-xO$_2$-x solid solution prepared by a supercritical drying route.* Journal of Physical Chemistry B, 2005. **109**(43): p. 20303-20309.

41. Foo, K.L., U. Hashim, K. Muhammad, and C.H. Voon, *Sol-gel synthesized zinc oxide nanorods and their structural and optical investigation for optoelectronic application.* Nanoscale Res Lett, 2014. **9**(1): p. 429.

42. Kim, D.H., W.M. Seong, I.J. Park, E.S. Yoo, S.S. Shin, J.S. Kim, H.S. Jung, S. Lee, and K.S. Hong, *Anatase TiO2 nanorod-decoration for highly efficient photoenergy conversion.* Nanoscale, 2013. **5**(23): p. 11725-11732.

43. Lalitha, K., G. Sadanandam, V.D. Kumari, M. Subrahmanyam, B. Sreedhar, and N.Y. Hebalkar, *Highly Stabilized and Finely Dispersed Cu$_2$O/TiO$_2$: A Promising Visible Sensitive Photocatalyst for Continuous Production of Hydrogen from Glycerol:Water Mixtures.* Journal of Physical Chemistry C, 2010. **114**(50): p. 22181-22189.

44. Hara, M., T. Kondo, M. Komoda, S. Ikeda, K. Shinohara, A. Tanaka, J.N. Kondo, and K. Domen, *Cu$_2$O as a photocatalyst for overall water splitting under visible light irradiation.* Chem Commun (Camb), 1998(3): p. 357-358.

45. Bandara, J., C.P. Udawatta, and C.S. Rajapakse, *Highly stable CuO incorporated TiO($_2$) catalyst for photo-catalytic hydrogen production from H($_2$)O.* Photochem Photobiol Sci, 2005. **4**(11): p. 857-861.

46.   Wang, Z., Y. Liu, D.J. Martin, W. Wang, J. Tang, and W. Huang, *CuOx-TiO$_2$ junction: what is the active component for photocatalytic H$_2$ production?* Phys Chem Chem Phys, 2013. **15**(36): p. 14956-14960.

47.   Wu, Y., G. Lu, and S. Li, *The Role of Cu(I) Species for Photocatalytic Hydrogen Generation Over CuO x /TiO$_2$.* Catalysis Letters, 2009. **133**(1-2): p. 97-105.

48.   Adachi, K., K. Ohta, and T. Mizuno, *Photocatalytic Reduction of Carbon-Dioxide to Hydrocarbon Using Copper-Loaded Titanium-Dioxide.* Solar Energy, 1994. **53**(2): p. 187-190.

49.   Hirano, K., K. Inoue, and T. Yatsu, *Photocatalysed reduction of CO$_2$ in aqueous TiO$_2$ suspension mixed with copper powder.* Journal of Photochemistry and Photobiology A: Chemistry, 1992. **64**(2): p. 255-258.

50.   Li, Y., W.N. Wang, Z.L. Zhan, M.H. Woo, C.Y. Wu, and P. Biswas, *Photocatalytic reduction of CO$_2$ with H2O on mesoporous silica supported Cu/TiO$_2$ catalysts.* Applied Catalysis B-Environmental, 2010. **100**(1-2): p. 386-392.

51.   Liu, L.J., F. Gao, H.L. Zhao, and Y. Li, *Tailoring Cu valence and oxygen vacancy in Cu/TiO$_2$ catalysts for enhanced CO$_2$ photoreduction efficiency.* Applied Catalysis B-Environmental, 2013. **134**: p. 349-358.

52.   Qin, S., F. Xin, Y. Liu, X. Yin, and W. Ma, *Photocatalytic reduction of CO$_2$ in methanol to methyl formate over CuO-TiO$_2$ composite catalysts.* J Colloid Interface Sci, 2011. **356**(1): p. 257-261.

53.   Slamet, H.W. Nasution, E. Purnama, S. Kosela, and J. Gunlazuardi, *Photocatalytic reduction of CO$_2$ on copper-doped Titania catalysts prepared by improved-impregnation method.* Catalysis Communications, 2005. **6**(5): p. 313-319.

54.   Park, M., B.S. Kwak, S.W. Jo, and M. Kang, *Effective CH4 production from CO2 photoreduction using TiO$_2$/x mol% Cu-TiO$_2$ double-layered films.* Energy Conversion and Management, 2015. **103**: p. 431-438.

55.   Tseng, I.H., J.C.S. Wu, and H.Y. Chou, *Effects of sol-gel procedures on the photocatalysis of Cu/TiO$_2$ in CO$_2$ photoreduction.* Journal of Catalysis, 2004. **221**(2): p. 432-440.

56.   Park, M., B.S. Kwak, S.W. Jo, and M. Kang, *Effective CH4 production from CO2 photoreduction using TiO$_2$/x mol% Cu–TiO$_2$ double-layered films.* Energy Conversion and Management, 2015. **103**: p. 431-438.

57.   Wu, N.-L. and M.-S. Lee, *Enhanced TiO$_2$ photocatalysis by Cu in hydrogen production from aqueous methanol solution.* International Journal of Hydrogen Energy, 2004. **29**(15): p. 1601-1605.

58.   You, M., T.G. Kim, and Y.M. Sung, *Synthesis of Cu-Doped TiO₂ Nanorods with Various Aspect Ratios and Dopant Concentrations.* Crystal Growth & Design, 2010. **10**(2): p. 983-987.

59.   Foo, W.J., C. Zhang, and G.W. Ho, *Non-noble metal Cu-loaded TiO₂ for enhanced photocatalytic H₂ production.* Nanoscale, 2013. **5**(2): p. 759-764.

60.   Obregón, S., M.J. Muñoz-Batista, M. Fernández-García, A. Kubacka, and G. Colón, *Cu–TiO₂ systems for the photocatalytic H₂ production: Influence of structural and surface support features.* Applied Catalysis B: Environmental, 2015. **179**: p. 468-478.

61.   Gombac, V., L. Sordelli, T. Montini, J.J. Delgado, A. Adamski, G. Adami, M. Cargnello, S. Bernal, and P. Fornasiero, *CuO(x)-TiO₂ photocatalysts for H2 production from ethanol and glycerol solutions.* J Phys Chem A, 2010. **114**(11): p. 3916-3925.

62.   Paracchino, A., V. Laporte, K. Sivula, M. Gratzel, and E. Thimsen, *Highly active oxide photocathode for photoelectrochemical water reduction.* Nat Mater, 2011. **10**(6): p. 456-461.

63.   Wu, D.X., Y.J. Wang, C.Y. Zhang, and H.T. Zhu, *3D Flowerlike Copper Sulfide Nanostructures Synthesized from Copper (I) Oxide Hollow Microspheres.* Iumrs International Conference in Asia 2011, 2012. **36**(0): p. 25-33.

64.   Zou, Y.L., S.Z. Kang, X.Q. Li, L.X. Qin, and J. Mu, *TiO₂ nanosheets loaded with Cu: A low-cost efficient photocatalytic system for hydrogen evolution from water.* International Journal of Hydrogen Energy, 2014. **39**(28): p. 15403-15410.

65.   You, M., T.G. Kim, and Y.-M. Sung, *Synthesis of Cu-Doped TiO₂Nanorods with Various Aspect Ratios and Dopant Concentrations.* Crystal Growth & Design, 2010. **10**(2): p. 983-987.

66.   Baxter, J.B. and E.S. Aydil, *Nanowire-based dye-sensitized solar cells.* Applied Physics Letters, 2005. **86**(5): p. 053114.

67.   Bashiri, R., N.M. Mohamed, C.F. Kait, and S. Sufian, *Hydrogen production from water photosplitting using Cu/TiO₂ nanoparticles: Effect of hydrolysis rate and reaction medium.* International Journal of Hydrogen Energy, 2015. **40**(18): p. 6021-6037.

68.   Wu, Y.Q., G.X. Lu, and S.B. Li, *The Doping Effect of Bi on TiO₂ for Photocatalytic Hydrogen Generation and Photodecolorization of Rhodamine B.* Journal of Physical Chemistry C, 2009. **113**(22): p. 9950-9955.

69.   Liu, H., Y. Chen, G. Tian, Z. Ren, C. Tian, and H. Fu, *Visible-Light-Induced Self-Cleaning Property of Bi₂Ti₂O₇-TiO₂ Composite Nanowire Arrays.* Langmuir, 2015. **31**(21): p. 5962-5969.

70. Pei, L.Z., H.D. Liu, N. Lin, and H.Y. Yu, *Bismuth titanate nanorods and their visible light photocatalytic properties.* Journal of Alloys and Compounds, 2015. **622**: p. 254-261.

71. Singla, G., P.K. Jha, J.K. Gill, and K. Singh, *Structural, thermal and electrical properties of Ti4+ substituted Bi2O3 solid systems.* Ceramics International, 2012. **38**(3): p. 2065-2070.

72. Cheng, R.F., L.N. Zhu, Y.L. Zhu, Z.J. Xu, R.Q. Chu, H.Y. Li, J.G. Hao, J. Du, and G.R. Li, *Giant piezoelectricity and ultrahigh strain response in bismuth sodium titanate lead-free ceramics.* Materials Letters, 2016. **165**: p. 143-146.

73. Cao, T.P., Y.J. Li, C.H. Wang, Z.Y. Zhang, M.Y. Zhang, C.L. Shao, and Y.C. Liu, *$Bi_4Ti_3O_{12}$ nanosheets/TiO_2 submicron fibers heterostructures: in situ fabrication and high visible light photocatalytic activity.* Journal of Materials Chemistry, 2011. **21**(19): p. 6922-6927.

74. Hou, D., X. Hu, P. Hu, W. Zhang, M. Zhang, and Y. Huang, *$Bi_4Ti_3O_{12}$ nanofibers-BiOI nanosheets p-n junction: facile synthesis and enhanced visible-light photocatalytic activity.* Nanoscale, 2013. **5**(20): p. 9764-9772.

75. Hao, P., Z.H. Zhao, J. Tian, Y.H. Sang, G.W. Yu, H. Liu, S.W. Chen, and W.J. Zhou, *Bismuth titanate nanobelts through a low-temperature nanoscale solid-state reaction.* Acta Materialia, 2014. **62**: p. 258-266.

76. Lin, X., Y.-n. Gong, Y.-d. Zhang, Y.-s. Yan, and Q.-f. Guan, *Influence of pH Value on Photocatalytic Activity of $Bi_4Ti_3O_{12}$ Crystals Obtained by Hydrothermal Method.* Chinese Journal of Chemical Physics, 2014. **27**(2): p. 209-213.

77. Lin, X., Q. Guan, Y. Zhang, T. Liu, C. Zou, C. Liu, and H. Zhai, *Visible light photocatalytic properties of $Bi_{3.25}Eu_{0.75}Ti_3O_{12}$ nanowires.* Journal of Physics and Chemistry of Solids, 2013. **74**(9): p. 1254-1262.

78. Lin, X., Q. Guan, C. Zou, T. Liu, Y. Zhang, C. Liu, and H. Zhai, *Photocatalytic degradation of an azo dye using $Bi_{3.25}M_{0.75}Ti_3O_{12}$ nanowires (M=La, Sm, Nd, and Eu).* Materials Science and Engineering: B, 2013. **178**(8): p. 520-526.

79. West, J.C., *Case law update. Medical Protective Company v. Duma, Nos. 10-3866, 10-3867 (6th Cir. May 1, 2012).* J Healthc Risk Manag, 2013. **32**(3): p. 47-52.

80. Shi, Q., J.K. Ren, Y.P. Wang, P.Y. Peng, and W.A. Wang, *Effect of N doping on morphology and property of bismuth titanate TiO_2 composite catalyst.* Zhongguo Youse Jinshu Xuebao/Chinese Journal of Nonferrous Metals, 2013. **23**(2): p. 487-494.

81. Yong, S.W., H.K. Osman, S.T. Ong, S.T. Ha, and S.L. Lee, *Synthesis, Characterization and Photocatalytic Behaviour of Cubic Structured*

Nanocrystalline Bismuth Titanate. Asian Journal of Chemistry, 2014. **26**(21): p. 7463-7466.

82.   Zhao, W., Z. Jia, E. Lei, L. Wang, Z. Li, and Y. Dai, *Photocatalytic degradation efficacy of $Bi_4Ti_3O_{12}$ micro-scale platelets over methylene blue under visible light.* Journal of Physics and Chemistry of Solids, 2013. **74**(11): p. 1604-1607.

83.   Hou, J., Z. Wang, C. Yang, W. Zhou, S. Jiao, and H. Zhu, *Hierarchically Plasmonic Z-Scheme Photocatalyst of Ag/AgCl Nanocrystals Decorated Mesoporous Single-Crystalline Metastable $Bi_{20}TiO_{32}$ Nanosheets.* The Journal of Physical Chemistry C, 2013. **117**(10): p. 5132-5141.

84.   Kargin, Y.F., S.N. Ivicheva, and V.V. Volkov, *Phase relations in the Bi_2O_3-TiO_2 system.* Russian Journal of Inorganic Chemistry, 2015. **60**(5): p. 619-625.

85.   An'amt, M.N., S. Radiman, N.M. Huang, M.A. Yarmo, N.P. Ariyanto, H.N. Lim, and M.R. Muhamad, *Sol-gel hydrothermal synthesis of bismuth-TiO_2 nanocubes for dye-sensitized solar cell.* Ceramics International, 2010. **36**(7): p. 2215-2220.

86.   Lin, X., P. Lv, Q.F. Guan, H.B. Li, H.J. Zhai, and C.B. Liu, *Bismuth titanate microspheres: Directed synthesis and their visible light photocatalytic activity.* Applied Surface Science, 2012. **258**(18): p. 7146-7153.

87.   Chen, K., Y. Li, H. Tian, and H. Gu, *Synthesis and photocatalytic performance of heterostructured nano-composite $Bi_4Ti_3O_{12}$/TiO_2.* Cailiao Yanjiu Xuebao/Chinese Journal of Materials Research, 2014. **28**(7): p. 503-508.

88.   Murugesan, S. and V.R. Subramanian, *Robust synthesis of bismuth titanate pyrochlore nanorods and their photocatalytic applications.* Chem Commun (Camb), 2009(34): p. 5109-5111.

89.   Sood, S., S.K. Mehta, A. Umar, and S.K. Kansal, *The visible light-driven photocatalytic degradation of Alizarin red S using Bi-doped TiO_2 nanoparticles.* New Journal of Chemistry, 2014. **38**(7): p. 3127-3136.

90.   Weng, B., S.Q. Liu, Z.R. Tang, and Y.J. Xu, *One-dimensional nanostructure based materials for versatile photocatalytic applications.* RSC Advances, 2014. **4**(25): p. 12685-12700.

91.   Gao, C.T., X.D. Li, X.P. Zhu, L.L. Chen, Z.M. Zhang, Y.Q. Wang, Z.X. Zhang, H.G. Duan, and E.Q. Xie, *Branched hierarchical photoanode of titanium dioxide nanoneedles on tin dioxide nanofiber network for high performance dye-sensitized solar cells.* Journal of Power Sources, 2014. **264**: p. 15-21.

92.   Chai, Z.S., J.W. Gu, P.F. Qiang, X. Yu, and W.J. Mai, *Facile conversion of rutile titanium dioxide nanowires to nanotubes for enhancing the performance of dye-sensitized solar cells.* CrystEngComm, 2015. **17**(5): p. 1115-1120.

93.   No, Y.J., S.I. Roohani-Esfahani, and H. Zreiqat, *Nanomaterials: the next step in injectable bone cements.* Nanomedicine (Lond), 2014. **9**(11): p. 1745-1764.

94.   Khaled, S.M., P.A. Charpentier, and A.S. Rizkalla, *Synthesis and characterization of poly(methyl methacrylate)-based experimental bone cements reinforced with TiO_2-SrO nanotubes.* Acta Biomater, 2010. **6**(8): p. 3178-3186.

95.   Elumalai, N.K., T.M. Jin, V. Chellappan, R. Jose, S.K. Palaniswamy, S. Jayaraman, H.K. Raut, and S. Ramakrishna, *Electrospun ZnO nanowire plantations in the electron transport layer for high-efficiency inverted organic solar cells.* ACS Appl Mater Interfaces, 2013. **5**(19): p. 9396-9404.

96.   Archana, P.S., E. Naveen Kumar, C. Vijila, S. Ramakrishna, M.M. Yusoff, and R. Jose, *Random nanowires of nickel doped TiO_2 with high surface area and electron mobility for high efficiency dye-sensitized solar cells.* Dalton Trans, 2013. **42**(4): p. 1024-1032.

97.   Mitschang, F., M. Langner, H. Vieker, A. Beyer, and A. Greiner, *Preparation of conductive gold nanowires in confined environment of gold-filled polymer nanotubes.* Macromol Rapid Commun, 2015. **36**(3): p. 304-310.

98.   Lee, H.G., G. Sai-Anand, S. Komathi, A.I. Gopalan, S.W. Kang, and K.P. Lee, *Efficient visible-light-driven photocatalytic degradation of nitrophenol by using graphene-encapsulated $TiO_{(2)}$ nanowires.* J Hazard Mater, 2015. **283**: p. 400-409.

99.   Xia, G., Y. Tan, D. Li, Z. Guo, H. Liu, Z. Liu, and X. Yu, *Hierarchical porous $Li_{(2)}Mg(NH)_{(2)}$@C nanowires with long cycle life towards stable hydrogen storage.* Sci Rep, 2014. **4**: p. 6599.

100.   Lee, W.S., Y.S. Park, and Y.K. Cho, *Hierarchically structured suspended TiO_2 nanofibers for use in UV and pH sensor devices.* ACS Appl Mater Interfaces, 2014. **6**(15): p. 12189-12195.

101.   Archana, P.S., A. Gupta, M.M. Yusoff, and R. Jose, *Tungsten doped titanium dioxide nanowires for high efficiency dye-sensitized solar cells.* Phys Chem Chem Phys, 2014. **16**(16): p. 7448-7454.

102.   Noh, S.I., D.W. Park, H.S. Shim, and H.J. Ahn, *Fabrication and photovoltaic properties of heterostructured TiO2 nanowires.* J Nanosci Nanotechnol, 2012. **12**(7): p. 6065-6068.

103.   Boyle, T.J., T.Q. Doan, L.A. Steele, C. Apblett, S.M. Hoppe, K. Hawthorne, R.M. Kalinich, and W.M. Sigmund, *Tin(II) amide/alkoxide coordination compounds for production of Sn-based nanowires for lithium ion battery anode materials.* Dalton Trans, 2012. **41**(31): p. 9349-9364.

104.   Mathews, N., B. Varghese, C. Sun, V. Thavasi, B.P. Andreasson, C.H. Sow, S. Ramakrishna, and S.G. Mhaisalkar, *Oxide nanowire networks and their electronic and optoelectronic characteristics.* Nanoscale, 2010. **2**(10): p. 1984-1998.

105.   Mai, L., L. Xu, C. Han, X. Xu, Y. Luo, S. Zhao, and Y. Zhao, *Electrospun ultralong hierarchical vanadium oxide nanowires with high performance for lithium ion batteries.* Nano Lett, 2010. **10**(11): p. 4750-4755.

106.   Formo, E., E. Lee, D. Campbell, and Y. Xia, *Functionalization of electrospun TiO2 nanofibers with Pt nanoparticles and nanowires for catalytic applications.* Nano Lett, 2008. **8**(2): p. 668-672.

107.   Chuangchote, S., J. Jitputti, T. Sagawa, and S. Yoshikawa, *Photocatalytic activity for hydrogen evolution of electrospun TiO2 nanofibers.* ACS Appl Mater Interfaces, 2009. **1**(5): p. 1140-1143.

108.   Wakayama, H. and Y. Fukushima, Ind. Eng. Chem. Res., 2006. **45**: p. 3328.

109.   Masika, E., R.A. Bourne, T.W. Chamberlain, and R. Mokaya, *Supercritical CO_2 mediated incorporation of Pd onto templated carbons: a route to optimizing the Pd particle size and hydrogen uptake density.* ACS Appl Mater Interfaces, 2013. **5**(12): p. 5639-5647.

110.   Marin, R.P., S. Ishikawa, H. Bahruji, G. Shaw, S.A. Kondrat, P.J. Miedziak, D.J. Morgan, S.H. Taylor, J.K. Bartley, J.K. Edwards, M. Bowker, W. Ueda, and G.J. Hutchings, *Supercritical antisolvent precipitation of TiO2 with tailored anatase/rutile composition for applications in redox catalysis and photocatalysis.* Applied Catalysis a-General, 2015. **504**: p. 62-73.

111.   Da Silva, E.P., M.R. Guilherme, E.T. Tenório-Neto, A.F. Rubira, M.H. Kunita, L. Cardozo-Filho, and C.G. Alonso, *scCO $_2$-based synthesis of semi-crystalline TiO $_2$ nanoparticles: A rapid and direct strategy.* Materials Letters, 2014. **136**: p. 133-137.

112.   Marin, R.P., S. Ishikawa, H. Bahruji, G. Shaw, S.A. Kondrat, P.J. Miedziak, D.J. Morgan, S.H. Taylor, J.K. Bartley, and J.K. Edwards, *Supercritical Antisolvent Precipitation of TiO $_2$ with Tailored Anatase/Rutile Composition for Applications in Redox Catalysis and Photocatalysis.* Applied Catalysis A: General, 2015.

113.   Sui, R. and P. Charpentier, *Synthesis of metal oxide nanostructures by direct sol-gel chemistry in supercritical fluids.* Chem Rev, 2012. **112**(6): p. 3057-3082.

114.   Badawy, W.A., *Preparation, electrochemical, photoelectrochemical and solid-state characteristics of indium-incorporated TiO $_2$ thin films for solar cell fabrication.* Journal of Materials Science, 1997. **32**(18): p. 4979-4984.

115. Liu, Y., G. Chen, C. Zhou, Y. Hu, D. Fu, J. Liu, and Q. Wang, *Higher visible photocatalytic activities of nitrogen doped In_2TiO_5 sensitized by carbon nitride.* J Hazard Mater, 2011. **190**(1-3): p. 75-80.

116. Yu, C.H., C.H. Wu, C.H. Lin, C.H. Hsiao, and C.F. Lin, *Hydrophobicity and molecular weight of humic substances on ultrafiltration fouling and resistance.* Separation and Purification Technology, 2008. **64**(2): p. 206-212.

117. Lee, S. and C.H. Lee, *Effect of membrane properties and pretreatment on flux and NOM rejection in surface water nanofiltration.* Separation and Purification Technology, 2007. **56**(1): p. 1-8.

118. Boussu, K., C. Vandecasteele, and B. Van der Bruggen, *Relation between membrane characteristics and performance in nanofiltration.* Journal of Membrane Science, 2008. **310**(1-2): p. 51-65.

119. Luo, M.L., J.Q. Zhao, W. Tang, and C.S. Pu, *Hydrophilic modification of poly(ether sulfone) ultrafiltration membrane surface by self-assembly of TiO_2 nanoparticles.* Applied Surface Science, 2005. **249**(1-4): p. 76-84.

120. Lind, M.L., A.K. Ghosh, A. Jawor, X. Huang, W. Hou, Y. Yang, and E.M. Hoek, *Influence of zeolite crystal size on zeolite-polyamide thin film nanocomposite membranes.* Langmuir, 2009. **25**(17): p. 10139-10145.

121. Raj, S.A., S. Rajesh, K. Lakshmi, K.H. Shobana, and D. Mohan, *Effect of functionalisation on polysulfone-based ultrafiltration membranes.* International Journal of Nuclear Desalination, 2010. **4**(1): p. 18-27.

122. Steen, M.L., A.C. Jordan, and E.R. Fisher, *Hydrophilic modification of polymeric membranes by low temperature H_2O plasma treatment.* Journal of Membrane Science, 2002. **204**(1-2): p. 341-357.

123. Gilron, J., S. Belfer, P. Väisänen, and M. Nyström, *Effects of surface modification on antifouling and performance properties of reverse osmosis membranes.* Desalination, 2001. **140**(2): p. 167-179.

124. Maximous, N., G. Nakhla, W. Wan, and K. Wong, *Preparation, characterization and performance of Al_2O_3/PES membrane for wastewater filtration.* Journal of Membrane Science, 2009. **341**(1-2): p. 67-75.

125. Maximous, N., G. Nakhla, W. Wan, and K. Wong, *Performance of a novel ZrO_2/PES membrane for wastewater filtration.* Journal of Membrane Science, 2010. **352**(1-2): p. 222-230.

126. Rahimpour, A., S.S. Madaeni, A. Shockravi, and S. Ghorbani, *Preparation and characterization of hydrophile nano-porous polyethersulfone membranes using*

synthesized poly(sulfoxide-amide) as additive in the casting solution. Journal of Membrane Science, 2009. **334**(1-2): p. 64-73.

127.   Blanco, J.F., Q.T. Nguyen, and P. Schaetzel, *Novel hydrophilic membrane materials: Sulfonated polyethersulfone Cardo.* Journal of Membrane Science, 2001. **186**(2): p. 267-279.

128.   Gullinkala, T. and I. Escobar, *Study of the hydrophilic-Enhanced ultrafiltration membrane.* Environmental Progress, 2008. **27**(2): p. 210-217.

129.   Chen, S.H., R.M. Liou, Y.Y. Lin, C.L. Lai, and J.Y. Lai, *Preparation and characterizations of asymmetric sulfonated polysulfone membranes by wet phase inversion method.* European Polymer Journal, 2009. **45**(4): p. 1293-1301.

130.   Lafitte, B. and P. Jannasch, *Polysulfone ionomers functionalized with benzoyl(difluoromethylenephosphonic acid) side chains for proton-conducting fuel-cell membranes.* Journal of Polymer Science, Part A: Polymer Chemistry, 2007. **45**(2): p. 269-283.

131.   Lafitte, B. and P. Jannasch, *Phosphonation of polysulfones via lithiation and reaction with chlorophosphonic acid esters.* Journal of Polymer Science, Part A: Polymer Chemistry, 2005. **43**(2): p. 273-286.

132.   Abu-Thabit, N.Y., S.A. Ali, and S.M. Javaid Zaidi, *New highly phosphonated polysulfone membranes for PEM fuel cells.* Journal of Membrane Science, 2010. **360**(1-2): p. 26-33.

133.   Khulbe, K.C., C. Feng, and T. Matsuura, *The art of surface modification of synthetic polymeric membranes.* Journal of Applied Polymer Science, 2010. **115**(2): p. 855-895.

134.   Guiver, M.D., S. Croteau, J.D. Hazlett, and O. Kutowy, *Synthesis and characterization of carboxylated polysulfones.* British Polymer Journal, 1990. **23**(1-2): p. 29-39.

135.   Van Der Bruggen, B., *Chemical modification of polyethersulfone nanofiltration membranes: A review.* Journal of Applied Polymer Science, 2009. **114**(1): p. 630-642.

Chapter 3

3 Cu_2O /TiO_2 Nanowires using Supercritical CO_2 for Photocatalytic Hydrogen Production

This work reports a novel method using supercritical CO_2 ($ScCO_2$) to synthesize copper (I)-titania nanowires for sacrificial hydrogen production. The doped titania nanowires were prepared using a unique sol-gel methodology in $ScCO_2$ using titanium alkoxide, metal dopant, and acetic acid as the polycondensation agent. This methodology produced uniformly dispersed dopants integrated into nanowires with diameters of 80-100 nm and aspect ratios of 15-25 as observed by SEM. XPS and XANES results confirmed the presence of a single oxidation state of Cu (I). The photocatalytic activity of the prepared nanowires was tested using formaldehyde as a sacrificial agent for hydrogen production in water with solar light irradiation at 100 mW/cm^2. The copper doped titania showed superior performance compared to other catalysts with 13 times the hydrogen production compared to Degussa P25 and 47 times more than from un-doped titanium dioxide nanowires. The results are attributed to the Cu (I) oxidation state, high aspect ratio nanowires providing access to active sites, and higher dopant dispersion

3.1   Introduction

In recent years, solar photocatalytic processes are gaining attention for their potential in hydrogen production using water splitting and sacrificial agents.[1] Nano-sized TiO_2 is widely examined for water and wastewater photocatalytic treatment and water splitting for hydrogen production, due to its numerous beneficial aspects including high chemical and thermal stability, non-corrosivity, abundance, and cost effectiveness.[2-4] However, the main barriers of implementing TiO_2 at large scale are the rapid recombination of photo-generated electron/hole pairs and the poor activation of TiO_2 by visible light.[5, 6] Prior investigations showed that doping TiO_2 using various noble and transition metals such as Pt, Au, Pd, Rh, Ni, Cu, Ag, etc. greatly reduces the possibility of electron-hole recombination, resulting in efficient electron-hole separation and stronger photocatalytic

activity of TiO_2.[7] [8] Recent studies have shown that sacrificial reagents such as methanol or formaldehyde can inhibit rapid recombination of electron/hole pairs by utilizing the electrons for oxidation.[9] Doping TiO_2 also induces a red shift in the absorption spectrum, making it possible for visible light activation to enhance the energy harvesting efficiency of TiO_2.[10]

In particular, copper doped titania has gained significant interest for sacrificial hydrogen production compared to rare and expensive noble metals due to its adequate band gap and band edge position in addition to its cost effectiveness and abundance.[11] Work in 1998 by Hara et al. highlighted the potential of using Cu_2O under visible light to produce hydrogen. [12] Banadra et al. (2005) attributed the sacrificial hydrogen production to CuO, which effectively transferred photogenerated electrons to the copper (II) oxide surface, where water reduction took place.[13] Wu et al. (2009) prepared copper doped TiO_2 nanoparticles of mixed copper oxides by a wet impregnation method and tested for hydrogen production using a methanol-water mixture. Although mixed copper oxide doped TiO_2 were photocatalytically active, it was later found that Cu_2O doped titania is the most active oxide for photocatalytic hydrogen production.[14] Recently, a more detailed study of Cu_2O doped TiO_2 produced by hydrogen reduction of a Cu-Cu_2O core-shell structure showed that Cu (I) exhibited higher photocatalytic activities compared to Cu (II).[15] In addition to core-shell nanostructures, most currently prepared Cu doped TiO_2 morphologies are nanoparticles,[16] nanofilms,[17] hollow spheres,[18] and nanorods.[19] Nanoparticles are primarily used due to their relatively high surface areas to facilitate reactions. Conversely, nanowires provide direct paths for electron transport compared to the random tortuous paths in nanoparticles,[20] and are of great interest to examine sacrificial hydrogen production to probe the catalytic mechanism.

Current techniques to make nanowires include the supercritical fluid liquid-solid mechanism SF-S-L used by the Korgel research group, [21] and vapor-liquid-solid method (V-L-S) by Lieber's research group. [22] However, challenges of these techniques are in making porous materials with high surface area with various metal oxides, such as titania, which would be suitable as catalysts for hydrogen production. Recently, supercritical carbon dioxide ($ScCO_2$) has been shown to provide high aspect

ratio nanofibers/wires of titania with high surface area and porosity.[23] $ScCO_2$ is an inexpensive and green alternative to conventional organic solvents; it is environmentally benign and non-flammable with low viscosity, zero surface tension and high diffusivity, which are favorable for synthesizing fine and uniform nanomaterials with porous nanostructure.[24]

In light of the above discussion, the objective of this work was to synthesize Cu doped TiO_2 nanowires using a $ScCO_2$ sol-gel process for sacrificial hydrogen production. To the best of our knowledge, the ability to produce pure Cu (I) doped titania has not been reported in the literature. The performances of produced catalysts were compared with commercial nanoTiO_2 particles (P25) and undoped TiO_2 nanowires.

3.2   Experimental Details

3.2.1   Chemicals and Materials

Titanium (IV) isopropoxide (TIP) (97%), acetic acid (99.7%), copper (II) acetylacetonate (acac) (99.99%), copper (II) 2-ethylhexanoate (97%), copper (II) methoxide (97%), and formaldehyde solution (36.5%) were purchased from the Aldrich Chemical Company (Oakville, ON, Canada and used without further purification). Instrument grade liquid carbon dioxide (99.99%) from Air Liquide Canada was delivered by a syringe pump (Isco 260D) into a 10 mL view cell reactor equipped with a pressure transducer, heating tape and thermocouple for temperature control. The details of the reactor are provided in Lucky et al.[25]

3.2.2   Synthesis of Cu (I) doped TiO_2 nanowires

In a typical experiment, predetermined amounts of titanium isopropoxide (TIP) and desired copper precursor were quickly placed in a 10 mL view cell, followed by addition of acetic acid and CO_2, except for undoped TiO_2 nanowires in which no copper precursor was added. The view cell was heated to 60 ℃ and subsequently pressurized to 5000 psig. A magnetic stirrer was used to ensure uniform mixing of the reactants. The hydrolysis rate was controlled by adjusting metal precursors to acetic acid molar ratios in the range of 1:5-6. During the gelation stage, a dark blue color was observed in about 30 and 40

minutes, which gradually became lighter with time during aging. After five days of aging, the samples were washed with 100 mL of $ScCO_2$ at a rate of 0.3 mL/min to remove unreacted materials and by-products, and to prevent collapse of the gel network. The prepared copper-doped TiO_2 sol-gel was then calcined in air at 500 °C for 2 hours. The calcination temperature was selected based on the thermal gravimetric analysis (TGA) (results not shown) where removal of organic components occurred at 317 ºC.

3.2.3   Characterization of Cu doped TiO_2 Nanowires

The synthesized nanowires' morphology was characterized by Scanning Electron Microscopy (SEM) (Model LEO 1530) and Transmission Electron Microscopy (TEM) (Model JEOL 2010F) capable of dark field scanning transmission electron microscopy (STEM) coupled with energy dispersive X-ray spectroscopy. Samples for SEM imaging were prepared by applying the powder directly to a carbon adhesive tape. For TEM analysis, the powdered samples were dispersed in ethanol by sonication for 15 min and then cast on a copper grid covered with holey carbon film. The BET (Brunauer-Emmett-Teller) surface area and BJH (Barrett-Joyner-Halenda) pore size and volume analysis were determined from nitrogen adsorption and desorption isotherm data obtained at 77 K with a constant-volume adsorption apparatus (Micromeritic Tristar II) using N_2 gas (99.995% pure obtained from Praxair, Canada). The prepared samples were degassed at 150°C overnight before measurements. Structural analysis of the samples was performed using an X-ray powder diffractometer (Rigaku Miniflex XRD, Texas, U.S.A.), fitted with a rotating sample holder, a scintillation counter detector and a divergent beam utilizing a Cu K source of X-rays (= 1.5418 °A). The XPS analysis was carried out with a Kratos Axis Ultra spectrometer using a monochromatic Al K (alpha) source (15mA, 14kV).

3.2.4   Photocatalytic Hydrogen Production

The experimental setup for photocatalytic sacrificial hydrogen production was reported previously. [26] A pyrex glass photocatalytic reactor (11 cm x 6.3 cm) with a volume of 350 ml was used to carry out the experiments. The majority of experiments were conducted using 50 mg of photocatalyst in 50 ml formaldehyde (0.16 M) solution. Prior to solar irradiation, the solution was agitated at 500 rpm using a magnetic stirrer

(Heidolph) for 1 hour with simultaneous nitrogen purging at ambient pressure to eliminate oxygen from the solution. The reactor contents were irradiated using a solar simulator (model: SS1 KW, Sciencetech). The solar lamp produces irradiance at 100 mWcm^{-2} at full power (1000 watts), which is similar to the global solar spectrum at sea level. The photocatalytic reactor was air-cooled with an electric fan to keep the temperature constant at ambient conditions. A Gas Chromatography (Schimadzu GC 2014, Heyesep D packed column: 10 m length, 2 mm ID, and 2 µm film thickness, with thermal conductivity detector (TCD)) was utilized for quantification of produced hydrogen. The calibration of the GC was conducted using a 1000 ml gas-sampling bulb (Supelco), which was filled with nitrogen and hydrogen to yield hydrogen calibration gas with desired concentrations.

3.3   Results and Discussion

3.3.1   Morphology and Compositional Characterization of Nanowires

Both undoped TiO_2 nanowires and those doped with Cu were synthesized to compare their morphology and photocatalytic activity to provide a better understanding of the effect of copper doping. The morphology of the undoped titanium is clearly a nanowire morphology with high porosity and high aspect ratio as shown in Figure 3-1a. Further characterization was carried out by TEM with a high magnification random site shown in the inset of Figure 3-1b. A single fast fourier transform (FFT) diffraction pattern is observed showing the diffraction pattern of a single titania crystal. Figure 3-1c was constructed by inverse FFT diffraction of the selected site to calculate the lattice distance of the undoped TiO_2 nanowires, which are about 0.35nm as shown in Figure 3-1d, which is in agreement with literature values for titania.
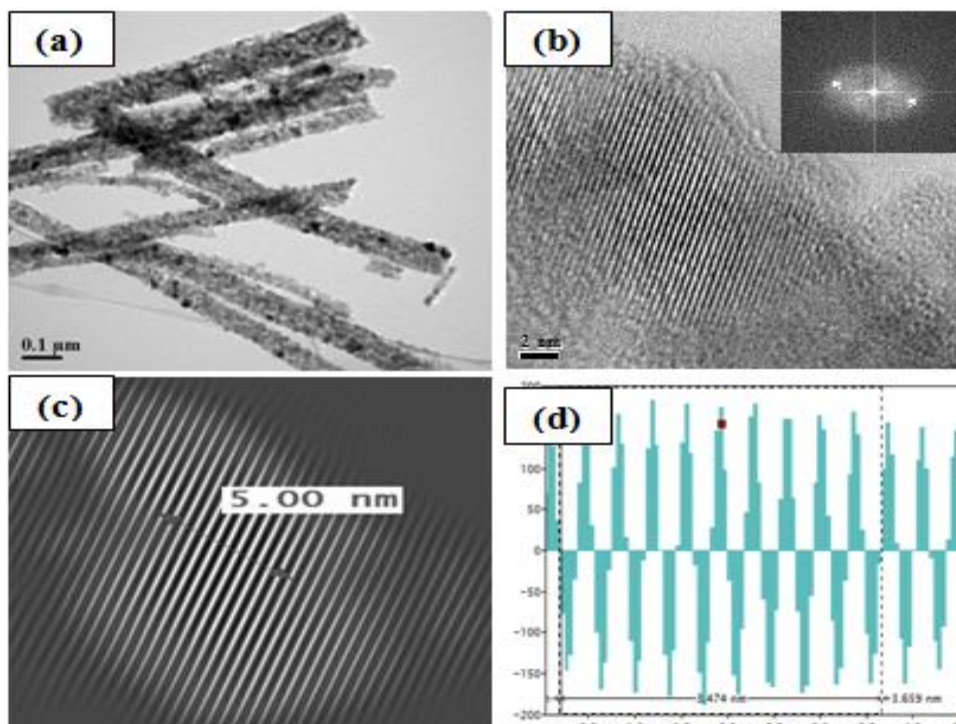
Figure 3-1: High resolution TEM image of undoped TiO_2 nanowires (a), TEM image of single nanowire with FFT diffraction (b), inverse FFT (c), histogram of lattice in figure c (d).

Cu doped TiO_2 nanowires were successfully prepared by the $ScCO_2$ sol-gel synthesis methodology by testing three different precursors (copper (II) Acetylacetonate, copper (II) 2-ethylhexanoate, and copper (II) methoxide) with acetic acid at 60 ℃ and 5000 psi. The produced materials were characterized by FTIR as shown in Figure 3-2, which shows 5 mol % copper doping with TIP. However, copper (II) acetylacetonate was selected due to its higher surface area compared with the rest of precursors and its uniform nanowire formation. The FTIR of each precursor with TIP and its product are provided in the Appendix.
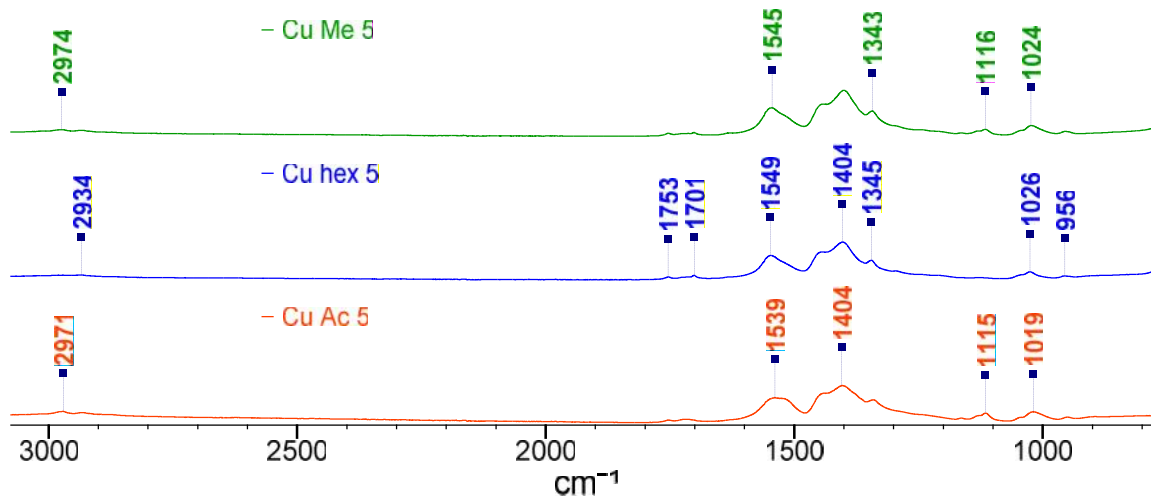
Figure 3-2: FTIR spectra of produced copper doped nanowires with different precursor, copper (II) methoxide (green), copper (II) 2-ethylhexanoate (blue), copper (II) Acetylacetonate (red), reacted with TIP and acetic acid at 60 ºC, 5000 psi.

Copper doped nanowires were successfully prepared by the $ScCO_2$ sol-gel method by mixing the copper (II) acetylacetonate and titanium precursors at 1%, 2%, and 5 mol % of Cu in TiO_2. These samples gave copper doping levels of 0.9, 2, and 5.6 atomic % after calcination, respectively. For simplicity, these samples will be referred to as CuAc1, CuAc2, and CuAc5, respectively. Hereafter, the undoped titanium dioxide nanowire will be referred as TiNW.

The morphology of the synthesized Cu doped TiO_2 nanowires were determined by SEM and TEM with a typical sample shown in Figure 3-3. The TEM image shown in Figure 3-3d indicates that these nanowires are uniform, porous and have high aspect ratios. FTIR results also showed the typical peaks of C=O asymmetric stretching 1701 cm^{-1} at and the symmetric stretching at 1404 to 1345 cm^{-1} as shown in Figure 3-4 for CuAc1, CuAc2, and CuAc5.

48
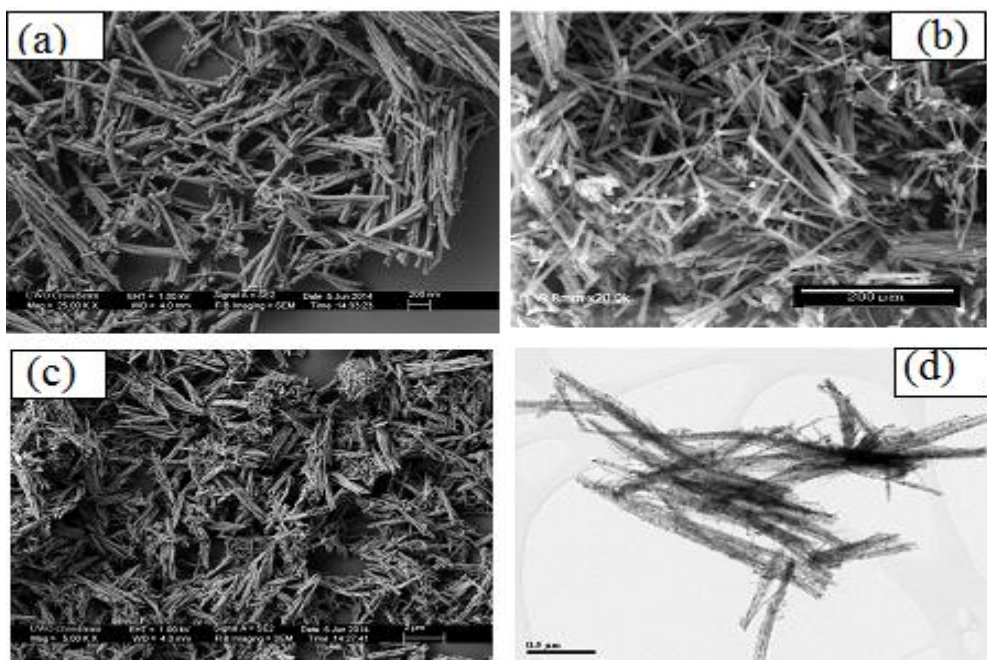
Figure 3-3: SEM images of copper doped TiO_2 nanowires (a), another SEM for copper doped TiO_2 nanowires (b), SEM image of undoped TiO_2 nanowires (c) TEM image of copper doped TiO_2 nanowire(d).Reaction conditions: selected mmole copper acetylacetonate, 10 mmole TIP, 60 mmole acetic acid, 5 ml of CO_2, temp 60 °C and pressure 5000 psi.
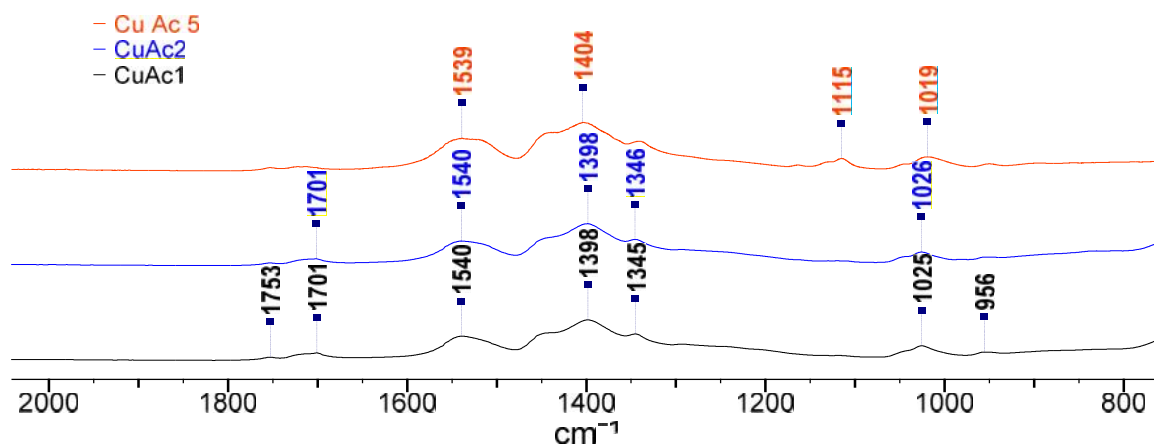
Figure 3-4: FTIR spectra of produced copper doped nanowires using copper (II) Acetylacetonate as precursor for CuAc5 (red), CuAc2 (blue), and CuAc1 (black).

The ScCO$_2$ sol-gel is a reproducible method for doping material with excellent dispersion providing good control of the surface parameters critical for nanomaterials. One of the criteria for controlling the selectivity of producing nanowires over nanoparticles is the alkoxide to acetic acid ratio. Nanowires can be produced with alkoxide to acetic acid ratio greater than 4.5 which was optimized in previous work by the Charpentier group.[25]

Figure 3-3 shows the distribution of diameter and aspect ratio of the produced Cu-TiO$_2$ nanowires determined from the SEM analyses. Nanowire structure was clearly observed for all bimetallic nanomaterials with high aspect ratios (R= length/diameter), mostly in the range of 15 to 25, with diameter distributions ranging from 50 to 150 nm.
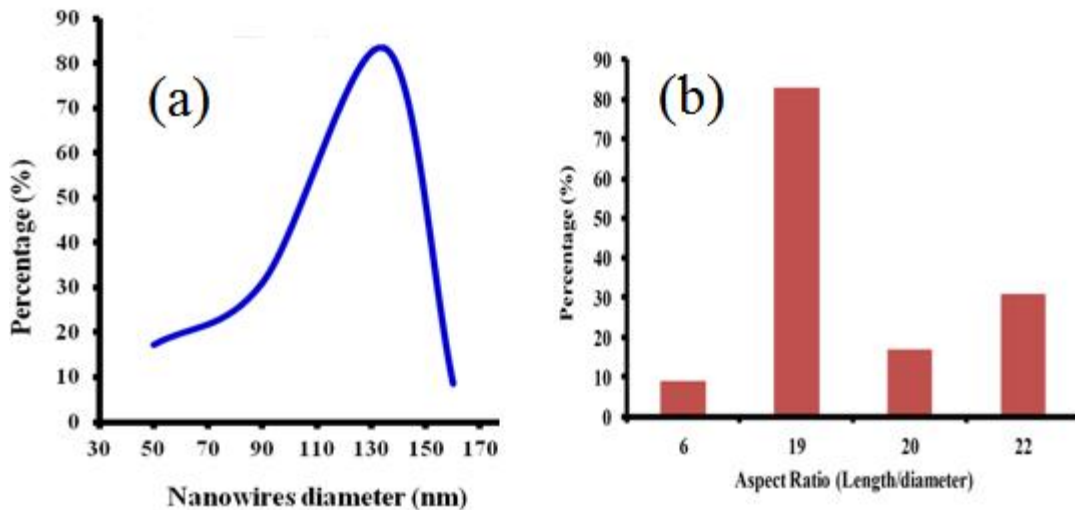
Figure 3-3: Copper doped TiO$_2$ nanowires: (a) diameter distribution and (b) aspect ratio distribution.

Doping with copper did not change the titanium nanowires morphology, which still gave high aspect ratio's, porous nanowires with an excellent dispersion of copper. This was confirmed by TEM metal mapping of Cu/TiO$_2$ nanowires as shown in Figure 3-4a. Higher magnifications of the specified location are shown in Figure 3-4b. Figure 3-4c shows the lattice distance of about 0.35 nm as summarized in the histogram shown in Figure 3-4d.
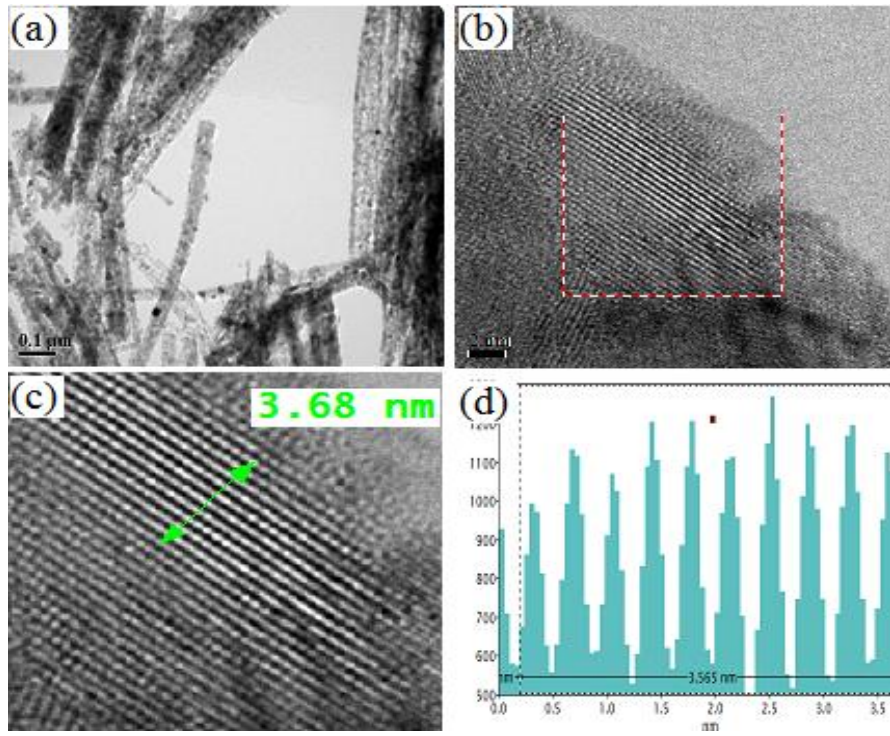
Figure 3-4: High resolution TEM images of Cu doped TiO_2 nanowires CuAc1 (a), high magnification of figure a (b-c), histogram of lattice (d).

The similarity of lattice distances between TiNW and CuAc1 and CuAc2 is an excellent indication of no agglomeration of copper at specific sites. However, the copper doped nanowires showed a slight change of morphology at the highest doping level for CuAc5. At copper doping of 5.6 atomic %, formation of nanoparticles about 2 nm on the surface of the nanowires started to form as shown in Figure 3-5.
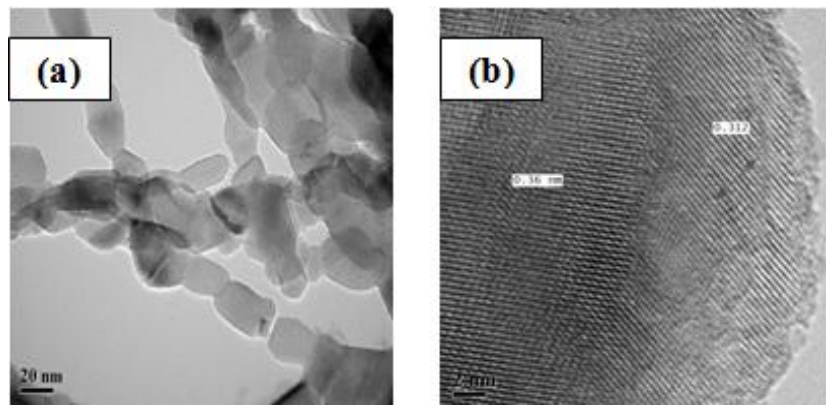
Figure 3-5: TEM image of CuAc5 (5 Atomic % doped TiO_2 nanowires) (a) and high resolution of selected area (b).

To illustrate the degree of Cu dopant metal dispersion throughout the nanowires, TEM mapping using energy dispersive X-ray spectroscopy (EDS) is shown for the copper doped TiO_2 in Figure 3-6. Uniform dispersion of Cu throughout the nanowires for samples CuAc1 and CuAc2 can be seen, whereas copper nanoparticles are clearly observed due to the higher loading of copper in CuAc5, which is also reported in the literature but at a lower loading. [27] These results show good dispersion of copper throughout the TiO_2 structure, which is attributed to the adopted synthesis methodology utilizing $ScCO_2$ as a solvent and drying agent, which helped in enhancing the precursors' solubility, preventing collapse of the formed networks during gelation due to the zero surface tension of $ScCO_2$ during the aging and washing stages, as described in detail previously.[28]
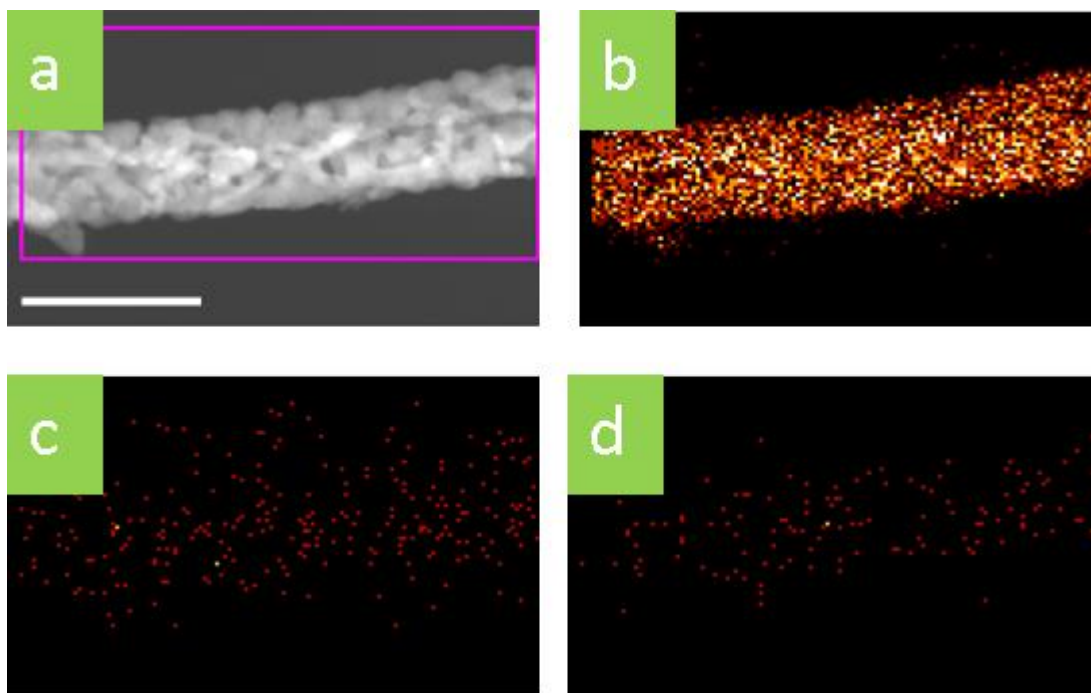
Figure 3-6: STEM image of copper doped TiO_2 nanowires showing porosity of nanowire (a), and EDS mapping showing dispersion of titanium (b), oxygen (c) and copper (d) within a nanowire. The bar scale is 100 nm.

The surface area of a material decreases with increasing dimensionality. For example, nanoparticles have higher surface areas compared to nanorods and nanowires.[19, 29]

Despite the nanowires structure, the produced nanowires have comparable surface areas to Degussa P25 (also examined in this work for hydrogen production) (50 m^2/g). The BET surface area of undoped TiO_2 nanowires were measured to be 58 m^2/g and copper doped nanowires ranged between 31 to 49 m^2/g. The relatively high surface area of nanowires can be attributed to pore formation during the sol-gel synthesis of nanowires and more crucially retaining of the pores by $ScCO_2$ during the drying stage. The Barrett-Joyner-Halenda (BJH) nitrogen adsorption-desorption isotherm provides a more detailed understanding of the porosity (pore volumes and pore areas) compared to BET analysis. The isotherms of the undoped TiO_2 and copper doped TiO_2 nanowires are shown in Figure 3-7, indicating a typical type IV isotherm.[15] The Cu doped sample shows an average adsorption pore size of 8.2 nm with a pore volume of 0.12 cm^3/g and pore area of 59 m^2/g.
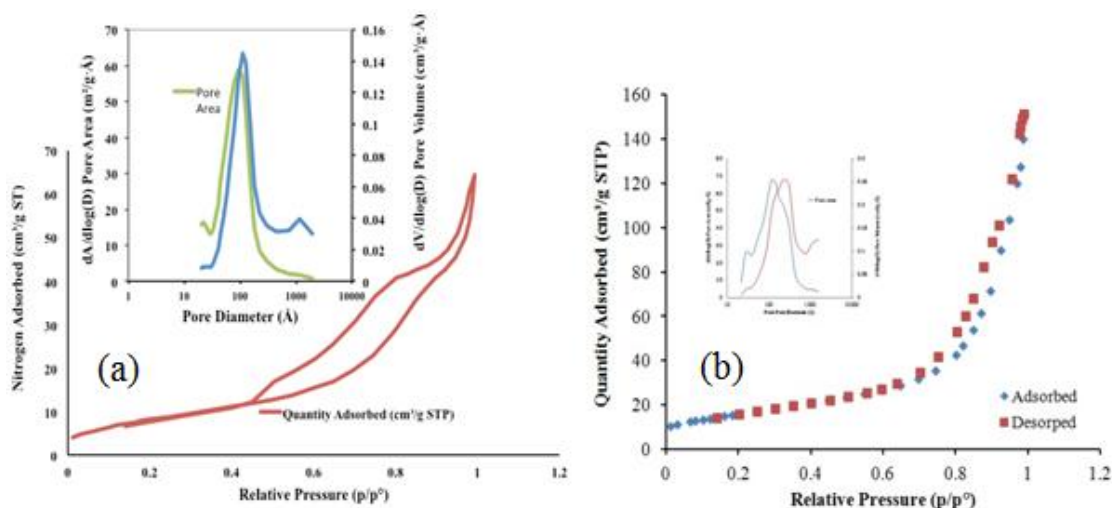
Figure 3-7: (a) Nitrogen isotherms of copper doped titanium nanowires. Pore volume and pore area distribution are shown in the insertion, (b) Nitrogen isotherms of indium doped titanium nanowires. Pore volume and area distribution are shown in the insertion.

The XRD analysis of the nanowires is shown in Figure 3-8. The calcined samples showed a highly crystalline structure and clear formation of anatase structures with traces of rutile after treatment at 500 °C. The XRD spectra of the Cu_2O-TiO_2 nanowires indicate that TiO_2 is in mainly the anatase phase. A gradual increase of the characteristic peaks at 27^0

that is related to rutile was observed as the concentration of copper dopant increased. In addition, smaller peaks were noticed in the area between 35^0 and 45^0. The peaks at 36.1^0, 38.6^0, 44.1^0, correspond to copper doping as their intensity increased with an increase in copper loading. However the sample CuAc5 shows additional X-ray features that reflect the contribution of copper, complementing the TEM image of specific site of copper (quantum dot) on the surface of titanium dioxide consistent with the TEM results.
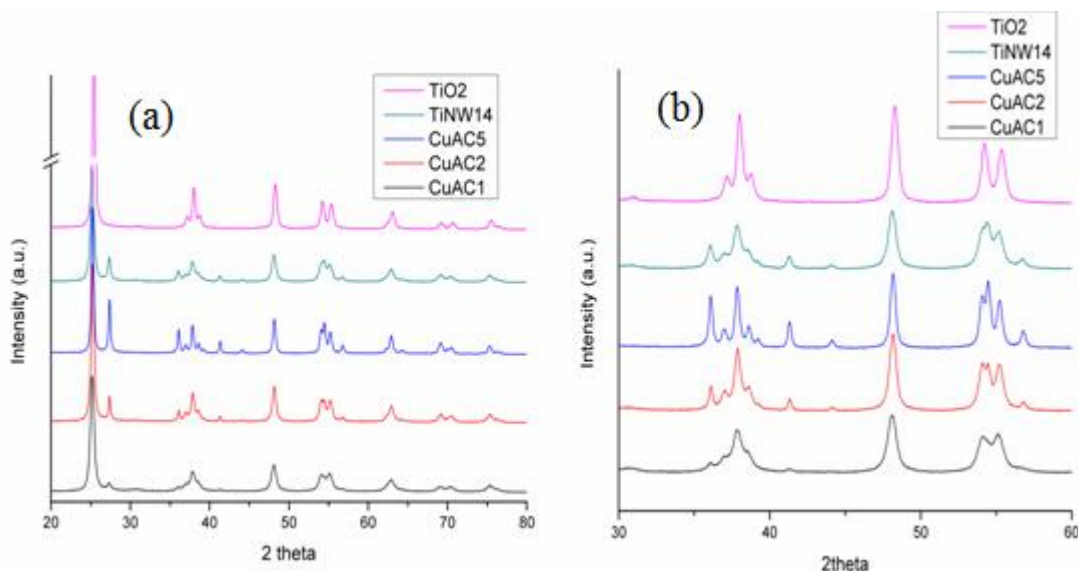
Figure 3-8: XRD results (a) of anatase titanium dioxide, Titanium dioxide nanowires, and copper doped TiO_2 nanowires (b) zoom of selected range of (a).

Both the chemical oxidation state of copper and titanium and their concentrations were determined by XPS analysis (Figure 3-9a). In all the prepared titania nanowires, copper and titanium were detected. Titanium was confirmed as Ti (IV) with a binding energy Ti 2p3/2 of 458.66 eV and symmetrical peak, which indicates the absence of any traces of titanium (III). Its binding energy peak slightly shifts in the range of 455.15 - 458.68 eV, depending on its interaction with copper (Figure 3-9b). However, in sample CuAc5, which has about 5.6 atomic % Cu, the titanium peak shifts slightly to 458.74 eV. Oxygen peak for all TiNW, CuAc1 and CuAc2 was noticed at 526.55 eV, for CuAc5 sample, it occurs at 527.25 eV which could be attributed to the formation of 12 % Cu (II) as it was confirmed by high resolution XPS in which a shake-up peak is observed between 940-

945 eV as shown in Figure 3-9b. However, none of the other copper doped samples had any amount of Cu (II) as indicated by XPS.
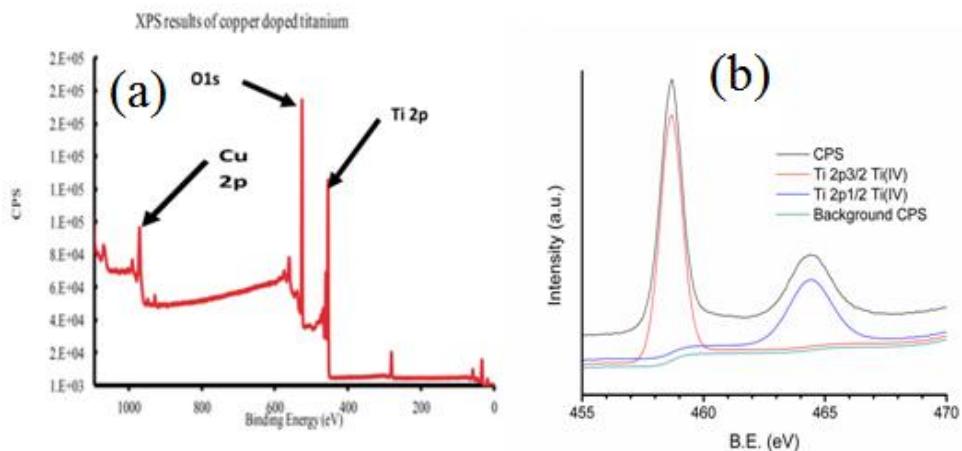
Figure 3-9: XPS results of copper doped TiO$_2$ nanowires. (a) General scans and (b) shows Ti deconvolution.

The copper doped TiO$_2$ sample showed a characteristic binding energy peak of Cu 2p$_{3/2}$ at 932.58 eV, which indicates the existence of Cu (I) in sample CuAc1 and CuAc2. The absence of shakeup peak around Cu 2p$_{3/2}$ 942 eV in both samples confirms that no Cu (II) species is present in these samples, [30] as shown in the deconvoluted XPS spectrum in Figure 3-10a. Furthermore, a shift to higher binding energy was observed as the copper concentration increases (Figure 3-10).
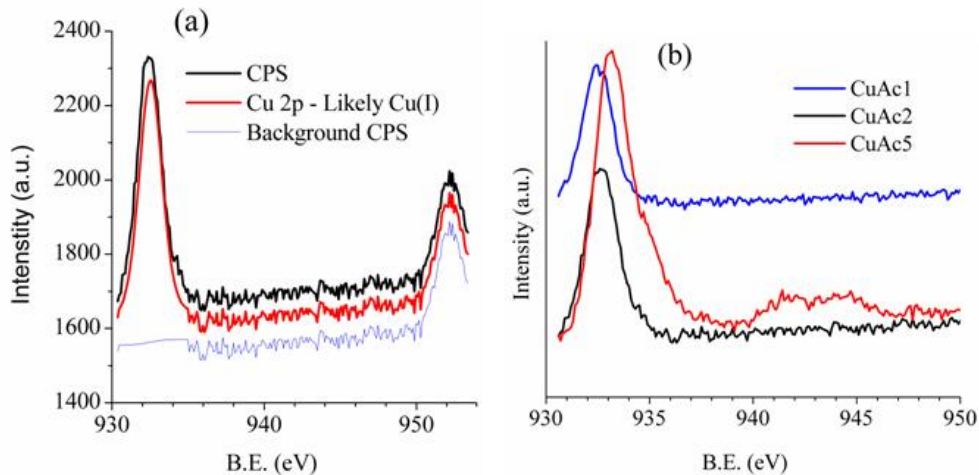
Figure 3-10: XPS results of copper doped TiO_2 nanowires. (a) shows copper deconvolution peak, (b) shows an increase of binding energy as copper concentration increases.

3.3.2   XANES and EXAFS

Figure 3-11a shows the normalized Ti L3,2-edge XANES of the copper doped TiO_2 nanowires in comparison with anatase and rutile TiO_2 (> 99.7 %, Sigma-Aldrich), which probes the transitions from Ti $2p_{3/2}$ and $2p_{1/2}$ states to unoccupied $3d_{5/2}$ and $2p_{3/2}$ states. For anatase and rutile TiO_2, the features in the XANES spectra are due to the splitting pattern (t2g and eg) of the energy of the *d* orbitals under an octahedral crystal field followed by local distortion that leads to different local symmetries for anatase (*D*2d) and rutile (*D*2h). It can be seen that the most striking difference is the intensity ratio between feature e_{11} and e_{12}, that is, feature e_{11} is dominant in anatase while feature e_{12} is dominant in rutile. The lowering of the *O*h symmetry to *D*2d and *D*2h leads to the $2p \qquad$ eg transition further splitting into peak e_{11} and e_{12} at the L3-edge. The symmetry variations between anatase and rutile have an impact on the eg state; therefore, we can track anatase and rutile phases via the relative ratio between features e_{11} and e_{12}. [31] The XANES of the Cu doped TiO_2 nanowires (black curve) illustrates well-resolved features of anatase TiO2 that is confidently identified via the intensity ratio between e_{11} and e_{12}. It indicates that the Cu doped TiO_2 nanowires are of anatase phase, which is consistent with the XRD results. Compared to the standard anatase (blue curve), the peaks in Cu doped TiO_2 are broadened, which is due to the porous structure of the Cu doped TiO_2 nanowires (Figure 3-11a). Ti $L_{3,2}$-edge XANES results of the Cu doped TiO_2 nanowires agree well with

their XRD results. Figure 3-11b shows the Cu L_3-edge XANES spectrum of the Cu doped TiO_2 nanowires. The resonances arise from Cu $2p_{3/2}$ to $3d$, $4s$ transitions. The spectrum displays the same features as that of Cu_2O which suggests that the doped Cu in the TiO_2 nanowires exists as Cu^{1+}, which is consistent with the XPS data. [32, 33]
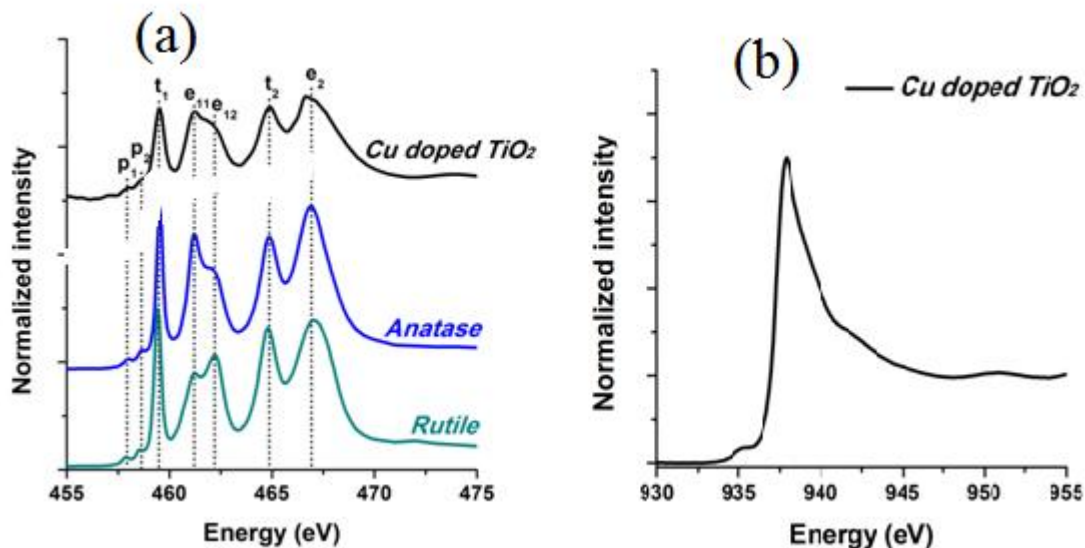
Figure 3-11: (a) TEY XANES spectra of Cu doped and In doped TiO_2 nanowires at Ti L3,2-edge. The spectra of standard TiO_2 of anatase and rutile phase are also shown for comparison. (b) TEY XANES spectrum of the Cu doped TiO_2 nanowires at Cu L_3-edge.

3.3.3 Photocatalytic Hydrogen Production over Cu_2O/TiO_2 Nanowires

The photocatalytic performance of the Cu doped TiO_2 nanowires was compared to that of P25 and undoped TiO_2 nanowires using formaldehyde as the sacrificial agent for hydrogen production under solar light (100 mW/cm^2). The sacrificial agent loading was optimized by testing hydrogen production using 0.06 M, 0.16 M and 0.24 M formaldehyde and it was found that 0.16 M produced the highest hydrogen using CuAc1 as shown in Figure 3-12.
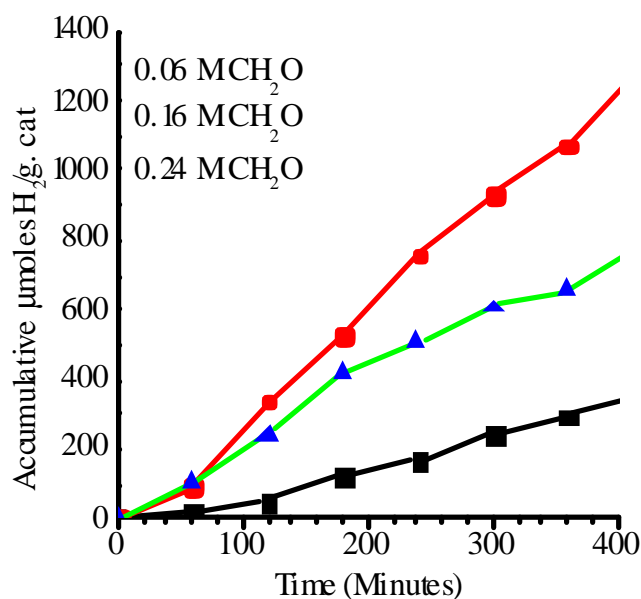
Figure 3-12: Effect of formaldehyde concentration on hydrogen production under solar light using CuAc1 as photocatalyst.

The results show that Cu_2O/TiO_2 nanowires at different levels of doping produced the highest amount of hydrogen followed by Degussa P25, followed by undoped TiO_2 nanowires. Both undoped catalysts showed a lower rate of hydrogen generation compared to the copper doped nanowires. The highest rate of about 9 µmoles of hydrogen per minute was obtained by sample CuAc1. Although the initial rates of hydrogen production for all the nanowires leveled off after about 120 minutes, the range of hydrogen production for Degussa P25 decreased with time. On the other hand, the copper doped nanowires were stable for about 7 hours of operation. Low hydrogen production using the undoped catalysts is attributed to higher band gap of 3.2 eV compared to 1.7-2.2 of Cu_2O/TiO_2 with a higher position conduction band compared to pristine TiO_2, and effective separation of electron-hole as copper works as a co-catalyst. As shown in Figure 3-13a, the rate of hydrogen production utilizing Cu_2O/TiO_2 in the 0.16 M formaldehyde solution increased to about 9 µmoles of H_2 g cat. $^{-1}$ per minutes and remained constant for 7 hours. The cumulative hydrogen generation using CuAc1 was about 10 times higher than that of P25, and about 47 greater than that of TiNW (undoped TiO_2 nanowires).

This result is a promising start for further development of the Cu_2O/TiO_2 nanowires, especially compared to platinum, gold or other expensive dopants. [26] The most recent $CuOx-TiO_2$ study conducted by Wang et al (2013) showed that the active species for hydrogen production was Cu (I), with Cu (II) having a negative effect on hydrogen production.[34] In that study, 1.3 µmoles g^{-1} of H_2 was produced using 42 wt% copper doped TiO_2 with a 300 W Xe lamp. In this study, 9 µmoles g^{-1} per min of H_2 was produced using a much lower copper loading of 2.3 wt% and solar light of 100 mW/cm^2. The better results in this study are attributed to the single active oxide of Cu (I) using the produced nanowires. In addition, the presence of mixed copper oxide in the study of Wang et al. (2013) indicated a lag time of 5 hours before hydrogen production was started. [34] This was not the case in this study, as instantaneous hydrogen production was observed with all copper doped nanowires.
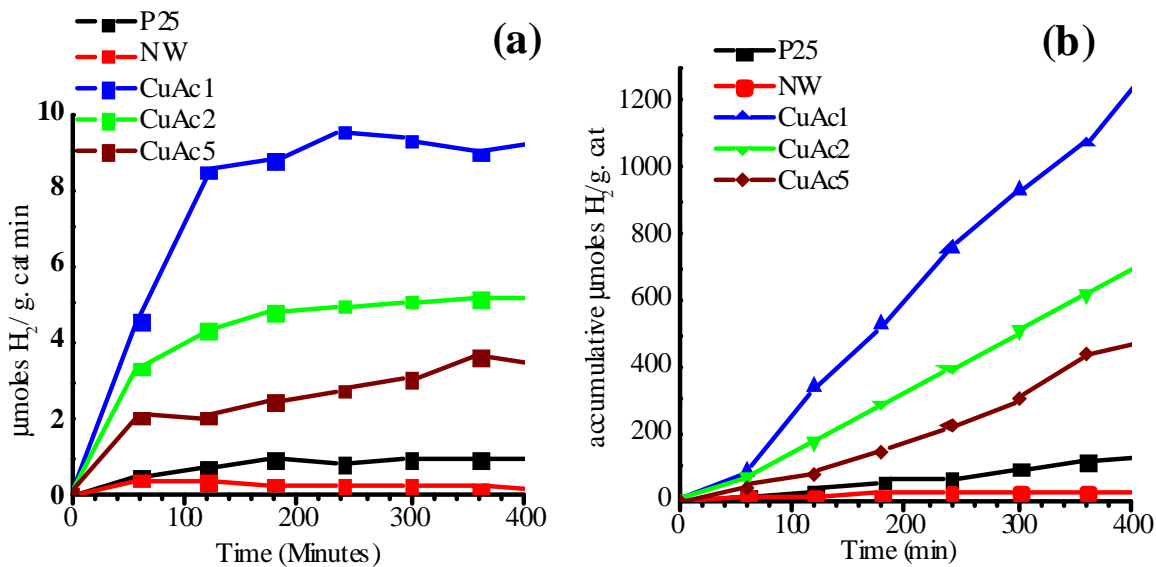
Figure 3-13: Four Replicated experimental results depicting (a) H_2 production rate µmole/min (b) H_2 production µmole per gram of photocatalyst. Photocatalytic study: TiO_2 Degussa P25, undoped TiO_2 nanowires (NW), Cu_2O/TiO_2 nanowires (CuAc1, CuAc2, CuAc5). [HCHO] = 0.16 M, photocatalyst concentration: 1 g/L, light intensity: 100 mW/cm^2.

In further explanation of the mechanism based on our experimental data, the H_2 production from formaldehyde may be described by the following two equations.[2]

h ,catalyst

$$CH_2O + H_2O \xrightarrow{\hspace{2cm}} HCOOH + H_2 \quad \text{----------------------------- (1)}$$

$$HCOOH \xrightarrow{\text{h ,catalyst}} CO_2 + H_2 \quad \text{-------------------------------- (2)}$$
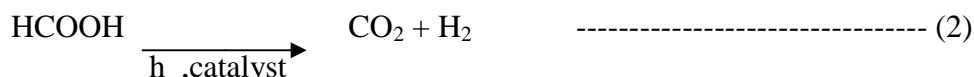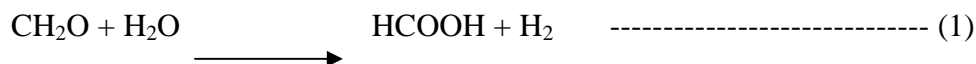
According to these equations, a maximum of 3.9×10^{-5} moles (1.17 mg) of HCHO was consumed in 7 hours using the bimetallic Cu_2O/TiO_2 catalyst, while reactions with P25 TiO_2 resulted in the consumption of 2.72×10^{-5} moles (0.82 mg) of HCHO. This implies that HCHO was always in excess in solution to maintain the rate of hydrogen production constant. Production of formic acid in the solution was confirmed by the decrease in solution pH from almost neutral pH to 6.6-3.8, based on the type of catalyst used. Based on the experimental pH drop and using equation 2, a theoretical estimation showed a 0.7, 1.5 and 2.7 μmoles of HCOOH production in reactions with Cu_2O/TiO_2, TiNW and P25, respectively. However, the total amount of hydrogen produced was 1304, 728, and 478 μmoles g^{-1} for CuAc1, CuAc2 and CuAc5, respectively (Figure 3-13b). These were compared to P25, and undoped titanium nanowires, which produced 130 and 28 μmoles g^{-1}, respectively. It is possible that some CO_2 produced following equation 2 will dissolve and works as a buffer. Therefore, the copper doped nanowires were also the most effective catalyst for higher extents of mineralization of formaldehyde, which is explained by the smallest drop in pH for CuAc1.

Copper stability is a critical parameter for long term use of this catalyst. It was noticed in the literature that deactivation of Cu catalyst occurred resulting in lag time due to the conversion of copper from one oxidation state to anther or to metallic copper. In this work, stability of the doped copper titanium nanowires was tested by conducting cyclic sacrificial hydrogen production experiments for three times as shown in Figure 3-14. The consistent rate and extent of hydrogen production indicated excellent stability of the produced catalysts.
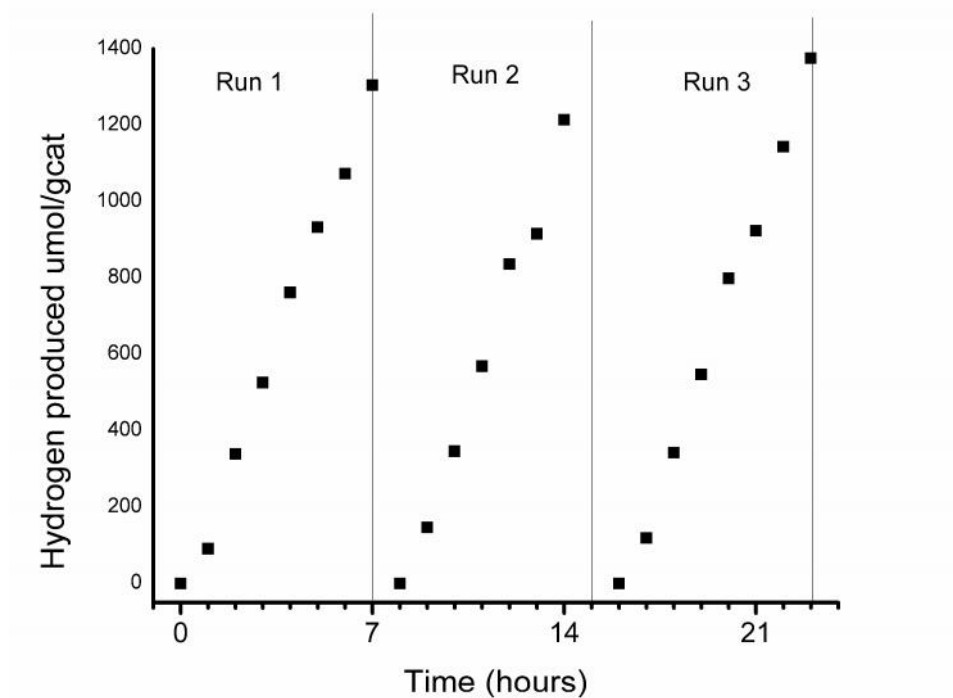
Figure 3-14: Cyclic photocatalytic study for hydrogen production using 1 % Cu doped TiO$_2$ nanowire (CuAc1), [HCHO] = 0.16 M, photocatalyst concentration: 1 g/L, light intensity: 100 mW/cm^2.

Maximum hydrogen production rate produced in this study was compared with those available in literature as shown in Figure 3-15. In the study of Chowdhury et al. (2013), 0.25% Pt doped P25 catalyst showed the maximum hydrogen production of 180 μmoles g^{-1} hr^{-1}as compared to 120 μmoles g^{-1} hr^{-1}for 1.5% Cu$_2$O/TiO$_2$ obtained in this work. However, several disadvantages of Pt are well known in environmental applications, including its scarcity and high cost.[35]
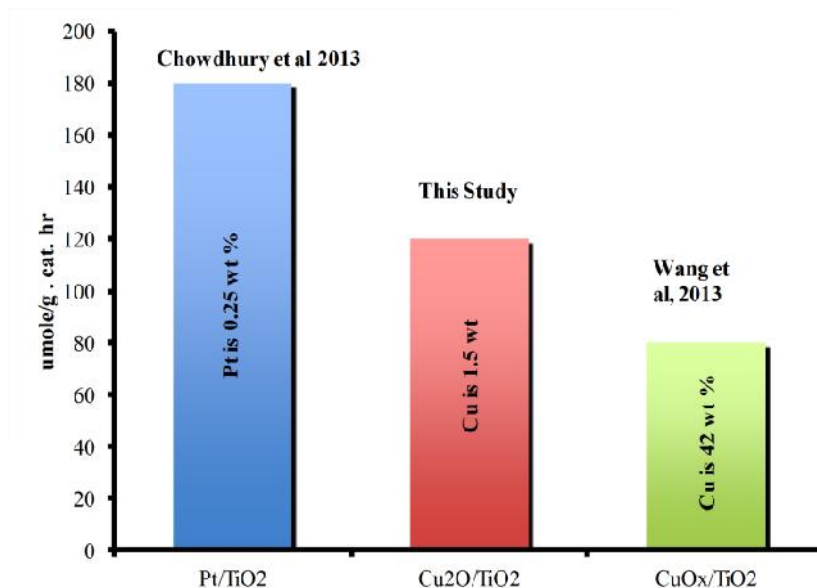
Figure 3-15: H_2 production per gram of catalyst per hour for the latest published studies.

The apparent quantum yield was also calculated over the active solar region of (300-650 nm) for the doped catalysts following equation (3). [36]   Average quantum yield of copper doped titanium nanowires was 55% higher than that of the quantum yield of P25 but comparable to the quantum yield of 0.25 % platinum doped titanium dioxide as shown in Table 3-1.

Apparent quantum yeild (%) = $\frac{(\text{Number of H2 molecules}) \times 2}{\text{Number of indient photons}}$ X100   (3)

Table 3-1: Comparison of various mechanisms for hydrogen production over the catalysts.

Photocatalyst	Yield from HCHO calculated from the pH drop (μmoles/g)	Total Yield (μmoles/g)	Quantum yield (%), full solar spectrum (300-650 nm)
Cu_2O/TiO_2	0.7	1304	1.20
Degussa P25	2.7	130	0.77
TiNW	1.5	28	0.22
Pt/TiO_2 [26]	-	-	1.24

The attempt to close the hydrogen mass balance based on eqns. (1) and (2) shows that the decrease in solution pH is not commensurate with the consumption of formaldehyde, indicating that water splitting may also have contributed to hydrogen production. Hydrogen is expected to be produced by water splitting in the case of copper doped TiO_2, since its conduction band is more negative than TiO_2 vs. saturated calomel electrode (SCE) (higher in position) and its valance band is more positive than TiO_2.[37] This will enable photogenerated electrons to accumulate at the TiO_2 conduction band where water is reduced to produce hydrogen and formaldehyde is oxidized at the hole position as shown in Figure 3-16. HCHO will scavenge any generated holes accumulating at the copper valance band. Unfortunately, due to low consumption of HCHO, we could not confirm this by chemical analysis of HCHO before and after the experiment. However, hydrogen produced by the activation of P25 by solar light is comparable to other values reported in the literature.[38]
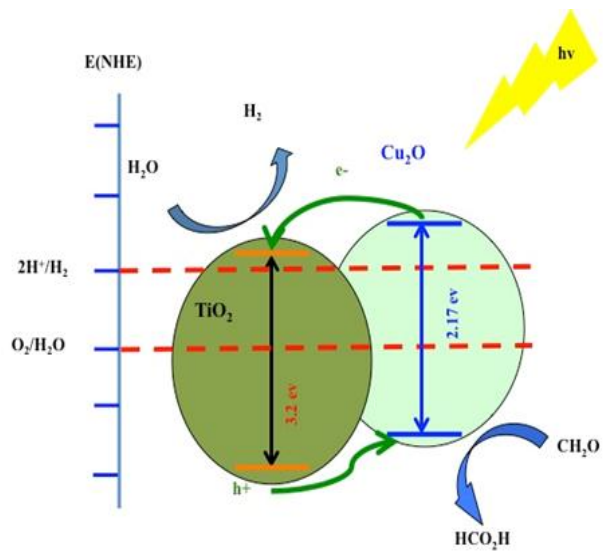
Figure 3-16: Mechanism for solar hydrogen production using Cu_2O-TiO_2 assembly.

3.4 Conclusions

Cu_2O/TiO_2 nanowires of different loading of Cu were prepared using a unique sol-gel methodology in $ScCO_2$. XANES and XPS analyses indicate the presence of only Cu^{+1} oxidation state in the doped catalysts. The Cu_2O/TiO_2 nanowires were found to be active photocatalysts for hydrogen production using a solar simulator (100 mW/cm^2) involving both water splitting and sacrificial hydrogen production mechanisms. Cu_2O/TiO_2 nanowires also indicated higher stability compared to Degussa P25 and undoped TiO_2 nanowires. The maximum hydrogen production of 1304 µmoles of H_2/g-cat for Cu_2O/TiO_2 with 1% Cu was 10 times greater than that of TiO_2 Degussa P25 (130 µmoles of H_2/g-catalyst) and about 47 times more than undoped titanium nanowires. All Cu_2O/TiO_2 nanowires produced a significant amount of hydrogen compared to undoped titanium, which makes copper doped titanium dioxide an excellent photocatalyst for hydrogen production as well as mineralization of organic pollutants such as formaldehyde. These results were attributed to the unique preparation method that enabled highly dispersed dopant and the single active oxidation state of copper as Cu (I). Doping of titanium dioxide with less expensive transition metals such as copper is a promising choice for photocatalytic sacrificial hydrogen generation compared to pristine TiO_2. More importantly, unlike Degussa P25, copper doped TiO_2 nanowires showed no deactivation over 3 cycles of experiments with a total duration of 21 hours. Sacrificial hydrogen production using Cu-TiO_2 and solar radiation serves the dual purposes of water treatment and hydrogen production from waste.

3.5 References

1. Zhu, Z., R. Yang, M. You, X. Zhang, Y. Wu, and W. Tan, *Single-walled carbon nanotube as an effective quencher.* Anal Bioanal Chem, 2010. **396**(1): p. 73-83.

2. Chen, X., S. Shen, L. Guo, and S.S. Mao, *Semiconductor-based photocatalytic hydrogen generation.* Chem Rev, 2010. **110**(11): p. 6503-6570.

3. Lazar, M.A., S. Varghese, and S.S. Nair, *Photocatalytic Water Treatment by Titanium Dioxide: Recent Updates.* Catalysts, 2012. **2**(4): p. 572-601.

4. Chong, M.N., B. Jin, C.W. Chow, and C. Saint, *Recent developments in photocatalytic water treatment technology: a review.* Water Res, 2010. **44**(10): p. 2997-3027.

5. Linsebigler, A.L., G.Q. Lu, and J.T. Yates, *Photocatalysis on Tio2 Surfaces - Principles, Mechanisms, and Selected Results.* Chemical Reviews, 1995. **95**(3): p. 735-758.

6. Anpo, M. and M. Takeuchi, *The design and development of highly reactive titanium oxide photocatalysts operating under visible light irradiation.* Journal of Catalysis, 2003. **216**(1-2): p. 505-516.

7. Mahlambi, M.M., A.K. Mishra, S.B. Mishra, R.W. Krause, B.B. Mamba, and A.M. Raichur, *Metal doped nanosized titania used for the photocatalytic degradation of rhodamine B dye under visible-light.* J Nanosci Nanotechnol, 2013. **13**(7): p. 4934-4942.

8. Kim, S., S.J. Hwang, and W. Choi, *Visible light active platinum-ion-doped TiO_2 photocatalyst.* J Phys Chem B, 2005. **109**(51): p. 24260-24267.

9. Lanese, V., D. Spasiano, R. Marotta, I. Di Somma, L. Lisi, S. Cimino, and R. Andreozzi, *Hydrogen production by photoreforming of formic acid in aqueous copper/TiO_2 suspensions under UV-simulated solar radiation at room temperature.* International Journal of Hydrogen Energy, 2013. **38**(23): p. 9644-9654.

10. Jia, Y.S., S. Shen, D.G. Wang, X. Wang, J.Y. Shi, F.X. Zhang, H.X. Han, and C. Li, *Composite Sr_2TiO_4/$SrTiO_3$(La,Cr) heterojunction based photocatalyst for hydrogen production under visible light irradiation.* Journal of Materials Chemistry A, 2013. **1**(27): p. 7905-7912.

11. Lalitha, K., G. Sadanandam, V.D. Kumari, M. Subrahmanyam, B. Sreedhar, and N.Y. Hebalkar, *Highly Stabilized and Finely Dispersed Cu_2O/TiO_2: A Promising Visible Sensitive Photocatalyst for Continuous Production of Hydrogen from Glycerol:Water Mixtures.* Journal of Physical Chemistry C, 2010. **114**(50): p. 22181-22189.

12. Hara, M., T. Kondo, M. Komoda, S. Ikeda, K. Shinohara, A. Tanaka, J.N. Kondo, and K. Domen, *Cu₂O as a photocatalyst for overall water splitting under visible light irradiation.* Chem Commun (Camb), 1998(3): p. 357-358.

13. Bandara, J., C.P. Udawatta, and C.S. Rajapakse, *Highly stable CuO incorporated TiO(₂) catalyst for photo-catalytic hydrogen production from H(₂)O.* Photochem Photobiol Sci, 2005. **4**(11): p. 857-861.

14. Wu, Y., G. Lu, and S. Li, *The Role of Cu(I) Species for Photocatalytic Hydrogen Generation Over CuO x /TiO₂.* Catalysis Letters, 2009. **133**(1-2): p. 97-105.

15. Foo, W.J., C. Zhang, and G.W. Ho, *Non-noble metal Cu-loaded TiO₂ for enhanced photocatalytic H₂ production.* Nanoscale, 2013. **5**(2): p. 759-764.

16. Gombac, V., L. Sordelli, T. Montini, J.J. Delgado, A. Adamski, G. Adami, M. Cargnello, S. Bernal, and P. Fornasiero, *CuO(x)-TiO₂ photocatalysts for H₂ production from ethanol and glycerol solutions.* J Phys Chem A, 2010. **114**(11): p. 3916-3925.

17. Paracchino, A., V. Laporte, K. Sivula, M. Gratzel, and E. Thimsen, *Highly active oxide photocathode for photoelectrochemical water reduction.* Nat Mater, 2011. **10**(6): p. 456-461.

18. Wu, D.X., Y.J. Wang, C.Y. Zhang, and H.T. Zhu, *3D Flowerlike Copper Sulfide Nanostructures Synthesized from Copper (I) Oxide Hollow Microspheres.* Iumrs International Conference in Asia 2011, 2012. **36**(0): p. 25-33.

19. You, M., T.G. Kim, and Y.-M. Sung, *Synthesis of Cu-Doped TiO₂Nanorods with Various Aspect Ratios and Dopant Concentrations.* Crystal Growth & Design, 2010. **10**(2): p. 983-987.

20. Baxter, J.B. and E.S. Aydil, *Nanowire-based dye-sensitized solar cells.* Applied Physics Letters, 2005. **86**(5): p. 053114.

21. Bogart, T.D., X. Lu, and B.A. Korgel, *Precision synthesis of silicon nanowires with crystalline core and amorphous shell.* Dalton Trans, 2013. **42**(35): p. 12675-12680.

22. Lieber, C.M., *Semiconductor nanowires: A platform for nanoscience and nanotechnology.* MRS Bull, 2011. **36**(12): p. 1052-1063.

23. Farhangi, N., R.R. Chowdhury, Y. Medina-Gonzalez, M.B. Ray, and P.A. Charpentier, *Visible light active Fe doped TiO₂ nanowires grown on graphene using supercritical CO₂.* Applied Catalysis B-Environmental, 2011. **110**: p. 25-32.

24. Garcia-Gonzalez, C.A., M.C. Camino-Rey, M. Alnaief, C. Zetzl, and I. Smirnova, *Supercritical drying of aerogels using CO₂: Effect of extraction time on the end material textural properties.* Journal of Supercritical Fluids, 2012. **66**: p. 297-306.

25. Lucky, R.A., Y. Medina-Gonzalez, and P.A. Charpentier, *Zr doping on one-dimensional titania nanomaterials synthesized in supercritical carbon dioxide.* Langmuir, 2010. **26**(24): p. 19014-19021.

26. Chowdhury, P., G. Malekshoar, M.B. Ray, J. Zhu, and A.K. Ray, *Sacrificial Hydrogen Generation from Formaldehyde with Pt/TiO₂ Photocatalyst in Solar Radiation.* Industrial & Engineering Chemistry Research, 2013. **52**(14): p. 5023-5029.

27. Yu, J. and J. Ran, *Facile preparation and enhanced photocatalytic H2-production activity of Cu(OH)₂ cluster modified TiO₂.* Energy & Environmental Science, 2011. **4**(4): p. 1364.

28. Sui, R., A. Rizkalla, and P.A. Charpentier, *Experimental study on the morphology and porosity of TiO₂ aerogels synthesized in supercritical carbon dioxide.* Microporous and Mesoporous Materials, 2011. **142**(2-3): p. 688-695.

29. Susha, A.S., A.A. Lutich, C. Liu, H. Xu, R. Zhang, Y. Zhong, K.S. Wong, S. Yang, and A.L. Rogach, *Comparative optical study of colloidal anatase titania nanorods and atomically thin wires.* Nanoscale, 2013. **5**(4): p. 1465-1469.

30. Biesinger, M.C., L.W.M. Lau, A.R. Gerson, and R.S.C. Smart, *Resolving surface chemical states in XPS analysis of first row transition metals, oxides and hydroxides: Sc, Ti, V, Cu and Zn.* Applied Surface Science, 2010. **257**(3): p. 887-898.

31. Irie, H., K. Kamiya, T. Shibanuma, S. Miura, D.A. Tryk, T. Yokoyama, and K. Hashimoto, *Visible Light-Sensitive Cu(II)-Grafted TiO₂ Photocatalysts: Activities and X-ray Absorption Fine Structure Analyses.* Journal of Physical Chemistry C, 2009. **113**(24): p. 10761-10766.

32. Hulbert, S.L., B.A. Bunker, F.C. Brown, and P. Pianetta, *Copper ${L}_{2,3}$ near-edge structure in ${\mathrm{Cu}}_{2}$O.* Physical Review B, 1984. **30**(4): p. 2120-2126.

33. Saikova, S., S. Vorobyev, M. Likhatski, A. Romanchenko, S. Erenburg, S. Trubina, and Y. Mikhlin, *X-ray photoelectron, Cu L3MM Auger and X-ray absorption spectroscopic studies of Cu nanoparticles produced in aqueous solutions: The effect of sample preparation techniques.* Applied Surface Science, 2012. **258**(20): p. 8214-8221.

34. Wang, Z., Y. Liu, D.J. Martin, W. Wang, J. Tang, and W. Huang, *CuOx-TiO₂ junction: what is the active component for photocatalytic H2 production?* Phys Chem Chem Phys, 2013. **15**(36): p. 14956-14960.

35. Chen, Z.W., D. Higgins, A.P. Yu, L. Zhang, and J.J. Zhang, *A review on non-precious metal electrocatalysts for PEM fuel cells.* Energy & Environmental Science, 2011. **4**(9): p. 3167-3192.

36. Shimidzu, T., T. Iyoda, and Y. Koide, *An Advanced Visible-Light-Induced Water Reduction with Dye-Sensitized Semiconductor Powder Catalyst.* Journal of the American Chemical Society, 1985. **107**(1): p. 35-41.

37. Tahir, M. and N.S. Amin, *Advances in visible light responsive titanium oxide-based photocatalysts for CO_2 conversion to hydrocarbon fuels.* Energy Conversion and Management, 2013. **76**(0): p. 194-214.

38. Babu, V.J., M.K. Kumar, A.S. Nair, T.L. Kheng, S.I. Allakhverdiev, and S. Ramakrishna, *Visible light photocatalytic water splitting for hydrogen production from $N\text{-}TiO_2$ rice grain shaped electrospun nanostructures.* International Journal of Hydrogen Energy, 2012. **37**(10): p. 8897-8904.

Chapter 4

4 Synthesis and Applications of Indium doped Titanium Nanowires

Indium doped titanium nanowires were prepared using a unique sol-gel methodology in supercritical CO_2 using titanium isopropoxide, indium acetate dopant, and acetic acid with a ratio 1:6 as the polycondensation agent. The methodology produced uniformly dispersed dopants integrated into nanowires with diameters of 80-100 nm and aspect ratios from 15-25 as observed by SEM. XPS results confirmed formation of indium titanate nanowires and their levels of indium compared to titanium. Dye Sensitized Solar Cells (DSSCs) were fabricated and tested with the nanowires under solar light irradiation (100 mW/cm^2) using different levels of indium. Indium doping level of 1.0 atomic % with respect to Ti showed the highest performance photoelectric current compared to pristine titanium nanowires confirming the added advantage of indium in these nanowires by enhancing visible light harvesting and reducing electron-hole recombination. At optimum indium doping, the fabricated DSSC cells showed about 2.5 times higher efficiency and photocurrent compared to undoped titanium nanowires. Hydrogen production showed a greater improvement with 26, and 5.7 times of hydrogen produced compared to undoped titanium nanowires and P25 respectively.

4.1 Introduction

Harvesting electrical, thermal, or chemical energy from sunlight as a source of clean, sustainable and cheap energy is gaining increased attention, especially with increased demands for energy and global efforts to reduce greenhouse gases. The demand for energy is expected to increase by about 37 % by 2035 as the population grows while phasing out of coal power generation plants becomes mandated.[1] In the field of sunlight conversion to electricity, photocatalytic reaction, photoelectrochemical production of fuels, titanium dioxide (TiO_2) has been a base material due to its numerous beneficial properties including chemical and thermal stability, abundance, and cost effectiveness.[2]

However, further development and research is needed to enhance visible light response of TiO_2 to harvest more sunlight to energy. Pristine TiO_2 is only active in a very limited region of the solar spectrum utilizing 5 % of sunlight. Furthermore, more focused work is needed to reduce the high recombination of photogenerated electrons with holes or other chemicals within the application device which negatively impacts its photocatalytic efficiency. [3] [4] An approach that is commonly used to overcome these limitations is doping with transition metals such as Ni, Zr, Cu, Cr, V, Zn, Bi, Fe, and noble metals such as Au, Pt, and Pd. In addition, non-metal dopants such as nitrogen, fluoride, sulfur, and carbon have been examined with varied amounts of success for increased visible light absorption, reduced electron-hole recombination, resulting in a stronger photocatalytic activity of TiO_2. [5-16]

Indium oxide thin films are used in solar cell applications due to two important advantages including high electron mobility while being transparent when used as a conductive layer. [17, 18] These advantages are enhanced by doping with hydrogen as TCO or doping with Zn, molybdenum and yttria-zirconia.[19-23] Comparing thin films and nanoparticles or bulk materials in solar cells or photocatalytic applications, nanowires have more advantages of light scattering properties that increase light absorption within the device and increased continuous direct percolation pathways for electrons to be collected.

This work was driven by the hypothesis of combining the advantages of nanowires and indium oxide to prepare indium doped titanium dioxide for photocatalytic applications. High aspect ratio and well defined nanowires are challenging to prepare and very few preparation methods have been reported. Sol-gel in supercritical carbon dioxide ($ScCO_2$) which has been shown to provide high aspect ratio nanofibers/wires of titania with high surface area and porosity were selected to prepare indium doped titanium nanowires.[24] $ScCO_2$ is an inexpensive and green alternative to conventional organic solvents; it is environmentally benign and non-flammable with low viscosity, zero surface tension and high diffusivity, which are favorable for synthesizing fine and uniform nanomaterials with porous nanostructure.[25] It has also been reported that indium doping enhanced the

71

photocatalytic performance of titania in water treatment and water splitting although In-TiO_2 nanowires have not been reported earlier. [26] [27]

Therefore, this work focuses on the synthesis of indium titanate nanowires at different indium to titanium ratios using a $ScCO_2$ sol-gel process and evaluating their photoelectric performance in DSSC and photocatalytic activity towards hydrogen production using sacrificial agent.

4.2   Experimental Details

4.2.1   Chemicals and Materials

Indium (III) acetate (99.99%), titanium (IV) isopropoxide (TIP) (97%), acetic acid (99.7%), ethylcellulose, and terpineol were purchased from the Aldrich Chemical Company, Oakville, ON, Canada and used without further purification. Instrument grade liquid carbon dioxide (99.99%) from Air Liquide Canada was delivered by a syringe pump (Isco 260D) into a 10 mL view cell reactor equipped with a pressure transducer, heating tape, and thermocouple for temperature control. The details of the reactor are provided in Lucky et al.[28]

4.2.2   Synthesis of Indium Titanate Nanowires

In a typical experiment, predetermined amounts of titanium isopropoxide (TIP) and indium (III) acetate were quickly placed in the 10 ml view cell, followed by the addition of acetic acid, and CO_2. The amounts of indium (III) acetate were varied to prepare four different concentrations of indium titanate referred to in this paper as In1, In2, In3, and In4. The view cell was heated to 60 °C and subsequently pressurized to 5000 psig. A magnetic stirrer was used to ensure uniform mixing of the reactants. The hydrolysis rate was controlled by adjusting metal precursors to acetic acid molar ratios in the range of 1:5-6. During the gelation stage, a light pink color was observed in about 30 and 40 minutes for indium doped titania before changing to white color the next day. After five days of aging, the samples were washed with 100 mL of $scCO_2$ at a rate of 0.3 mL/min to remove unreacted materials and by-products, and to prevent collapse of the gel network. The prepared indium doped TiO_2 sol-gel was then calcined in air at 500 °C for 2 hours.

The calcination temperature was selected based on the thermal gravimetric analysis (TGA) results (not shown) where indium doped catalysts showed removal of organic components at about 450 °C. Similarly undoped titanium dioxide nanowires were prepared without the addition of indium (III) acetate.

4.2.3   Preparation of Photoanode

Indium titanate nanowires were prepared into a paste for coating on conductive glass. The paste was made by dissolving ethylcellulose into ethanol and terpineol mixture (2:1, v/v) and stored in a sealed container to minimize the changes in viscosity due to solvent evaporation. Fluorine doped tin oxide (FTO) glass plates (15 ohms per sq. inch, purchased from Solaronix, Switzerland) were cleaned by detergent wash and sonication for 10 minutes for three times, rinsed with DI water, sonicated in acetone for 5 minutes, washed with isopropanol, and finally dried with nitrogen gas.

Photoanodes were prepared by creating a mask template using packing tape with about 40 µm thickness on the conductive side of the FTO glass. Indium titanate nanowires-paste mixture was applied by doctor-blading with a glass rod, which formulates the active layer of the photoanode. The template tape was lifted after 30 minutes to minimize cracking of the paste. For comparison, the same procedure was done for TiO_2 (P25) and undoped titanium nanowires. The coated FTO glass then was calcined to 500 °C under air at a heating rate of 5 °C /min. The resulting films were cooled to 80 °C before immersing for overnight into a dye solution of 0.3 mM cis-diisothiocyanato-bis (2,2'-bipyridyl-4,4'-dicarboxylato) ruthenium (II) bis (tetrabutylammonium), also called N719 dye (purchased from Solaronix, Switzerland) in acetonitrile tert-butyl alcohol (1:1, v/v) solution.

4.2.4   Assembling dye sensitized solar cells (DSSCs)

The solar cell was assembled by combining platinum coated glass as a counter electrode with the photoanode prepared in the previous step. Platinum electrode was washed with a detergent and rinsed with DI water, followed by acetone before regeneration at 350 $^{\circ}$C for 30 minutes prior to use. The two electrodes were kept at a distance using 50 µm thick

Surlyn hot-melt gaskets. The cells then were laminated together by pressing them on a hot plate at 100 ºC. Iodine / tri-iodide based Iodolyte Z-100 from Solaronix was used as redox electrolyte, which was injected into the cell void by vacuum filling technique through a predrilled hole at the back of the counter electrode. Finally the cell was sealed with hot-melt sheet and a glass slide cover.

4.2.5   Photocatalytic Hydrogen Production

The experimental setup for photocatalytic sacrificial hydrogen production was reported previously. [29] A pyrex glass photocatalytic reactor (11 cm x 6.3 cm) with a volume of 350 ml was used to carry out the experiments. Most of the experiments were conducted using 50 mg of photocatalyst in 50 ml solution using 0.16 M formaldehyde as the sacrificial agent. Prior to solar irradiation, the solution was agitated at 500 rpm using a magnetic stirrer (Heidolph) for 1 hour with simultaneous nitrogen purging at ambient pressure to eliminate oxygen from the solution. The reactor contents were irradiated using a solar simulator (model: SS1 KW, Sciencetech) with a xenon arc lamp, and was continuously stirred at 500 rpm. The solar lamp produces irradiance at full power (1000 watts), which is similar to the global solar spectrum of 100 mWcm^{-2}. The photocatalytic reactor was air-cooled with an electric fan to keep the temperature constant at ambient conditions. A Gas Chromatography (Schimadzu GC 2014, Heyesep D packed column: 10 m length, 2 mm ID, and 2 µm film thickness, with thermal conductivity detector (TCD)) was utilized for quantification of producing hydrogen. The calibration of the GC was conducted using a 1000 ml gas-sampling bulb (Supelco), which was filled with nitrogen and hydrogen to yield hydrogen calibration gas with desired concentrations.

4.2.6   Characterization of Indium Titanate Nanowires

The synthesized nanowire morphology was characterized by scanning electron microscopy (SEM) (Model LEO 1530) and transmission electron microscopy (TEM) (Model JEOL 2010F) capable of dark field scanning transmission electron microscopy (STEM) and coupled with energy dispersive X-ray spectroscopy. For TEM analysis, the powdered samples were dispersed in ethanol by sonication for 15 min and then cast on a copper grid covered with holey carbon film. Samples for SEM imaging were prepared by

applying the powder directly to a carbon adhesive tape. The BET (Brunauer-Emmett-Teller) surface area and BJH (Barrett-Joyner-Halenda) pore size and volume analysis were determined from nitrogen adsorption and desorption isotherm data obtained at 77 K with a constant-volume adsorption apparatus (Micromeritic Tristar II) using N_2 gas (99.995% pure; obtained from Praxair, Canada). The prepared samples were degassed at 150°C overnight before measurements. Structural analysis of the samples was performed using an X-ray powder diffractometer (Rigaku Miniflex XRD, Texas, U.S.A.), fitted with a rotating sample holder, a scintillation counter detector and a divergent beam utilizing a Cu K source of X-rays (= 1.5418 °A). The XPS analysis was carried out with a Kratos Axis Ultra spectrometer using a monochromatic Al K (alpha) source (15mA, 14kV). Photocurrent performance of DSSCs was tested under Oriel solar simulator (92250A, AM 1.5 G) equipped with a 150 W Xe lamp and intensity of 100 mW/cm^2 measured by a Keithley 2420 programmable SourceMeter.

4.3 Results and Discussion

Indium titanate nanowires were successfully prepared by the $scCO_2$ sol-gel process at different loadings (0.05 g, 0.10 g, 0.22 g, and 0.38 g) of indium (III) acetate with 3.3 g titanium isopropoxide (TIP), 3.5 ml acetic acid and pressurized with $scCO_2$ at 60 ºC and 5000 psi. TiO_2 nanowires were prepared using the same methodology without the addition of indium acetate. The selectivity of producing indium titanate nanowires or TiO_2 nanowires over nanoparticles is dictated by the alkoxide to acetic acid ratio. Nanowires can be produced with alkoxide to acetic acid ratio 4.5 as shown previously.[30] The nanowires morphology was examined by TEM and its image is shown in Figure 4-1 for the prepared nanowires. Figure 4-1b shows a higher magnification of indium doped nanowires and at even higher magnification, a single indium titanate nanowire is shown in Figure 4-1c. A dark field image shown in Figure 4-1d demonstrates clear uniformity, aspect ratio and porosity of these nanowires.
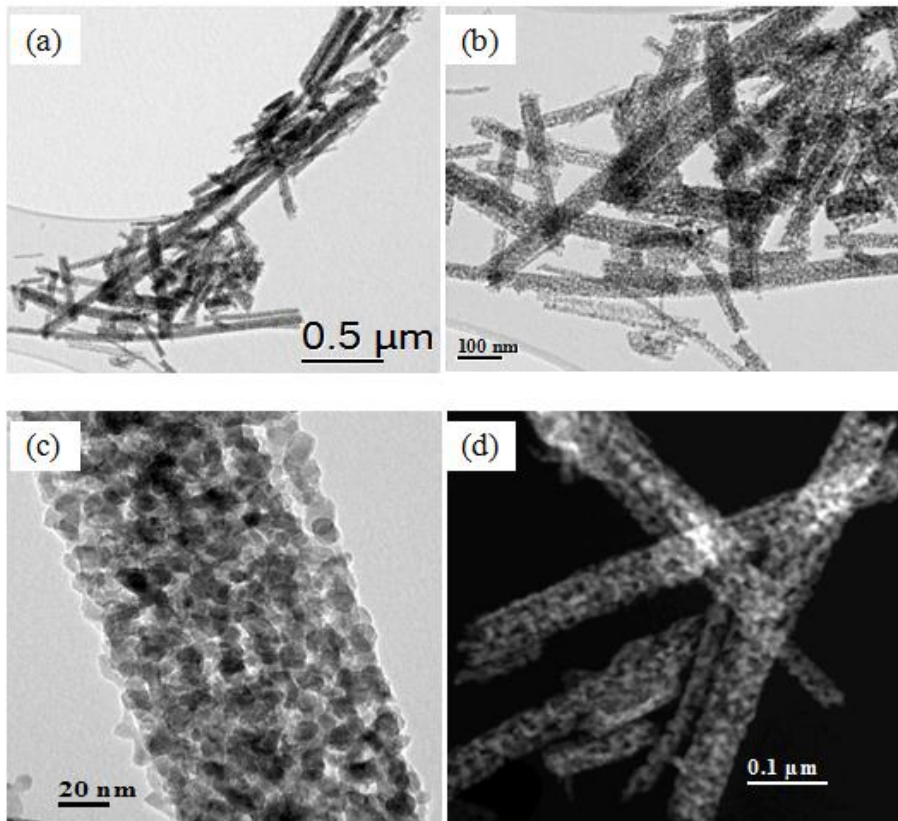
Figure 4-1: TEM images of TiO_2 nanowires [3.3 g TIP and 3.5 ml acetic acid](a), higher magnification of (a), and TEM images of single indium titanate nanowire [0.37g indium acetate, 3.5 ml acetic acid] (c), HAADF image showing porosity of nanowires (d). Synthesis was in $scCO_2$ at 60 ℃ and 5000 psi.

Dopant dispersion is a critical parameter for photocatalytic and photoanode in DSSC. To illustrate the degree of dopant metal dispersion throughout the nanowires, TEM mapping using energy dispersive X-ray spectroscopy (EDS) is shown for indium titanate nanowires in Figure 4-2. The nanowires showed uniform dispersion of indium metal throughout the nanowires with indium loadings at 1, 2, and 2.5 atomic % that was confirmed by EDS analysis. This result shows the high dispersion of indium throughout the indium titanate nanowires, attributed to the unique synthesis methodology using $scCO_2$ as a solvent and drying agent. $ScCO_2$ enhanced the precursors' solubility, preventing the collapse of the formed networks during gelation due to the zero surface tension of $scCO_2$ during the aging and washing stages.
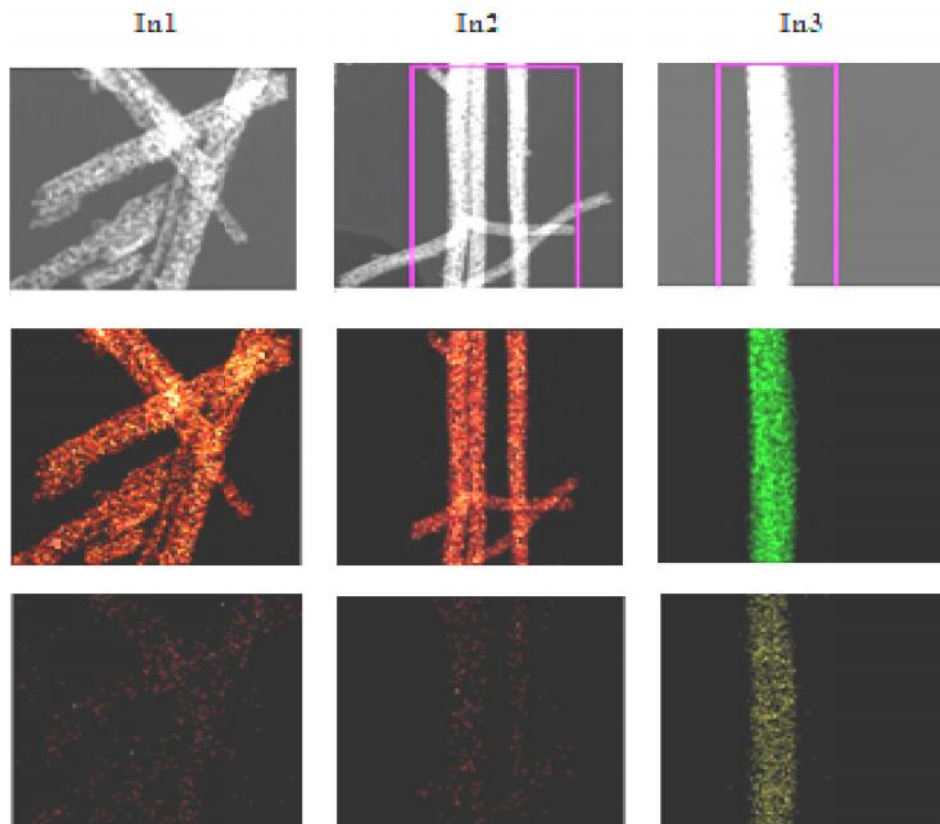
Figure 4-2: EDS mapping of Indium doped TiO$_2$ nanowires showing the dispersion of titanium, and indium within a nanowires. Images from top to down are; high angle annular dark field STEM, Titanium (Ka1), In (La1) signals respectively.

Enhanced dispersion of the indium dopant has been an important factor in producing high surface areas indium titanate nanowires. It is well known that a materials surface area decreases as its dimensionality decreases. For example, nanoparticles have a higher surface area compared to nanorods and nanowires.[31, 32] Despite the formation of nanowires, the produced undoped TiO$_2$ nanowires had comparable surface areas to Degussa P25 (also examined in this work) which we measured at 58 and 50 m^2/g, respectively. The BET results of all four samples In1, In2, In3, and In4 nanowires were measured as 113, 109, 100.6 and 112.8 m^2/g, respectively. This significant increase in surface area can be attributed to the pores forming during the sol-gel synthesis and retaining of the pores by the scCO$_2$ drying as shown summarized Table 4-1.

Table 4-1: BET results for P25 TiO$_2$, undoped TiO$_2$ nanowires, and indium titanate nanowires In1, In2 , In3 and In4.

Sample	BET (m2/g)	Micropore area (m^2/g)	Ext. surface area (m^2/g)	Micropore volume (m^3/g)	Pore size (nm)
P25	58	-	-	-	-
TiNW	50	-	-	-	-
In 1 (1 %)	113.0	51.7	61.7	0.0114	10.0
In 2 (2 %)	109.0	43.3	65.7	0.00518	9.8
In 3 (3 %)	100.6	40.9	59.7	0.00546	6.8
In 4 (4 %)	112.8	39.4	73.4	0.001312	4.6

Indium titanate nanowires XRD spectra are shown in Figure 4-3. Examination of the indium doped samples shows clearly the anatase TiO$_2$ phase with characteristic peaks at 25^0, 38^0, 48^0, 55^0, 63^0, 70^0 and 76^0. These are in excellent match to anatase (PDF 01-086-1157). No peaks at 30.66^0, 35.540, and 51.09^0 that represent In$_2$O$_3$ were detected at low indium doping in samples In1, In2, and In3. However, In4 with 4% indium loading showed broad of peaks at $2 = 31^0$ and 35^0 which could be attributed to indium oxide. In addition, doping with indium produced a rutile phase titania at a lower than expected temperature, which has been recently reported.[33] Due to the lack of sensitivity of XRD at this level of indium doping, more conclusive analysis using X-ray Absorption Near Edge Spectroscopy (XANES) and XPS were performed.
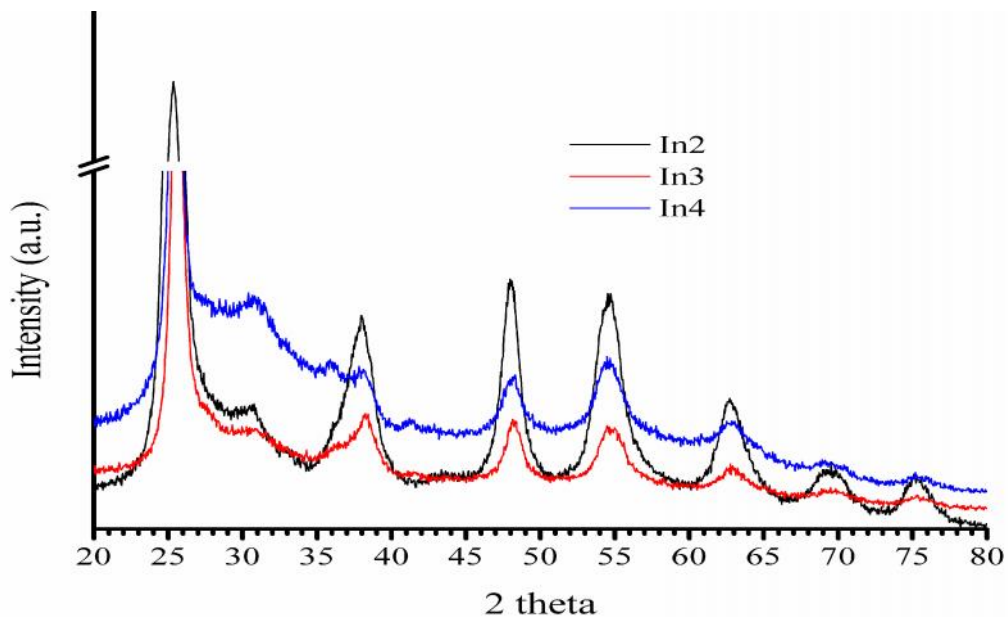
Figure 4-3: XRD results of titanium dioxide nanowires, indium titanate nanowires (a) XRD overview (b, c, and d) selected ranges magnification.

Both the chemical oxidation states of indium and titanium and their concentrations were determined by XPS analysis. In all the indium titanate nanowires, the chemical state of titanium was found to be (IV) with a binding energy peak of 2p 3/2 at 458.63 eV, depending on its interaction with the dopant metal as shown in Figure 4-4. The XPS analysis showed a characteristic binding energy peak of In 3d 5/2 at 444.66 eV eV, which indicates the existence of In (III). This confirms successful indium doping into the nanowires (Figure 4-4).
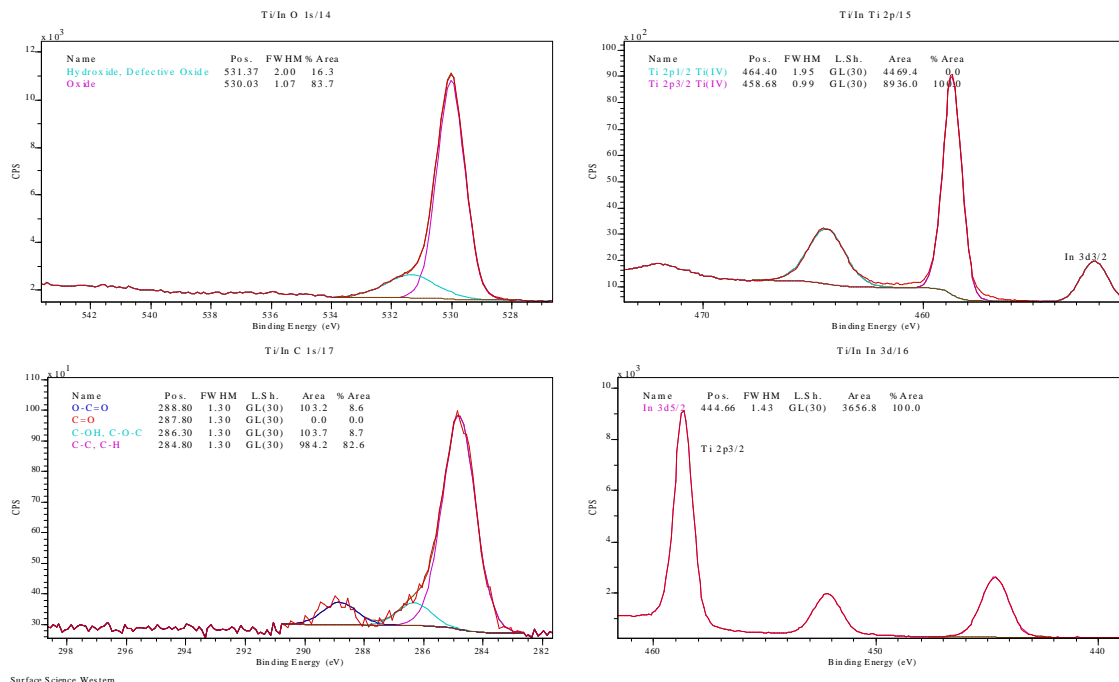
Figure 4-4: XPS of indium titanate nanowires showing indium, oxygen, carbon and titanium binding energies and oxidation states.

4.3.1　XANES and EXAFS

The normalized Ti $L_{3,2}$-edge XANES of the indium doped TiO_2 nanowires in comparison with anatase and rutile TiO_2 (> 99.7 %, Sigma-Aldrich), is shown in Figure 4-5a. XANES spectroscopy probes the transitions from Ti $2p_{3/2}$ and $2p_{1/2}$ states to unoccupied $3d_{5/2}$ and $2p_{3/2}$ states. For anatase and rutile TiO_2, the features in the XANES spectra are due to the splitting pattern (t_{2g} and e_g) of the energy of the d orbitals under an octahedral crystal field followed by local distortion that leads to different local symmetries for anatase (D_{2d}) and rutile (D_{2h}). It can be seen that the most striking difference is the intensity ratio between feature e_{11} and e_{12}, that is, feature e_{11} is dominant in anatase while feature e_{12} is dominant in rutile. The lowering of the O_h symmetry to D_{2d} and D_{2h} leads to the $2p$ e_g transition further splitting into peak e_{11} and e_{12} at the L_3-edge. The symmetry variations between anatase and rutile have an impact on the e_g state; therefore, we can track anatase and rutile phases via the relative ratio between features e_{11} and e_{12}. [34]

The XANES spectroscopy of the In doped TiO_2 nanowires, the e_{11} and e_{12} features are observed with similar intensity, indicating that the sample has both anatase and rutile phases. Since the edge jump of the XANES spectrum is proportional to the quantities of the sample, the compositional fractions of the composite sample can be obtained by fitting a linear combination of the spectra of its components to that of the composite. Figure 4-5b shows the linear fitting results of the In doped TiO_2 nanowires. The best fitting curve (red dotted curve) gives the same ratio of e_{11} and e_{12} as the experimental one (black solid curve), illustrating that the weight ratio between anatase and rutile in the In doped TiO_2 nanowires is about 2:3. The difference between the fitting and experimental curves (blue dash-dotted curve) is due to the broadening of the experimental spectrum (poor crystallinity and porous structure of the In doped TiO_2 nanowires). Ti $L_{3,2}$-edge XANES results of In doped TiO_2 nanowires agree well with their XRD results.
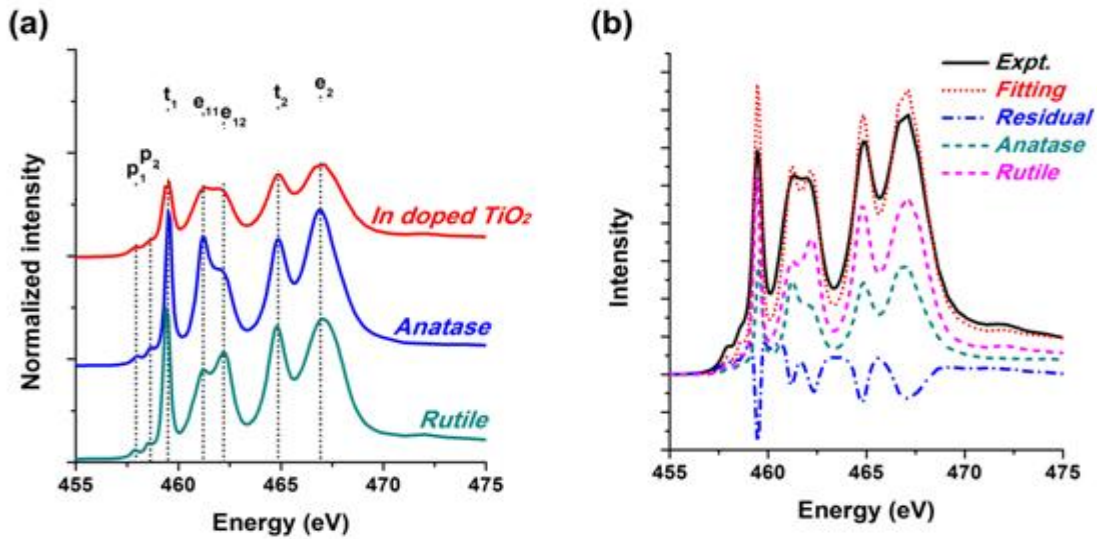
Figure 4-5: (a) TEY XANES spectra of In doped TiO_2 nanowires at Ti L3,2-edge. The spectra of standard TiO_2 of anatase and rutile phase are also shown for comparison. (b) Linear combination fitting analysis of the In doped TiO_2 nanowires at Ti L3,2-edge.

4.3.2 Photocurrent measurements

Photocurrent density-voltage (J-V) curves for P25 TiO_2, undoped TiO_2 nanowires, and indium titanate nanowires In1, In2, In3 and In4 are shown in Figure 4-6. This data was collected using $100mW/cm^2$ solar simulator light and all DSSCs were prepared under the same conditions as described earlier. The open-circuit voltages (Voc) for P25 and sample

TiO$_2$ NW are 0.70 and 0.63 V, respectively. However, all indium doped nanowires showed lower Voc values of 0.601, 0.578,572, and 527 V for In1, In2, In3 and In4, respectively. These results show an inverse relation between indium concentration and Voc. The photoelectric performance of a dye sensitized cell can be evaluated by determining the cell efficiency ( ) calculated using equation 4-1.

$$=Jsc*Voc \; X \; FF \; / \; I \qquad \qquad \textbf{4-1}$$

It is clear from these results that indium doping increased the efficiency of all DSSCs except for In4. In1 showed about 2.5 times higher efficiency and 2.4 times the photocurrent density of TiO$_2$ NW in the DSSC measurements. Furthermore, it was noticed that indium doping reduced series resistance of In1 to 455   compared to TiO$_2$ NW with series resistance of 724   . However, Rs increased for the rest of the samples as indium concentration increases. These results indicate that indium addition improved the photoanode performance of the DSSC's with an optimum loading at 1 %.
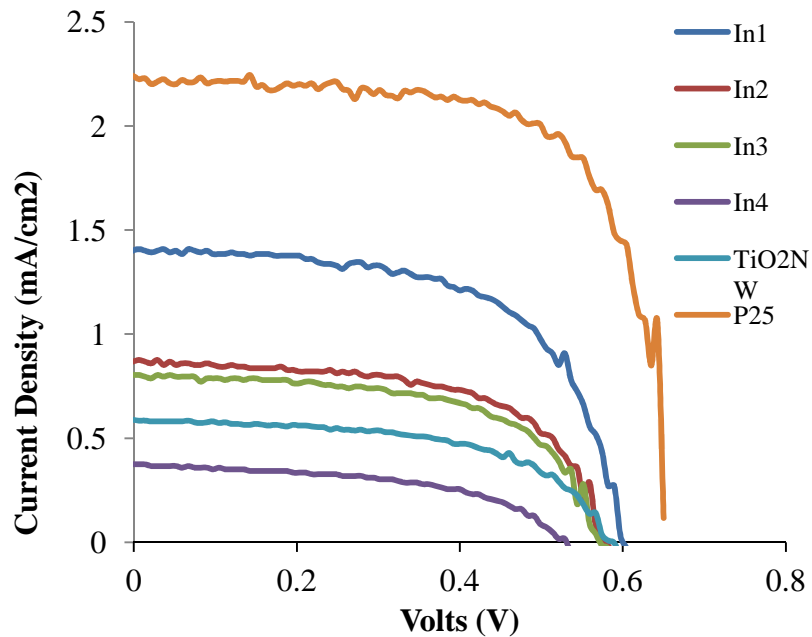
Figure 4-6: Photocurrent density- voltage (J-V) curves for P25 TiO$_2$, undoped TiO$_2$ nanowires, and indium titanate nanowires In1, In2 , In3 and In4.

Although Voc is an indication of the chemical potential of the cell, which is a function of nanocrystalline material in the photoanode with respect to chemical potential of the redox electrolyte, the voltage at zero short circuit current (P_{max}) is used to evaluate the dye sensitized solar cell's overall electrical power generation. The P_{max} for all indium titanate nanowire DSSCs was significantly higher than TiO_2 NW's as shown in Figure 4-7. These results can be attributed to their higher photocurrent generation compared to TiO_2 NW as shown in Table 4-2.
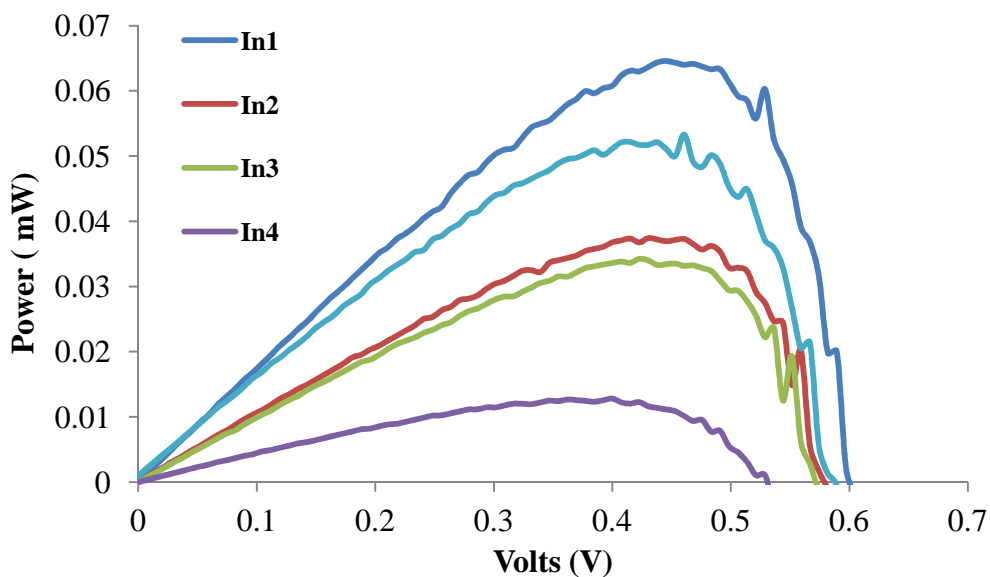
Figure 4-7: Power (mW) curves for undoped TiO_2 nanowires, and indium titanate nanowires In1, In2 , In3 and In4.

Table 4-2: Photoelectric performance parameters for P25 TiO$_2$, undoped TiO$_2$ nanowires, and indium titanate nanowires In1, In2 , In3 and In4.

Sample	Voc (V)	Jsc(mA/cm^2)	P$_{max}$(mW)	Fill Factor (%)	(%)	Rs ( )	Rsh ( )
P25	0.70	2.23	0.57	70	1.09	50	20473
TiNW	0.63	0.59	0.50	57	0.21	724	27411
In 1 (1 %)	0.601	1.413	0.065	60.5	0.51	455	34869
In 2 (2 %)	0.578	0.868	0.037	59.1	0.30	770	41376
In 3 (3 %)	0.572	0.805	0.034	58.5	0.27	890	49173
In 4 (4 %)	0.527	0.374	0.013	50.6	0.10	2291	42748

4.3.3   Electrochemical Impedance Spectroscopy Analysis

Internal evaluation of DSSCs is critical as it deepens our understanding of the competing processes that occur within the novel nanowire photoanode materials produced in this work. Kinetics of the photoelectrochemical processes is critical for determining the limitations and evaluating proposed enhancement approaches. [35] A well established method that can provide detailed knowledge of these competing reactions is electrochemical impedance spectroscopy (EIS).[36] Charge transfer resistance is a limiting factor for DSSCs. Two interfaces in DSSCs where charge transer can take place are: i) at the Pt/electrolyte interface and ii) at the indium titanate (nanocrystalline material)/dye/ electrolyte interface, referred to as R$_{Pt}$ and R$_{ct}$, respectively. EIS spectra of indium titanate nanowires are shown in Figure 4-8, which were collected using 200 mV AC, -0.5 DC V, and signal frequency 0.1 to 1 x 10^5 Hz, while the cell was under 1 sun illumination at 100 mW/cm^2. Two semicircles were observed in all the DSSCs. The first was at a high frequency region with corresponding information about the Pt/electrolyte interface resistance R$_{Pt}$. The second circle was at the middle frequency region,

corresponding to indium titanate nanowires/dye/electrolyte interface resistance R_{ct} which was insignificant. However, no semicircle at low frequency was observed which indicates that electron diffusion limitation occurs within the electrolyte. [37]

Fitting the electrochemical impedance spectra to equivalent circuit will enable determination of each internal resistance of the DSSC. The equivalent electrical model consists of resistors that are connected in series with parallel capacitors to reflect chemical capacitance at different interfaces as shown in Figure 4-8c. In this model R1, R2 and R3 represent series resistance, resistance at counter electrode, and resistance at the photoanode respectively. CPE1 and CPE2 represent chemical capacitance at counter electrode/electrolyte and photoanode (nanocrystalline /dye/electrolyte), respectively. The resistance and chemical capacitance results were calculated from the spectra using Z-view software.

The drop in DSSCs efficiency with increasing indium doping concentration can be explained by the EIS spectra results. The increase in charge transfer resistance at the counter electrode of DSSCs with In2, In3, and In4 was observed in the EIS spectra as maximum of the semicircles is in higher frequency, compared to In1 which shifted to the right as a lower frequency as shown Figure 4-8b. These EIS results are in a good agreement with the decreasing efficiency and increased resistance values Rs at open circuit conditions of the corresponding DSSCs obtained from J-V measurement. The increased efficiency of In1 DSSC compared to undoped TiO_2 nanowires DSSC prepared using the same synthesis method is attributed to the reduced recombination rate and enhanced light harvesting efficiency, and lower Rs resistance value of 455 for In1 compared to 724 for TiO_2 NW. However, as the indium doping concentration increased, the resistance of at the counter electrode increased. The series resistance, R_{Pt} and R_{ct}, are referred to in our fitted model as R1, R2, and R3, respectively. The disappearance of the semicircles at middle and low frequencies is attributed to the fact that R_{ct} is not significant but as its values (R3) are lower than the rest of resistance as shown in Table 4-3.
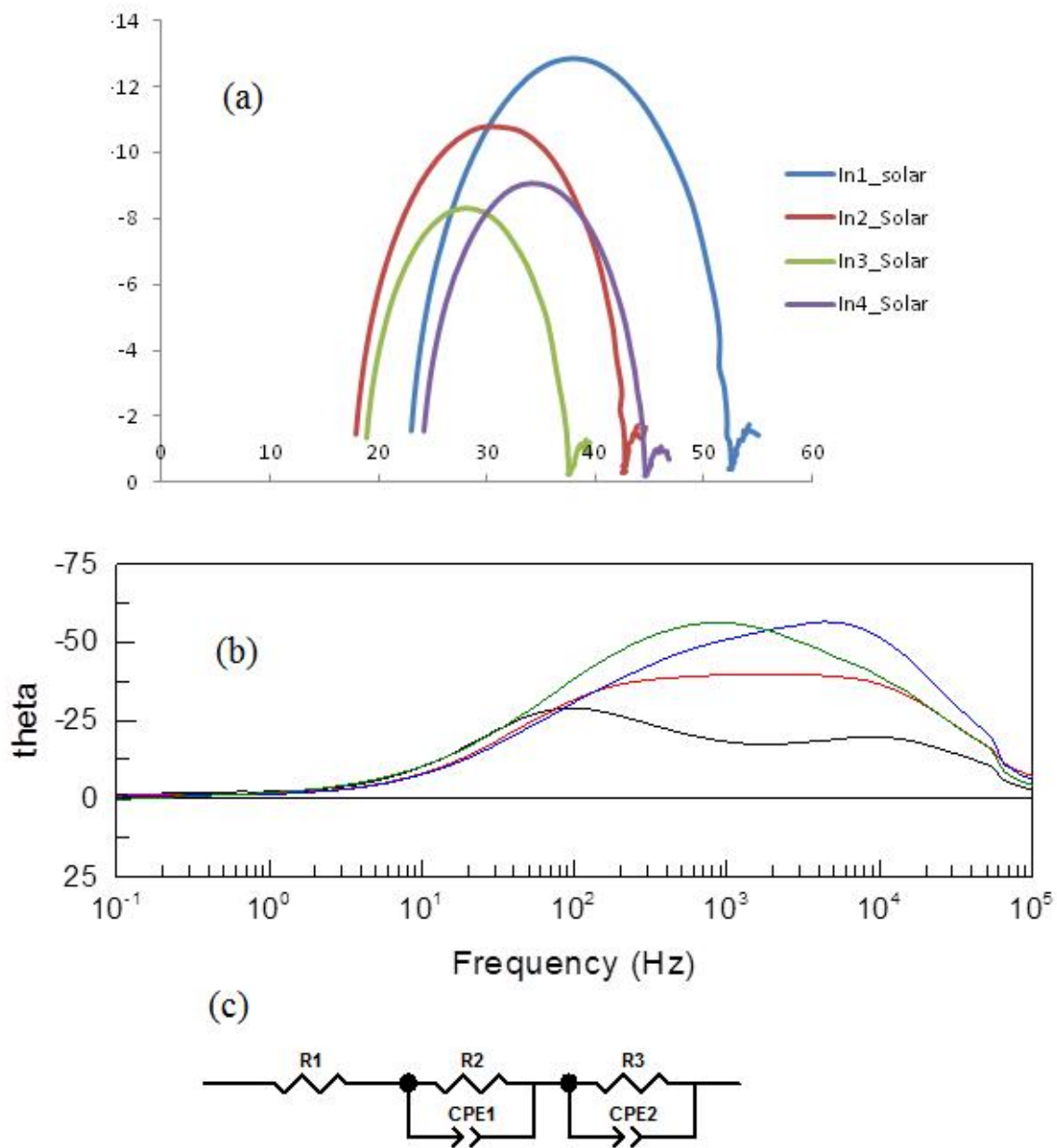
Figure 4-8: Nyquist plot (a) and the bode plots (b) measured with EIS analyzer for the DSSCs of Indium Titanate nanowires and (c) equivalent circuit.

Table 4-3: Typical EIS parameters calculated by fitting the data to an equivalent circuit for P25 TiO$_2$, undoped TiO$_2$ nanowires, and indium titanate nanowires In1, In2 , In3 and In4.

Sample	R1	R2	R3	Efficiency (%)	Rs ( )	Rsh ( )
P25	4.67	15.16	120	1.09	50	20473
TiO$_2$ NW	4.15	7.98	202	0.21	724	27411
In 1 (1 %)	4.18	22.77	28.09	0.51	455	34869
In 2 (2 %)	4.45	17.62	22.61	0.30	770	41376
In 3 (3 %)	4.23	18.35	17.84	0.27	890	49173
In 4 (4 %)	2.5	17.82	19.69	0.10	2291	42748

4.3.4   Photocatalytic Hydrogen Production

Photocatalytic activities of synthesized indium titanate nanowires, undoped TiO$_2$ nanowires, and P25 were investigated for sacrificial hydrogen production, with the results shown in Figure 4-9. Higher hydrogen amounts were produced by indium titanate irrespective of the indium loading level, indicating that indium titanate has a higher photocatalytic activity than pure P25 or undoped TiO$_2$ nanowires. The results showed indium doping with 2 atomic % produced highest amount of hydrogen of 734 µmol/g-hr followed by 1 atomic %, 3 atomic % and 4 atomic% with hydrogen production of 637, 351, and 88 µmol/g-hr, respectively. These are significant improvements compared to the undoped TiO$_2$ nanowires, which produced only 28 µmol/g-hr and 130 µmol/g-hr of P25. The results showed no decline of the catalytic activities for all catalysts over seven hours during the experiment. Optimum indium loading was found to be about 2 atomic %, which produced a significant amount of hydrogen, around 5.7 times more than that of

commercial P25, and 26 more than undoped TiO_2 nanowires. Using supercritical CO_2 as solvent, uniform nanowires with high surface area comparable to the nanoparticles were prepared that provided the required higher sites for reaction to take place with better surface charge transport and separation. In addition, doping with indium produced mixed phase of anatase and rutile as discussed in the XANES section which provided more active boundaries in addition of indium boundaries for reaction to take place and effective charge transport resulting in reduced recombination and enhancing hydrogen generation.
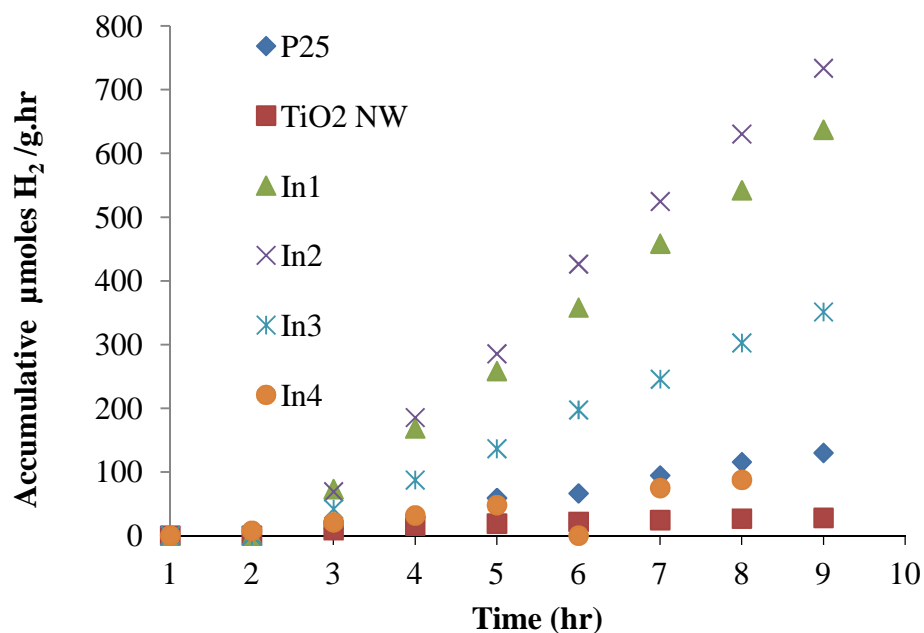
Figure 4-9: Hydrogen production using 0.16M formaldehyde, catalyst loading of 1g/L under solar radiation of 100mW/cm^2.
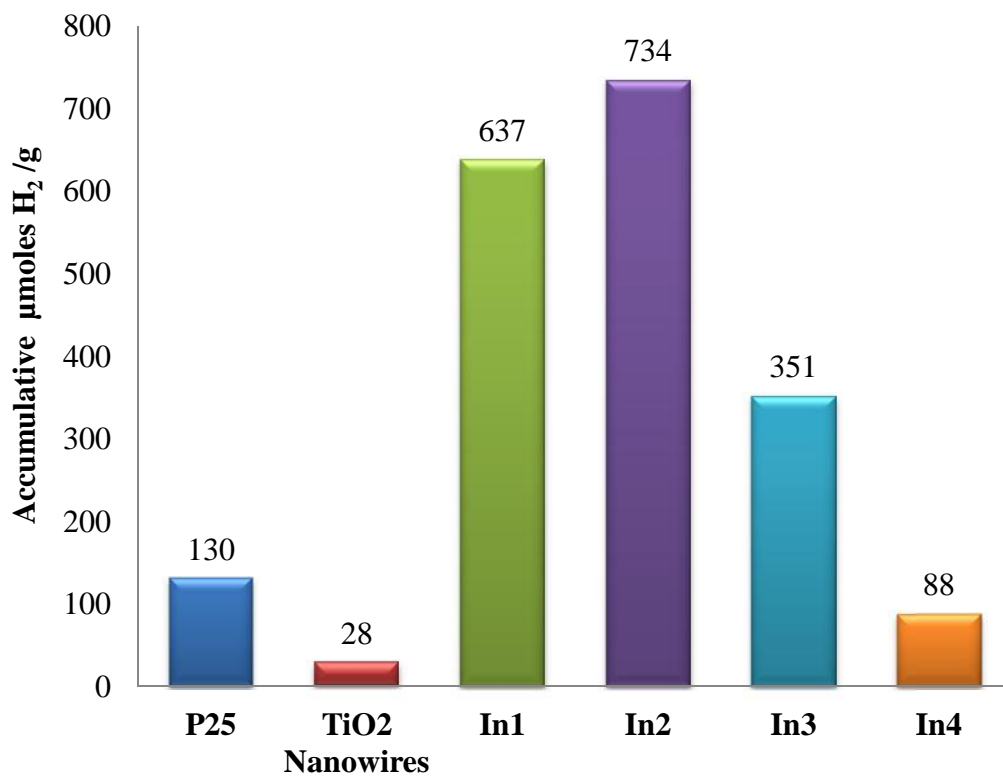
Figure 4-10: Total hydrogen produced by indium doped nanowires (In1, In2,In3, and In4), undoped TiO_2 nanowires, and undoped P25.

4.4   Conclusion

Indium titanate nanowires at different levels (1-4 atomic %) of indium were prepared and characterized using SEM, TEM and EDS showing uniform indium dispersion within formed nanowires. In addition, this method produced the high surface areas which were double the commercially available nanoparticles P25 and prepared undoped nanowires. Photoelectric current generated by 1.0 atomic % indium was double that produced by undoped TiO_2 nanowires and its efficiency was 2.5 times. However, for as a photocatalyst for hydrogen production, indium titanate nanowires showed a greater improvement with 26, and 5.7 times of hydrogen produced compared to undoped titanium nanowires and P25 respectively. These results make indium titanate an excellent photocatalyst for sacrificial hydrogen production.

4.5 References

1. BP, *BP Energy Outlook 2035*. 2015.

2. Chong, M.N., B. Jin, C.W. Chow, and C. Saint, *Recent developments in photocatalytic water treatment technology: a review.* Water Res, 2010. **44**(10): p. 2997-3027.

3. Linsebigler, A.L., G.Q. Lu, and J.T. Yates, *Photocatalysis on Tio2 Surfaces - Principles, Mechanisms, and Selected Results.* Chemical Reviews, 1995. **95**(3): p. 735-758.

4. Anpo, M. and M. Takeuchi, *The design and development of highly reactive titanium oxide photocatalysts operating under visible light irradiation.* Journal of Catalysis, 2003. **216**(1-2): p. 505-516.

5. Mahlambi, M.M., A.K. Mishra, S.B. Mishra, R.W. Krause, B.B. Mamba, and A.M. Raichur, *Metal doped nanosized titania used for the photocatalytic degradation of rhodamine B dye under visible-light.* J Nanosci Nanotechnol, 2013. **13**(7): p. 4934-4942.

6. Jia, Y.S., S. Shen, D.G. Wang, X. Wang, J.Y. Shi, F.X. Zhang, H.X. Han, and C. Li, *Composite Sr2TiO4/SrTiO3(La,Cr) heterojunction based photocatalyst for hydrogen production under visible light irradiation.* Journal of Materials Chemistry A, 2013. **1**(27): p. 7905-7912.

7. Samsudin, E.M., S.B.A. Hamid, J.C. Juan, W.J. Basirun, and G. Centi, *Enhancement of the intrinsic photocatalytic activity of TiO 2 in the degradation of 1, 3, 5-triazine herbicides by doping with N, F.* Chemical Engineering Journal, 2015. **280**: p. 330-343.

8. Abidov, A., B. Allabergenov, F.Y. Xiao, X. Jin, S.W. Jeong, B.H. Park, H.J. Kim, K.H. Jhee, and S.J. Kim. *Fabrication and Characterization of Amine Compounds Synthesized from Carbon Dioxide and Ammonia Water Using Transition Metal Doped TiO2*. in *Applied Mechanics and Materials*. 2015. Trans Tech Publ.

9. Nishiyama, N., Y. Fujiwara, K. Adachi, K. Inumaru, and S. Yamazaki, *Preparation of porous metal-ion-doped titanium dioxide and the photocatalytic degradation of 4-chlorophenol under visible light irradiation.* Applied Catalysis B-Environmental, 2015. **176**: p. 347-353.

10. Momeni, M.M. and Y. Ghayeb, *Photoelectrochemical water splitting on chromium-doped titanium dioxide nanotube photoanodes prepared by single-step anodizing.* Journal of Alloys and Compounds, 2015. **637**: p. 393-400.

11. Reddy, M., N. Sharma, S. Adams, R.P. Rao, V.K. Peterson, and B. Chowdari, *Evaluation of undoped and M-doped TiO₂, where M= Sn, Fe, Ni/Nb, Zr, V, and Mn, for lithium-ion battery applications prepared by the molten-salt method.* RSC Advances, 2015. **5**(37): p. 29535-29544.

12. Mathis, J., J. Lieffers, C. Mitra, F. Reboredo, Z. Bi, C. Bridges, M. Kidder, and M. Paranthaman, *Increased photocatalytic activity of TiO₂ mesoporous microspheres from codoping with transition metals and nitrogen.* Ceramics International, 2016. **42**(2): p. 3556-3562.

13. Barakat, M.A. and R. Kumar, *Photocatalytic Activity Enhancement of Titanium Dioxide Nanoparticles*, in *Photocatalytic Activity Enhancement of Titanium Dioxide Nanoparticles*. 2016, Springer. p. 1-29.

14. Islam, M., N. Zalikha, H. Kosslick, M.T. Zainuddin, Z.A. Zubir, A.A. Nazri, S. Azrolsani, A. Malek, M. Zahid, and M. Ezwan. *Effect of Single and Bimetallic Ni, V and Mn Transition Metal Ion Doping on the Properties of Anatase/Brookite TiO2 Photocatalyst*. in *Advanced Materials Research*. 2016. Trans Tech Publ.

15. Munir, S., S.M. Shah, and H. Hussain, *Effect of carrier concentration on the optical band gap of TiO₂ nanoparticles.* Materials & Design, 2016. **92**: p. 64-72.

16. Bakar, S.A. and C. Ribeiro, *An insight toward the photocatalytic activity of S doped 1-D TiO₂ nanorods prepared via novel route: As promising platform for environmental leap.* Journal of Molecular Catalysis A: Chemical, 2016. **412**: p. 78-92.

17. Van Hest, M., M. Dabney, J. Perkins, D. Ginley, and M. Taylor, *Titanium-doped indium oxide: A high-mobility transparent conductor.* Applied Physics Letters, 2005. **87**(3): p. 2111.

18. Jäger, T., Y.E. Romanyuk, S. Nishiwaki, B. Bissig, F. Pianezzi, P. Fuchs, C. Gretener, M. Döbeli, and A.N. Tiwari, *Hydrogenated indium oxide window layers for high-efficiency Cu (In, Ga) Se₂ solar cells.* Journal of Applied Physics, 2015. **117**(20): p. 205301.

19. Koida, T., H. Fujiwara, and M. Kondo, *Hydrogen-doped In₂O₃ as high-mobility transparent conductive oxide.* Japanese Journal of Applied Physics Part 2-Letters & Express Letters, 2007. **46**(25-28): p. L685-L687.

20. Taylor, M.P., D.W. Readey, M.F. van Hest, C.W. Teplin, J.L. Alleman, M.S. Dabney, L.M. Gedvilas, B.M. Keyes, B. To, and J.D. Perkins, *The Remarkable Thermal Stability of Amorphous In-Zn-O Transparent Conductors.* Advanced Functional Materials, 2008. **18**(20): p. 3169-3178.

21. Van Hest, M., M. Dabney, J. Perkins, and D. Ginley, *High-mobility molybdenum doped indium oxide.* Thin Solid Films, 2006. **496**(1): p. 70-74.

22.   Bhachu, D.S., D.O. Scanlon, G. Sankar, T.D. Veal, R.G. Egdell, G. Cibin, A.J. Dent, C.E. Knapp, C.J. Carmalt, and I.P. Parkin, *Origin of High Mobility in Molybdenum-Doped Indium Oxide.* Chemistry of Materials, 2015. **27**(8): p. 2788-2796.

23.   Morales-Masis, M., S.M. De Nicolas, J. Holovsky, S. De Wolf, and C. Ballif, *Low-Temperature High-Mobility Amorphous IZO for Silicon Heterojunction Solar Cells.* Ieee Journal of Photovoltaics, 2015. **5**(5): p. 1340-1347.

24.   Farhangi, N., R.R. Chowdhury, Y. Medina-Gonzalez, M.B. Ray, and P.A. Charpentier, *Visible light active Fe doped TiO_2 nanowires grown on graphene using supercritical CO_2.* Applied Catalysis B-Environmental, 2011. **110**: p. 25-32.

25.   Garcia-Gonzalez, C.A., M.C. Camino-Rey, M. Alnaief, C. Zetzl, and I. Smirnova, *Supercritical drying of aerogels using CO_2: Effect of extraction time on the end material textural properties.* Journal of Supercritical Fluids, 2012. **66**: p. 297-306.

26.   Badawy, W.A., *Preparation, electrochemical, photoelectrochemical and solid-state characteristics of indium-incorporated TiO_2 thin films for solar cell fabrication.* Journal of Materials Science, 1997. **32**(18): p. 4979-4984.

27.   Liu, Y., G. Chen, C. Zhou, Y. Hu, D. Fu, J. Liu, and Q. Wang, *Higher visible photocatalytic activities of nitrogen doped In_2TiO_5 sensitized by carbon nitride.* J Hazard Mater, 2011. **190**(1-3): p. 75-80.

28.   Lucky, R.A., Y. Medina-Gonzalez, and P.A. Charpentier, *Zr doping on one-dimensional titania nanomaterials synthesized in supercritical carbon dioxide.* Langmuir, 2010. **26**(24): p. 19014-19021.

29.   Chowdhury, P., G. Malekshoar, M.B. Ray, J. Zhu, and A.K. Ray, *Sacrificial Hydrogen Generation from Formaldehyde with Pt/TiO_2 Photocatalyst in Solar Radiation.* Industrial & Engineering Chemistry Research, 2013. **52**(14): p. 5023-5029.

30.   Sui, R., A. Rizkalla, and P.A. Charpentier, *Experimental study on the morphology and porosity of TiO_2 aerogels synthesized in supercritical carbon dioxide.* Microporous and Mesoporous Materials, 2011. **142**(2-3): p. 688-695.

31.   You, M., T.G. Kim, and Y.-M. Sung, *Synthesis of Cu-Doped TiO_2Nanorods with Various Aspect Ratios and Dopant Concentrations.* Crystal Growth & Design, 2010. **10**(2): p. 983-987.

32.   Susha, A.S., A.A. Lutich, C. Liu, H. Xu, R. Zhang, Y. Zhong, K.S. Wong, S. Yang, and A.L. Rogach, *Comparative optical study of colloidal anatase titania nanorods and atomically thin wires.* Nanoscale, 2013. **5**(4): p. 1465-1469.

33.   Rangel-Porras, G., E. Ramos-Ramírez, and L.M. Torres-Guerra, *Mesoporous characteristics of crystalline indium-titania synthesized by the sol-gel route.* Journal of Porous Materials, 2009. **17**(1): p. 69-78.

34.   Irie, H., K. Kamiya, T. Shibanuma, S. Miura, D.A. Tryk, T. Yokoyama, and K. Hashimoto, *Visible Light-Sensitive Cu(II)-Grafted TiO$_2$ Photocatalysts: Activities and X-ray Absorption Fine Structure Analyses.* Journal of Physical Chemistry C, 2009. **113**(24): p. 10761-10766.

35.   Hsu, C.P., K.M. Lee, J.T.W. Huang, C.Y. Lin, C.H. Lee, L.P. Wang, S.Y. Tsai, and K.C. Ho, *EIS analysis on low temperature fabrication of TiO$_2$ porous films for dye-sensitized solar cells.* Electrochimica Acta, 2008. **53**(25): p. 7514-7522.

36.   Kim, J.H., K.P. Kim, D.H. Kim, and D.K. Hwang, *Electrospun ZnO Nanofibers as a Photoelectrode in Dye-Sensitized Solar Cells.* J Nanosci Nanotechnol, 2015. **15**(3): p. 2346-2350.

37.   Zheng, D.J., M.D. Ye, X.R. Wen, N. Zhang, and C.J. Lin, *Electrochemical methods for the characterization and interfacial study of dye-sensitized solar cell.* Science Bulletin, 2015. **60**(9): p. 850-863.

Chapter 5

5 Photocatalytic Hydrogen Production using active Bismuth Titanate nanowires

Bismuth titanate and undoped TiO_2 nanowires were prepared using a unique sol-gel methodology in supercritical CO_2, using titanium alkoxide, bismuth acetate, and acetic acid as the polycondensation agent. Nanowire formation was confirmed by SEM and TEM for all bismuth titanate and undoped TiO_2. X-ray and XPS results confirmed the formation of bismuth titanate nanowires and the level of bismuth doping, while high surface area was confirmed by BET analysis. Sacrificial hydrogen production under solar light irradiation (100 mW/cm^2) was evaluated using different bismuth doped titania nanowires. Contrary to the other studies, this study reports for the first time that bismuth titanate is capable of photocatalytic hydrogen production without further doping using any noble or transition metal.

5.1 Introduction

Photocatalysis is a widely studied and applied method for the remediation of waste streams due to the ready availability of relatively inexpensive photocatalyst and capacity for free solar energy to carry out the reactions[1]. A large number of different photocatalytic systems have been investigated in recent years for their environmental applications or alternative energy production.[2] Producing hydrogen from sunlight using solar photocatalysis is a promising alternative for clean energy production. Titanium dioxide is the choice of photocatalyst in many applications due to its low band gap energy and low cost.[3] Further enhancement of its performance has been achieved by doping with noble metals including Pt and Au or transition metals like Cu, Ni, Fe, etc. with focus on reduction of electron-hole recombination or increase in visible light absorption by the photocatalyst. [4]

With increasing environmental concerns and the need for 'green reagents', interest in bismuth and its compounds has increased significantly over the last few years.[5] In particular, bismuth titanate has received significant interest for photocatalytic activities in visible light to degrade organic pollutants.[6] Bismuth (III) compounds are useful reagents in organic synthesis because of their low toxicity, low cost and ease of handling. Enhanced visible light absorption is a result of hybridization of Bi (6p), Bi (6s) with Ti (3d), O (2p) orbitals, respectively to provide the visible shift. Photocatalytic removal of organic pollutants in water and wastewater applications has been the main objective of these studies involving this promising photocatalyst. Different morphologies of bismuth titanate are reported with varying photocatalytic performances.[7] Yao et al. (2004) prepared a perovskite phase bismuth titanate nanoparticle with diameter between 10-90 nm that showed excellent photodegradation of methyl orange (90 % removal occurs in about 4 hours). Lin et al. prepared bismuth titanate microspheres using an autoclave method for methyl orange degradation.[8, 9] Recently, bismuth doped TiO_2- graphene nanocrystals prepared by an autoclave method by the Charpentier group were tested as a hot carrier transport in dye-sensitized solar cell (DSSC). [10] Bismuth titanate nanorods or nanowires are rarely reported in the literature until recently when Pei et al. (2015) synthesized bismuth titanate nanorods (50-200 nm length and 2 µm diameter) using a

facile hydrothermal process without additives for the visible light photodegradation of methylene blue and Rhodamine B.

Very few studies on photocatalytic hydrogen production using bismuth titanate are reported in the literature compared to its photocatalytic or its ferromagnetic applications.[11, 12]   Kudo and Hijii (1999) were the first group of researchers to report evolution of hydrogen from water, albeit at a low rate of 0.6 µmol H_2/hr using layered oxide photocatalysts consisting of Bi^{3+}.   On the other hand, Merka et al. (2014) demonstrated hydrogen production only after loading bismuth titanate with platinum and platinum/chromium as a co-catalyst.[13, 14]   These experimental investigations are in contradiction with density functional theory (DFT) calculations by Murugesan et al.(2015), which indicated that bismuth titanate has all the requirements to produce hydrogen by water splitting, yet no significant hydrogen production was reported using undoped bismuth titanate.[15] The objective of the current work is to synthesize bismuth titanate nanowires with different bismuth to titanium ratios using a $ScCO_2$ sol-gel process and evaluate their photocatalytic sacrificial hydrogen production potential, helping to rationalize the contradictory results reported in the literature.

5.2   Experimental Details

5.2.1   Chemicals and Materials

Bismuth (III) acetate (99.99%), titanium (IV) isopropoxide (TIP) (97%), acetic acid (99.7%), and formaldehyde solution (36.5%) were purchased from the Aldrich Chemical Company, Oakville, ON, Canada and used without further purification. Instrument grade liquid carbon dioxide (99.99%) from Air Liquide Canada was delivered by a syringe pump (Isco 260D) into a 10 mL view cell reactor equipped with a pressure transducer, heating tape, and thermocouple for temperature control. The details of the reactor are provided in Lucky et al.[16]

5.2.2   Synthesis of Bismuth Titanate Nanowires

In a typical experiment, predetermined amounts of titanium isopropoxide (TIP) and bismuth (III) acetate were quickly placed in the 10 mL view cell, followed by addition of

acetic acid, and CO_2. The amount of bismuth (III) acetate was varied to prepare four different concentrations of bismuth titanate nanowires. The view cell was heated to 60 ºC and subsequently pressurized to 5000 psig using $ScCO_2$. A magnetic stirrer was used to ensure uniform mixing of the reactants. The hydrolysis rate was controlled by adjusting metal precursors to acetic acid molar ratios in the range of 1:5-6. During the gelation stage, a light pink color was observed in about 30 and 40 minutes for bismuth doped titania before changing to white color the next day. After five days of aging, the samples were washed with 100 mL of $scCO_2$ at a rate of 0.3 mL/min to remove unreacted materials and by-products, and to prevent collapse of the gel network. The prepared bismuth doped TiO_2 sol-gel was then calcined in air at 500 ºC for 2 hours. The calcination temperature was selected based on the thermal gravimetric analysis (TGA) results (not shown) where bismuth doped catalysts showed removal of organic components at about 450 ºC. Undoped titanium dioxide nanowires were prepared in a similar way without the addition of bismuth (III) acetate.

5.2.3   Characterization of Bismuth Titanate Nanowires

The morphological features of synthesized nanowires were investigated by scanning electron microscopy (SEM) (Model LEO 1530) and transmission electron microscopy (TEM) (Model JEOL 2010F) capable of dark field scanning transmission electron microscopy (STEM) and coupled with energy dispersive X-ray spectroscopy. For TEM charaterization, the powdered samples were dispersed in ethanol by sonication for 15 min and then casted on a copper grid covered with holey carbon film. Samples for SEM imaging were prepared by applying the powder directly to a carbon adhesive tape. The BET (Brunauer-Emmett-Teller) surface area and BJH (Barrett-Joyner-Halenda) pore size and volume analysis were determined from nitrogen adsorption and desorption isotherm data obtained at 77 K with a constant-volume adsorption apparatus (Micromeritic Tristar II) using N_2 gas (99.995% pure; obtained from Praxair, Canada). The prepared samples were degassed under nitrogen gas flow at 150°C overnight before measurements. Structural analysis of the samples was performed using an X-ray powder diffractometer (Rigaku Miniflex XRD, Texas, U.S.A.), fitted with a rotating sample holder, a scintillation counter detector and a divergent beam utilizing a Cu K source of X-rays

($= 1.5418 \degree A$). The XPS analysis was carried out with a Kratos Axis Ultra spectrometer using a monochromatic Al K (alpha) source (15mA, 14kV).

5.2.4   Photocatalytic Hydrogen Production

The experimental setup for photocatalytic sacrificial hydrogen production was reported previously. [17] A pyrex glass photocatalytic reactor (11 cm x 6.3 cm) with a volume of 350 ml was used to carry out the experiments. Most of the experiments were conducted using 50 mg of photocatalyst in 50 ml solution using 0.16 M formaldehyde as the sacrificial agent. Prior to solar irradiation, the solution was agitated at 500 rpm using a magnetic stirrer (Heidolph) for 1 hour with simultaneous nitrogen purging at ambient pressure to eliminate oxygen from the solution. The reactor contents were irradiated using a solar simulator (model: SS1 KW, Sciencetech) with a xenon arc lamp. The solar lamp produces irradiance at full power (1000 watts), which is similar to the global solar spectrum at sea level of 100 mWcm^{-2}. The photocatalytic reactor was air-cooled with a fan to keep the temperature constant at ambient conditions.

A Gas Chromatography (Schimadzu GC 2014, Heyesep D packed column: 10 m length, 2 mm ID, and 2 µm film thickness, with thermal conductivity detector (TCD)) was utilized for quantification of produced hydrogen. The calibration of the GC was conducted using a 1000 ml gas-sampling bulb (Supelco), which was filled with nitrogen and hydrogen to yield hydrogen calibration gas with desired concentrations.

5.3   Results and Discussion

The morphology of bismuth titanate and TiO$_2$ nanowires was examined by SEM, with a typical result shown in Figure 5-1a for bismuth titanate nanowires. The TEM images of bismuth titanate nanowires shown in Figure 5-1 b-c demonstrate clear uniformity and porosity of these nanowires. Higher magnification of selected tips shows the grain boundaries and different orientations of crystalline lattice providing multiple active sites for photocatalytic processes to take place at the boundaries of these grains (about 5 nm) as shown in Figure 5-1d.
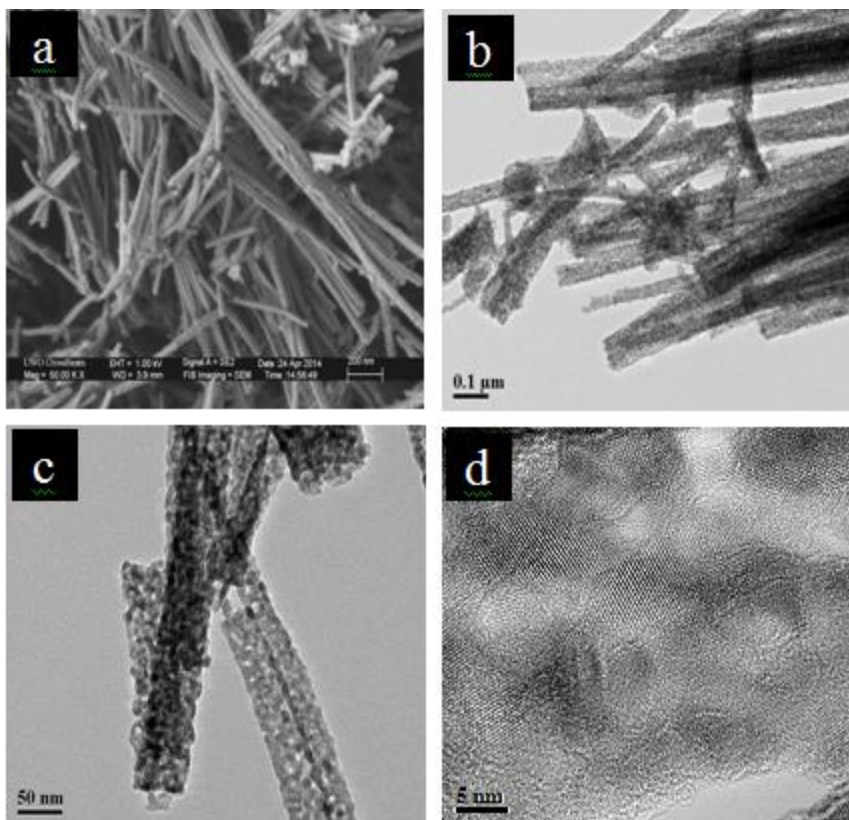
Figure 5-1: SEM image of bismuth titanate nanowires (a), and TEM images of single nanowire (b), Higher TEM magnification of b (c) showing grain sizes which is about 5 nm.

Greater details of the bismuth titanate morphology using high resolution TEM are shown in Figure 5-2. A selected site on a bismuth titanate nanowire is shown with grains in different directions with approximate size of 5-7 nm as labeled in Figure 5-2a. Figure 5-2 b-c are for selected sites showing a magnification on the lattice and enhanced image by applying inverse fast fourier transform (FFT) for calculation of the lattice distance, respectively. The lattice distance was calculated to be 0.33 nm by average spacing of 10 lattice spaces as shown in the histogram in Figure 5-2d. Similar processing techniques were applied to the other two sites which showed a lattice distance of 0.33 nm related to anatase phase and the two crossed lattices of 0.35 nm in Figure 5-2e and Figure 5-2 g, respectively.
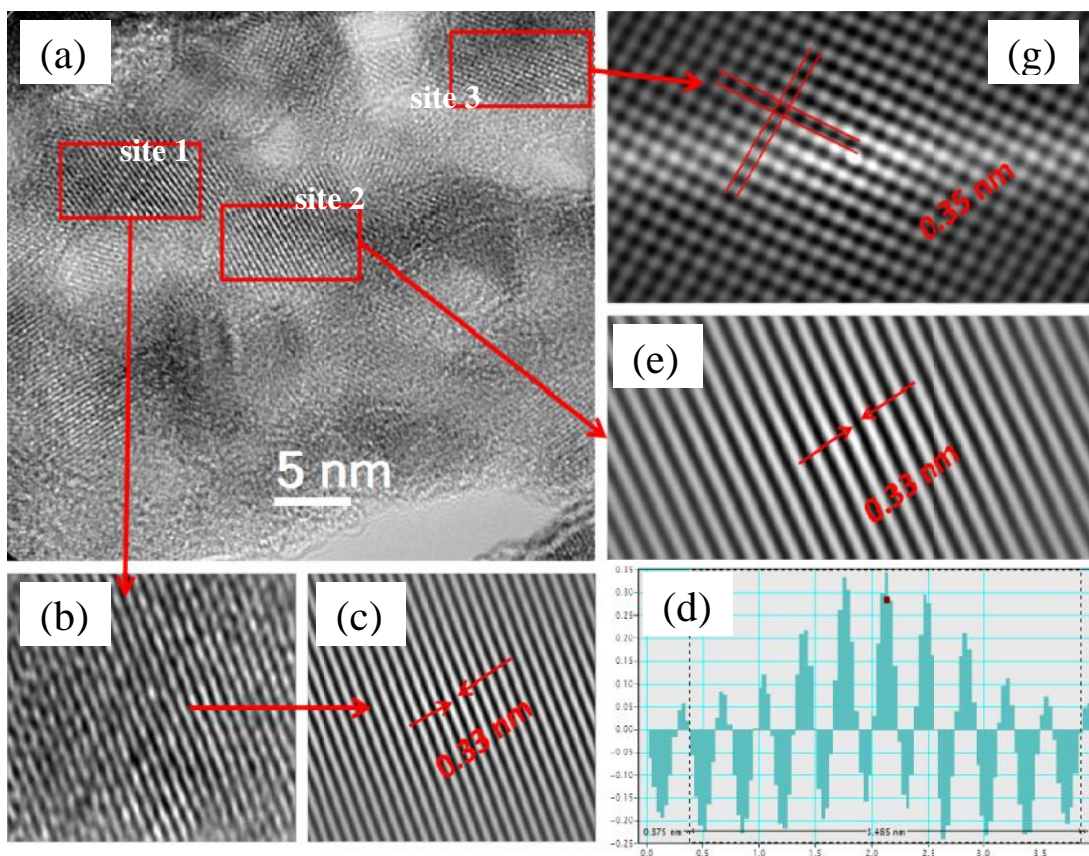
Figure 5-2: HRTEM images of bismuth titanate nanowire (a), High resolution TEM of selected site 1 (b), enhancement of (b) using inverse FFT (c), histogram of (c) calculating lattice distance (d), enhanced inverse FFT selected site 2 (e), enhanced inverse FFT of cross planes for lattice distance for site 3 (g).

To illustrate the degree of dopant metal dispersion throughout the nanowires, TEM mapping using energy dispersive X-ray spectroscopy (EDS) is shown for bismuth titanate nanowires in Figure 5-3. The nanowires showed uniform dispersion of bismuth metal throughout the nanowires with bismuth loadings of about 1, 2, and 2.5 atomic %. The high degree of dispersion of bismuth throughout the bismuth titanate nanowires is attributed to the synthesis methodology using $ScCO_2$ as a solvent and drying agent. This unique synthesis methodology helped in enhancing the precursors' solubility, preventing the collapse of formed networks during gelation due to the zero surface tension of $ScCO_2$ during the aging and washing stages as described in details previously.[18]
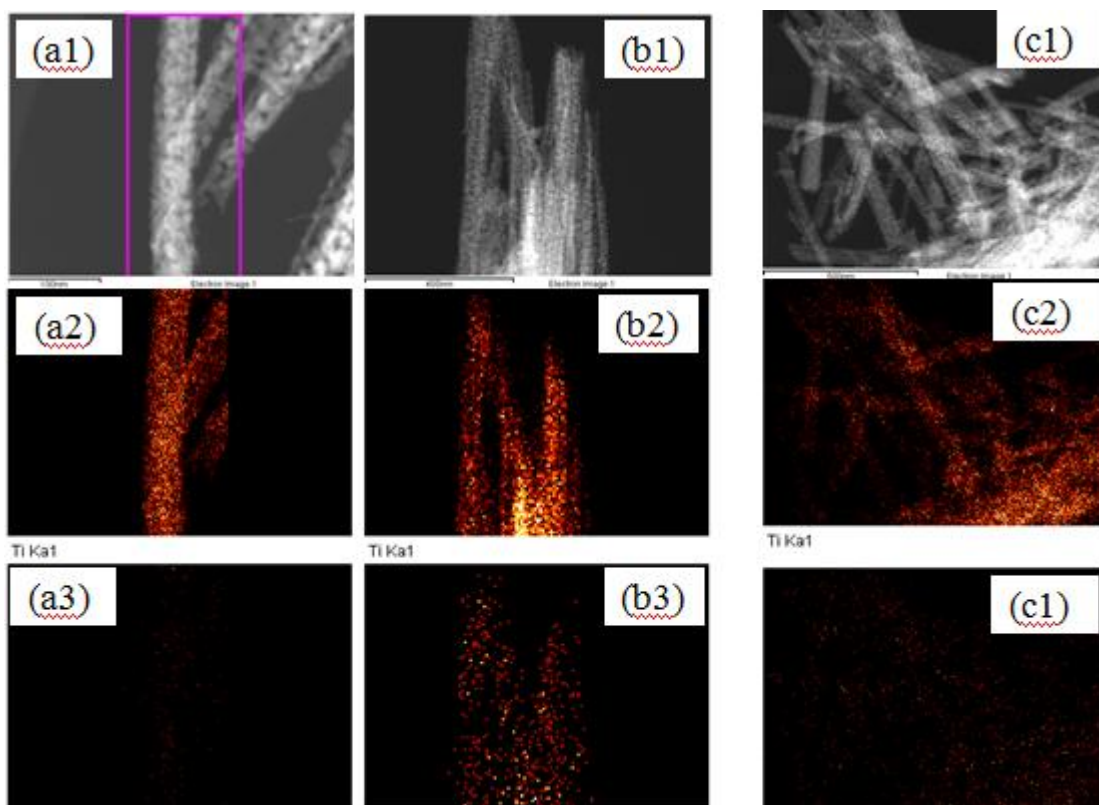
Figure 5-3: STEM images of bismuth titanate nanowires showing porosity of nanowires as in dark field (a1, b1, c1), EDS mapping shows the dispersion of titanium in (a2, b2,c2), and bismuth within nanowires in (a3,b3,c3) for bismuth loading of 1, 1.4 and 2.5 at % respectively.

Infrared spectroscopic results showed successful condensation during the sol-gel chemistry between TIP and bismuth acetate as three new peaks were formed at 1753, 1701, and 737 cm^{-1} in the produced gel which can be attributed to C=O and Ti-O stretching. Furthermore, disappearance of absorption peaks at 1116, 990, and 848 cm^{-1} of TIP is attributed to Ti-O-C and Ti-O stretch vibrations, shown in Figure 5-4a. In addition, it was observed that peaks at 1116 cm^{-1} and the band around 1375 cm^{-1} of TIP were decreasing as the amount of bismuth acetate increased from 1.4 mol % to 7 mole %. This is due to more of the titanium alkoxide is reacting with bismuth acetate as shown in Figure 5-4b.[19-22] Furthermore, the bands around 1735 cm^{-1} and 1430 cm^{-1} are assigned to COO vibrations of monodentate and bidentate bridging, respectively. It is expected that the bidentate bridging is more likely as the band around 1735 cm^{-1}, also can be assigned to free COO acid in the formed gel.
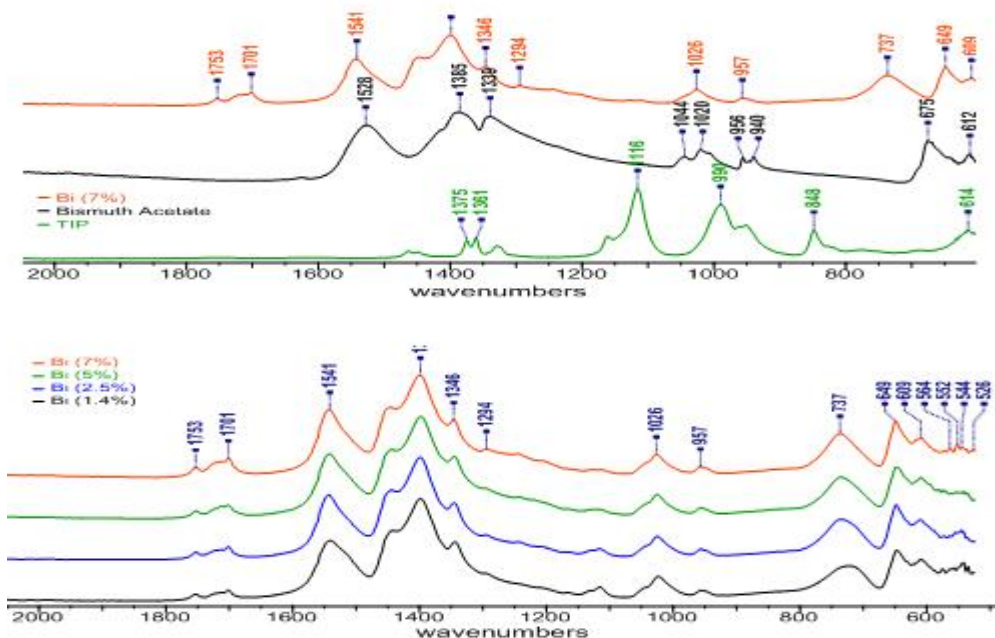
Figure 5-4: FT-IR spectra of (a) TIP and bismuth acetate and their resulting sol-gel product at 7 mole % bismuth, (b) is comparing the resulting sol-gel of (a) at different loadings of bismuth acetate namely 1.4, 2.5, 5, and 7 mole % bismuth.

The BET surface areas of all four samples of bismuth titanate Bi1, Bi2, Bi3, and Bi4 nanowires were measured as 80, 85, 84 and 99 m^2/g, respectively. It is known that the surface area decreases as a material's dimensionality increases. For example, nanoparticles have higher surface areas compared to nanorods and nanowires.[23, 24] Despite the formation of nanowires, the produced undoped TiO_2 nanowires had comparable surface areas to Degussa P25 (also examined in this work) which was measured as 58 and 50 m^2/g, respectively. The relatively high surface area of the nanowires can be attributed to pores formation during the sol-gel synthesis of nanowires and more crucially retaining of the pores by $ScCO_2$ drying as shown by the dark field STEM images in Figure 5-3.

The crystalline structures of the calcined bismuth titanate nanowires were investigated using X-ray Diffraction. The XRD patterns of bismuth titanate nanowires were compared with XRD spectra of the undoped TiO_2 nanowires that have characteristic peaks at 25^0,

38^0, 48^0, 53^0, 55^0, 63^0, 70^0 and 76^0 shown in Figure 5-5a, which are an excellent match to anatase phase (PDF 01-086-1157). X-Ray diffraction of bismuth titanate nanowires with different loadings showed additional peaks with $2\theta = 27^0$ and 31^0, and 36^0 which are related to bismuth. The bismuth characteristic peak around 27^0 corresponds to the plane [012] of rombohedral bismuth. The peak at 31^0 (Figure 5-5b) shows that the intensity of these peaks increased as the bismuth doping level increased. A shift to lower angle of the anatase peak of $2\theta = 25.5^0$ was observed in Figure 5-5c, with increased bismuth doping confirming the loading of bismuth into titania lattice as reported in literature.[25] This shift can be attributed to doping of the larger ionic radius of bismuth (0.103 nm) into the lattice of titania which is (0.061 nm) as shown in Figure 5-5b. In addition, a gradual change of intensity ratio between peaks at 54^0 and 55^0 occurs, with these two peaks merging into one peak at 54.5^0, as more bismuth was added into the nanowires. This also was the case for peaks at 68.9^0 and 70.4^0 as shown in Figure 5-5a. Moreover, no change was observed for peaks at 48^0 and 62^0 except a drop in intensity of the peak at 48^0 compared to peak at 54.5^0. [26, 27] The change to the titanium dioxide lattice structure confirmed doping of bismuth, which is near the surface as its ions are larger than titania, which may enhance the photocatalytic activity of the bismuth titanate nanowires by increased charge transfer on nanowire surface.
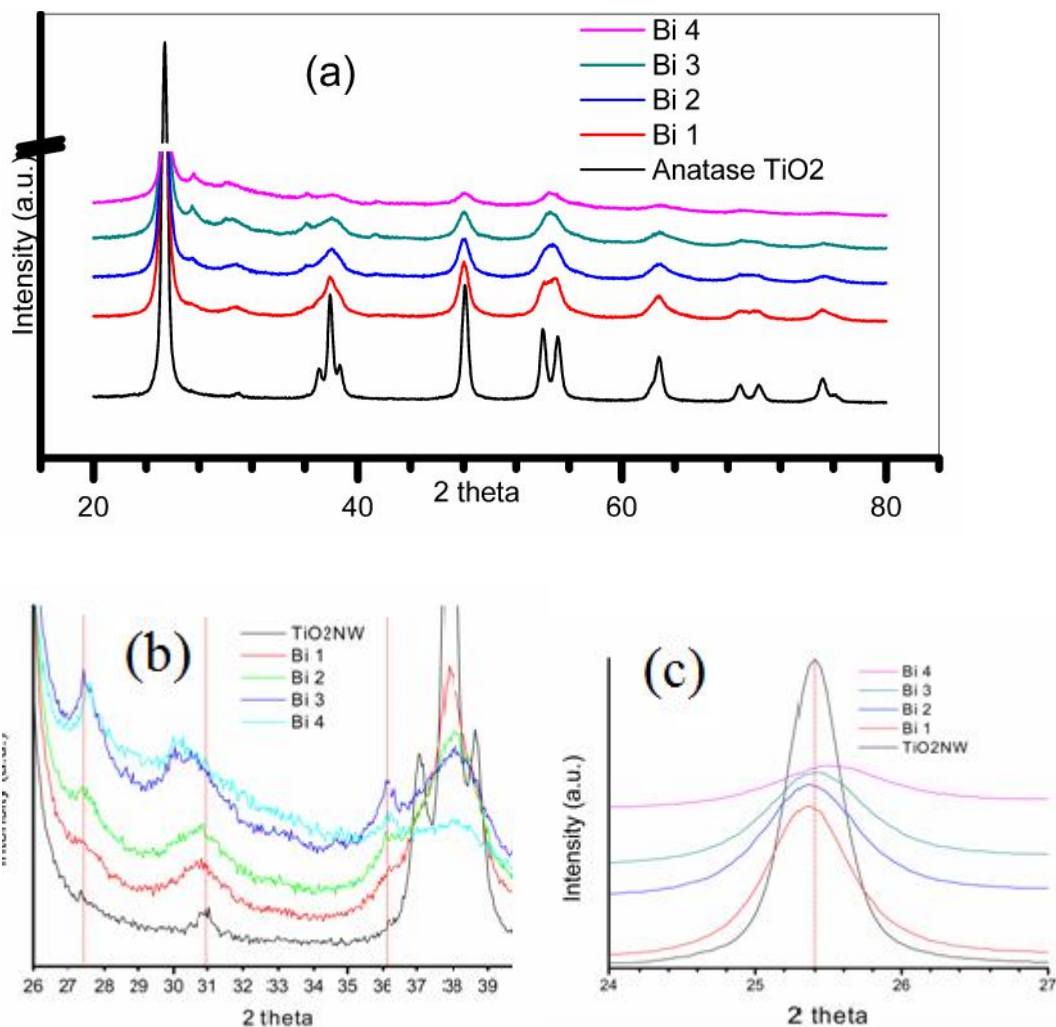
Figure 5-5: XRD results of undoped TiO$_2$ nanowires and bismuth titanate nanowires.

Both the chemical oxidation states of bismuth and titanium and their concentrations were determined by XPS analysis. In all the prepared bismuth titanate nanowires, the chemical state of titanium is (IV) with a binding energy peak at 458.85 eV, depending on its interaction with the dopant metal as shown in Figure 5-6. The XPS analysis showed a characteristic binding energy peak of Bi 4f 7/2 at 159.46 eV, which indicates the existence of Bi (III).
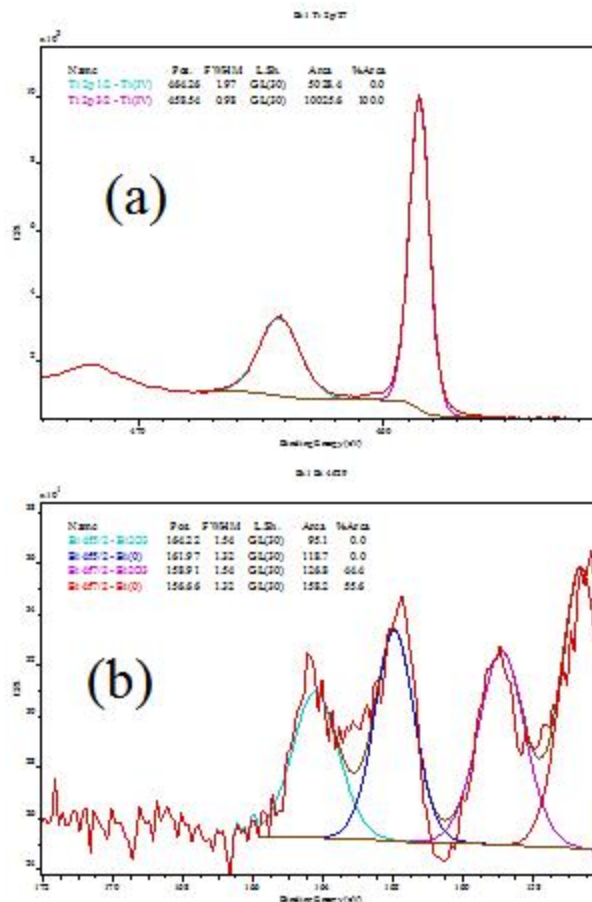
Figure 5-6: XPS results of bismuth titanate nanowire showing (a) titanium (b) bismuth.

5.3.1   Photocatalytic Hydrogen Production

Photocatalytic activities of the synthesized bismuth titanate nanowires and undoped TiO_2 nanowires were investigated for sacrificial hydrogen production, with the results shown in Figure 5-7a. Hydrogen generation rates for the tested nanowires and P25 TiO_2 are shown in Figure 5-7b. Hydrogen evolution rates were 0.93, 0.20, µmol-hr^{-1} for P25 TiO_2 and undoped TiO_2 nanowires, respectively. Higher hydrogen amount was produced by bismuth titanate irrespective of bismuth loading, indicating that bismuth titanate has a higher photocatalytic activity than pure P25 or the undoped TiO_2 nanowires. The rates of sacrificial hydrogen production using bismuth titanate nanowires were 6.5, 7.9, and 4.8 µmol-hr^{-1} for 1 mol %, 1.4 mol %, and 2.0 mol % bismuth respectively. These results showed that bismuth doping with 1.4 mol % produced highest amount of hydrogen of 1107 µmol/g-hr followed by 1 mol%, and 2 mol% with hydrogen production of 914

µmol/g-hr, and 668 µmol/g.hr, respectively. These are significant improvements compared to the undoped TiO_2 nanowires, which produced only 28 µmol/g-hr and 130 µmol/g-hr of P25 TiO_2. The results shown in Figure 5-7b indicate that the catalytic activities of all the produced photocatalysts were stable over seven hours of experiment. Optimum bismuth loading was found at about 1.4 mole %, as higher loadings decreased the amount of hydrogen production as shown in Figure 5-8:
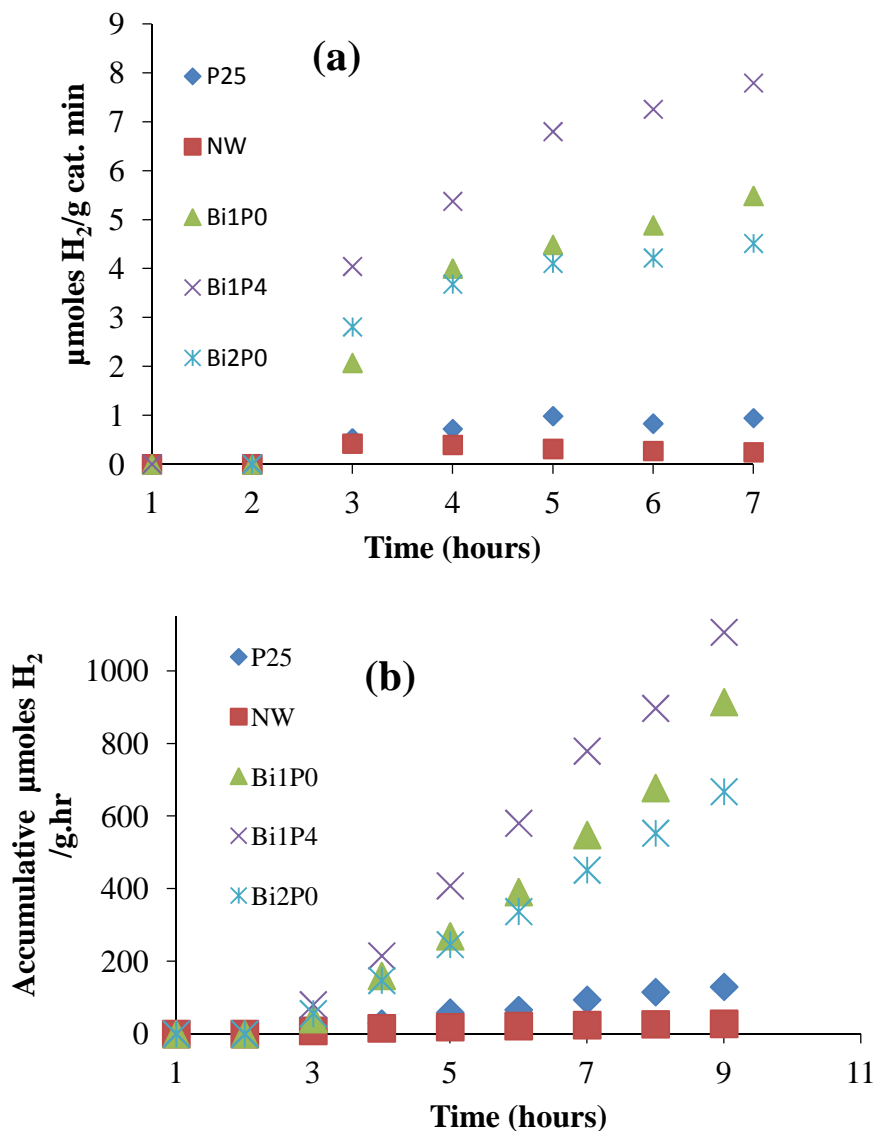
Figure 5-7: Photocatalytic hydrogen production (a) rate of production (b) by bismuth titanate nanowires, P25, and undoped TiO_2 NW.
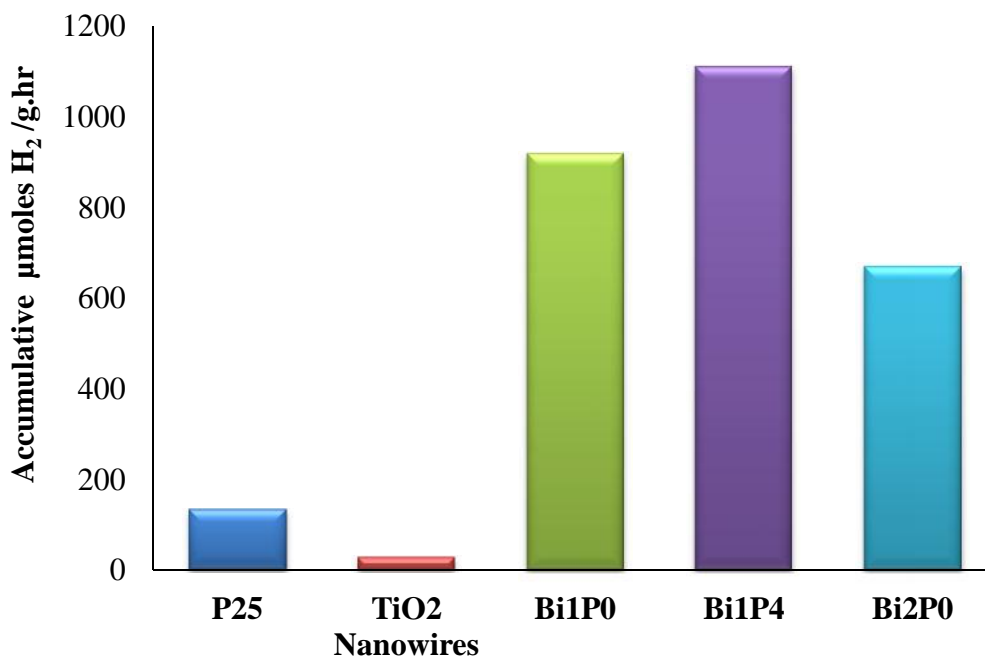
Figure 5-8: Photocatalytic hydrogen production (a) rate of production (b) by bismuth titanate nanowires, P25, and undoped TiO_2 NW.

A previous DFT study suggested that bismuth titanate should be doped with transition metals such as Fe, Ni, Cr, Mn, and V to modify the band gap to enable hydrogen production. [15] In 2014, Merka et al, synthesized non-stoichiometric pyrochlore bismuth titanate using an EDTA template in an aqueous sol-gel method and examined its capability to produce hydrogen. They evaluated three non-stoichiometric bismuth titanate catalysts compared to one stoichiometric bismuth titanate catalyst after photodeposition of 3 wt % platinum as a co-catalyst. The results showed that stoichiometric and $Bi_4Ti_3O_{12}$ were inactive production with very minimal hydrogen production.[14] However, in this study bismuth titanate nanowires produced significant amounts of hydrogen, around 8 times more than that of commercial P25, and 40 times more than undoped TiO_2 nanowires. The initial rates of hydrogen production using bismuth titanate nanowires were much higher compared to P25 and undoped nanowires. Using supercritical CO_2 as solvent, uniform nanowires with high surface area comparable to the nanoparticles were prepared that provided the required higher sites for reaction to take place with better surface charge transport and separation. In addition, doping with bismuth reduced the

conduction band energy by about 0.4 eV. This was achieved by combining Ti (3d) and Bi (6p) molecular orbitals at a lower conduction band position. The valance band position was also shifted to a lower positive potential by mixing Bi (6s) and O (2p) orbitals. This shift in the valance band enhanced the migration of photogenerated holes from the TiO_2 valance band to the Bi valance band resulting in more effective charge separation. The holes were further consumed by sacrificial formaldehyde in the solution leaving electrons to accumulate on bismuth sites to reduce H^+ to hydrogen gas as illustrated in Figure 5-9.
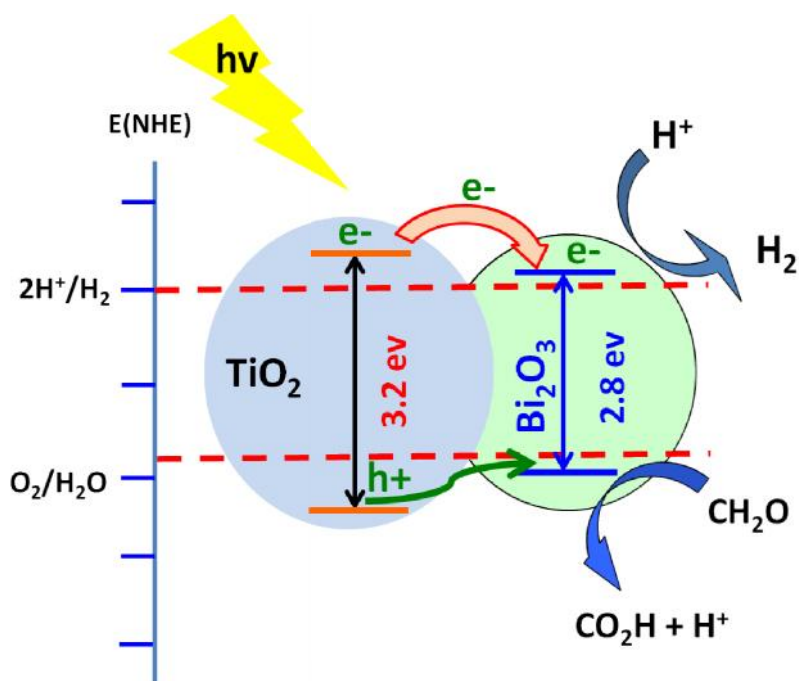
Figure 5-9: Schematic energy levels and photocatalytic hydrogen production by bismuth titanate nanowires.

5.4   Conclusions

Bismuth titanate nanowires with high photocatalytic activity to produce sacrificial hydrogen were successfully synthesized using a $ScCO_2$ sol-gel methodology. Significant amounts of hydrogen was produced by these nanowires irrespective of the bismuth loading level compared to commercial P25 and undoped titanium nanowires. This is attributed to their high surface areas and most importantly to the large number of grain boundaries that created active sites for reactions to take place. Energy band alignments with respect to TiO_2 and water reduction potential enabled efficient electron-hole separation and improved the charge transfer to bismuth for hydrogen generation. Bismuth titanate nanowires are promising for hydrogen generation with about 8 times more hydrogen than that produced by P25 and 40 times undoped TiO_2 nanowires prepared using similar approach and tested under similar conditions.

5.5 References

1. Lee, S.S., H. Bai, Z. Liu, and D.D. Sun, *Green approach for photocatalytic Cu(II)-EDTA degradation over TiO$_2$: toward environmental sustainability.* Environ Sci Technol, 2015. **49**(4): p. 2541-2548.

2. Moniz, S.J.A., S.A. Shevlin, D.J. Martin, Z.X. Guo, and J.W. Tang, *Visible-light driven heterojunction photocatalysts for water splitting - a critical review.* Energy & Environmental Science, 2015. **8**(3): p. 731-759.

3. Huang, Q., Z. Ye, and X.D. Xiao, *Recent progress in photocathodes for hydrogen evolution.* Journal of Materials Chemistry A, 2015. **3**(31): p. 15824-15837.

4. Eslava, S., M. McPartlin, R.I. Thomson, J.M. Rawson, and D.S. Wright, *Single-source materials for metal-doped titanium oxide: syntheses, structures, and properties of a series of heterometallic transition-metal titanium oxo cages.* Inorg Chem, 2010. **49**(24): p. 11532-11540.

5. Leonard, N.M., L.C. Wieland, and R.S. Mohan, *Applications of bismuth(III) compounds in organic synthesis.* Tetrahedron, 2002. **58**(42): p. 8373-8397.

6. Gupta, S. and V.R. Subramanian, *Encapsulating Bi2Ti$_2$O$_7$ (BTO) with reduced graphene oxide (RGO): an effective strategy to enhance photocatalytic and photoelectrocatalytic activity of BTO.* ACS Appl Mater Interfaces, 2014. **6**(21): p. 18597-18608.

7. Hou, J.G., Y.F. Qu, D. Krsmanovic, C. Ducati, D. Eder, and R.V. Kumar, *Hierarchical assemblies of bismuth titanate complex architectures and their visible-light photocatalytic activities.* Journal of Materials Chemistry, 2010. **20**(12): p. 2418-2423.

8. Yao, W.F., X.H. Xu, H. Wang, J.T. Zhou, X.N. Yang, Y. Zhang, S.X. Shang, and B.B. Huang, *Photocatalytic property of perovskite bismuth titanate.* Applied Catalysis B-Environmental, 2004. **52**(2): p. 109-116.

9. Lin, X., P. Lv, Q.F. Guan, H.B. Li, H.J. Zhai, and C.B. Liu, *Bismuth titanate microspheres: Directed synthesis and their visible light photocatalytic activity.* Applied Surface Science, 2012. **258**(18): p. 7146-7153.

10. Moula G, M.M., Charpentier PA and *Enhancement of Photocurrent in Dye-Sensitized Solar Cells Using Bismuth Doped TiO$_2$-Graphene as a Hot Carrier Transport. .* J Nanomater Mol Nanotechnol S1:002, 2013.

11. Hu, D., X. Kong, K. Mori, Y. Tanaka, K. Shinagawa, and Q. Feng, *Ferroelectric mesocrystals of bismuth sodium titanate: formation mechanism, nanostructure,*

and application to piezoelectric materials. Inorg Chem, 2013. **52**(18): p. 10542-10551.

12. Nogueira, A.E., E. Longo, E.R. Leite, and E.R. Camargo, *Synthesis and photocatalytic properties of bismuth titanate with different structures via oxidant peroxo method (OPM).* J Colloid Interface Sci, 2014. **415**: p. 89-94.

13. Kudo, A. and S. Hijii, *H_2 or O_2 Evolution from Aqueous Solutions on Layered Oxide Photocatalysts Consisting of Bi^{3+} with 6s2 Configuration and d0 Transition Metal Ions.* Chemistry Letters, 1999. **28**(10): p. 1103-1104.

14. Merka, O., D.W. Bahnemann, and M. Wark, *Photocatalytic hydrogen production with non-stoichiometric pyrochlore bismuth titanate.* Catalysis Today, 2014. **225**: p. 102-110.

15. Murugesan, S., M.N. Huda, Y.F. Yan, M.M. Al-Jassim, and V. Subramanian, *Band-Engineered Bismuth Titanate Pyrochlores for Visible Light Photocatalysis.* Journal of Physical Chemistry C, 2010. **114**(23): p. 10598-10605.

16. Lucky, R.A., Y. Medina-Gonzalez, and P.A. Charpentier, *Zr doping on one-dimensional titania nanomaterials synthesized in supercritical carbon dioxide.* Langmuir, 2010. **26**(24): p. 19014-19021.

17. Chowdhury, P., G. Malekshoar, M.B. Ray, J. Zhu, and A.K. Ray, *Sacrificial Hydrogen Generation from Formaldehyde with Pt/TiO_2 Photocatalyst in Solar Radiation.* Industrial & Engineering Chemistry Research, 2013. **52**(14): p. 5023-5029.

18. Sui, R., A. Rizkalla, and P.A. Charpentier, *Experimental study on the morphology and porosity of TiO_2 aerogels synthesized in supercritical carbon dioxide.* Microporous and Mesoporous Materials, 2011. **142**(2-3): p. 688-695.

19. Lynch, C.T., K.S. Mazdiyasni, W.J. Crawford, and J.S. Smith, *Infrared Spectra of Transition Metal Alkoxides.* Analytical Chemistry, 1964. **36**(12): p. 2332-&.

20. Leaustic, A., F. Babonneau, and J. Livage, *Structural investigation of the hydrolysis-condensation process of titanium alkoxides $Ti(OR)_4$ (OR = OPr-iso, OEt) modified by acetylacetone. 2. From the modified precursor to the colloids.* Chemistry of Materials, 1989. **1**(2): p. 248-252.

21. Burgos, M. and M. Langlet, *The sol-gel transformation of TIPT coatings: a FTIR study.* Thin Solid Films, 1999. **349**(1-2): p. 19-23.

22. Urlaub, R., U. Posset, and R. Thull, *FT-IR spectroscopic investigations on sol-gel-derived coatings from acid-modified titanium alkoxides.* Journal of Non-Crystalline Solids, 2000. **265**(3): p. 276-284.

23.   You, M., T.G. Kim, and Y.-M. Sung, *Synthesis of Cu-Doped TiO$_2$ Nanorods with Various Aspect Ratios and Dopant Concentrations.* Crystal Growth & Design, 2010. **10**(2): p. 983-987.

24.   Susha, A.S., A.A. Lutich, C. Liu, H. Xu, R. Zhang, Y. Zhong, K.S. Wong, S. Yang, and A.L. Rogach, *Comparative optical study of colloidal anatase titania nanorods and atomically thin wires.* Nanoscale, 2013. **5**(4): p. 1465-1469.

25.   Zhao, W., X. Wang, H. Sang, and K. Wang, *Synthesis of Bi-doped TiO$_2$ Nanotubes and Enhanced Photocatalytic Activity for Hydrogen Evolution from Glycerol Solution.* Chinese Journal of Chemistry, 2013. **31**(3): p. 415-420.

26.   McInnes, A., J.S. Sagu, and K.G.U. Wijayantha, *Fabrication and photoelectrochemical studies of Bi$_2$Ti$_2$O$_7$ pyrochlore thin films by aerosol assisted chemical vapour deposition.* Materials Letters, 2014. **137**: p. 214-217.

27.   Kahlenberg, V. and H. Bohm, *The Structures of Alpha-Bi$_2$ti$_4$o$_{11}$ and Beta-Bi$_2$ti$_4$o$_{11}$.* Acta Crystallographica Section B-Structural Science, 1995. **51**(1): p. 11-18.

Chapter 6

6   Bismuth Titanate Nanowires as Photoanode for Dye Sensitized Solar Cells

Bismuth titanate nanowires were prepared using a unique sol-gel methodology in supercritical CO_2 using titanium alkoxide, acetic acid as the polycondensation agent, and bismuth dopant to prepare 1.4 -7 atomic % catalyst. The methodology produced uniformly dispersed dopants integrated into nanowires with diameters from 80-100 nm and high aspect ratios from 15-25 as observed by SEM. XPS results confirmed the formation and the composition of bismuth titanate nanowires. The performance of various dye sensitized solar cells (DSSC) using different levels of bismuth in the nanowires were evaluated using solar light irradiation at 100 mW/cm^2. A bismuth doping level of 1.4 mol % with respect to Ti showed superior photoelectric performance in the DSSC cells, which was about 7.5 and 1.5 times greater compared to pure titanium nanowires and P25, respectively. Adding bismuth into the nanowires enhanced the harvesting of visible light and reduced the recombination of electron and holes.

6.1 Introduction

Nano-sized TiO_2 is the most widely examined photocatalyst for many photocatalytic and photoelectrical applications due to its numerous beneficial properties including high chemical and thermal stability, non-corrosivity, abundance, and cost effectiveness.[1] Despite all the benefits, poor activation of TiO_2 by visible light (TiO_2 absorbs only about 5% sunlight) and the rapid recombination of photo-generated electron/hole pairs have limited its efficiency, requiring future improvements for large scale application.[2] [3] Many investigations have been conducted to decrease the effect of the charge recombination and to increase the efficiency of solar light utilization, with a focus on doping TiO_2 using various noble and transition metals such as Pt, Au, Pd, Rh, Ni, Cu, Ag, etc. [4] [5] Doping TiO_2 also induces a red shift in the absorption spectrum, making it possible for visible light activation, enhancing the energy harvesting efficiency of this semiconductor.[6]

In particular, bismuth titanate has gained significant research interest for photocatalytic activities in visible light to degrade organic pollutants. [7] Enhanced visible light absorption is a result of hybridization of Bi (6p), Bi (6s) with Ti (3d), O (2p) orbitals, respectively to provide the visible shift. Bismuth titanate has been widely studied in the literature, with many reports on different preparation methods, that have yielded different morphologies with varying photocatalytic performances. [8-10] Yao et al. (2004) prepared perovskite phase nanoparticles of bismuth titanate with diameter between 10-90 nm that showed excellent photodegradation of methyl orange (90 % removal occurred in about 4 hours). [11] However, only a few studies on dye sensitized solar cells using bismuth titanate as photoanode are reported in the literature compared to its photocatalytic or ferromagnetic applications.[12, 13] In addition, bismuth titanate nanorods or nanowires are rarely reported in literature (Pei et al., 2015). Recently, bismuth doped TiO_2-graphene nanocrystals prepared by an autoclave method were tested as a hot carrier transport in DSSCs. [14] Limited photo-generated electrons in solar cells is due to low excitation energy available from direct sunlight at the titanium dioxide photoanode. The energy required for excitation of TiO_2 is about 3.2 eV, which lies in the UV region of sunlight. Even a slight extension of absorption spectra in the visible range

would contribute significantly to generation of electrons. These photogenerated electrons with their corresponding holes should be managed in DSSC's for reduced recombination. Photogenerated electrons can recombine with excited dye molecules or recombine with holes at the surface of the nanostructure material. However, recombination with dye molecules is not critical due to the small lifetime of excited dye molecules.[15] Furthermore, collection of injected electrons can be improved by reducing the percolation pathways by using nanowires in the photoanode, which have direct percolation pathways to thin conductive oxide (TCO) as compared to the tortuous paths in nanoparticles. For these reasons, selection of the doping material that has a high electron mobility, prepared with efficient metal dispersion to reduce recombination sites is considered an effective method to improve the photoanode performance. [16]

Recently, supercritical carbon dioxide ($ScCO_2$) has been shown to produce high aspect ratio nanofibers/wires of titania with high surface areas and porosities.[17] $ScCO_2$ is an inexpensive and green alternative to conventional organic solvents; it is environmentally benign and non-flammable with low viscosity, zero surface tension and high diffusivity, which are favorable for synthesizing fine and uniform nanomaterials with porous nanostructure.[18] However, nanowires with high aspect ratio and well defined structures are yet challenging to prepare and to the best of our knowledge very limited preparation methods are reported if any and specially tested for dye sensitized solar cell application. Therefore, this work focuses on the synthesis and characterization of bismuth titanate nanowires with different bismuth to titanium ratios using a $scCO_2$ sol-gel process. The performances of produced nanomaterials for DSSC application were evaluated.

6.2   Experimental Details

6.2.1   Chemicals and Materials

Bismuth (III) acetate (99.99%), titanium (IV) isopropoxide (TIP) (97%), acetic acid (99.7%), ethylcellulose, and terpineol were purchased from the Aldrich Chemical Company, Oakville, ON, Canada and used without further purification. Instrument grade liquid carbon dioxide (99.99%) from Air Liquide Canada was delivered by a syringe pump (Isco 260D) into a 10 mL view cell reactor equipped with a pressure transducer,

heating tape, and thermocouple for temperature control. The details of the reactor are provided in an earlier publication (Lucky et al.[19]).

6.2.2   Synthesis of Bismuth Titanate Nanowires

In a typical experiment, predetermined amounts of titanium isopropoxide (TIP) and bismuth (III) acetate were quickly placed in the 10 mL view cell, followed by addition of acetic acid, and CO_2. The amount of bismuth (III) acetate was varied to prepare four different concentrations of bismuth titanate, with bismuth loadings of about 1, 2, 2.5, and 7 atomic %, hereafter referred as Bi1, Bi2, Bi3, and Bi4. The view cell was heated to 60 °C and subsequently pressurized to 5000 psig. A magnetic stirrer was used to ensure uniform mixing of the reactants. The hydrolysis rate was controlled by adjusting metal precursors to acetic acid molar ratios in the range of 1:5-6. During the gelation stage, a light pink color was observed in about 30-40 minutes for bismuth doped titania before changing to white color the next day. After five days of aging, the samples were washed with 100 mL of $ScCO_2$ at a rate of 0.3 mL/min to remove unreacted materials and by-products, and to prevent collapse of the gel network. The prepared bismuth doped TiO_2 sol-gel was then calcined in air at 500 °C for 2 hours. The calcination temperature was selected based on the thermal gravimetric analysis (TGA) results (not shown) where bismuth doped catalysts showed removal of organic components at about 450 °C. Similarly, undoped titanium dioxide nanowires were prepared without the addition of bismuth (III) acetate.

6.2.3   Preparation of Photoanode

Bismuth titanate nanowires were mixed into a paste for coating on conductive glass. The paste was made by dissolving ethyl cellulose into ethanol and terpineol mixture (2:1, v/v), then stored in a sealed container to minimize the changes in viscosity due to solvent evaporation. Fluorine doped tin oxide (FTO) glass plates (15 ohms per sq. inch, Solaronix, Switzerland) were cleaned by detergent wash and sonication for 10 minutes for three times, rinsed with DI water, sonicated in acetone for 5 minutes, washed with isopropanol, and finally dried with nitrogen gas.

The photoanode was prepared by creating a mask template using packing tape with about 40 µm thickness on the conductive side of the FTO glass. The bismuth titanate nanowires paste mixture was applied by doctor-blading with a glass rod, which formulates the active layer of the photoanode. The template tape was lifted after 30 minutes to minimize cracking of the paste. For comparison, the same procedure was followed for TiO_2 (P25) and undoped titanium nanowires. The coated FTO glass was then calcined at 500 °C under air at a heating rate of 5 °C /min in a muffle furnace. The resulting films were cooled to 80 °C before immersed for overnight into a dye solution of 0.3 mM cis-di-isothio-cyanato-bis (2,2'-bipyridyl-4,4'-dicarboxylato) ruthenium (II) bis (tetrabutylammonium), also called N719 dye (Solaronix, Switzerland) in acetonitrile/tert-butyl alcohol (1:1, v/v) solution.

6.2.4   Assembling dye sensitized solar cells (DSSCs)

The solar cells were assembled by combining platinum coated glass as the counter electrode with the prepared photoanode mentioned above. Platinum electrode was washed with a detergent, then rinsed with DI water followed by acetone before regeneration at 350 ºC for 30 minutes prior to use. The two electrodes were kept at a distance using 50 µm thick Surlyn hot-melt gaskets. The cells were then laminated together by pressing them on a hotplate at 100 ºC. Iodine / tri-iodide (Iodolyte Z-100 from Solaronix) was used as the redox electrolyte, which was injected into the cell void by vacuum filling technique through a predrilled hole at the back of the counter electrode. Finally the cell was sealed with hot-melt seal and a glass slide cover.

6.2.5   Characterization of Bismuth Titanate Nanowires

The synthesized nanowire morphology was characterized by scanning electron microscopy (SEM) (Model LEO 1530) and transmission electron microscopy (TEM) (Model JEOL 2010F) capable of dark field scanning transmission electron microscopy (STEM) and coupled with energy dispersive X-ray spectroscopy. For TEM analysis, the powdered samples were dispersed in ethanol by sonication for 15 min and then cast on a copper grid covered with holey carbon film. Samples for SEM imaging were prepared by applying the powder directly to a carbon adhesive tape. The BET (Brunauer-Emmett-

Teller) surface area and BJH (Barrett-Joyner-Halenda) pore size and volume analysis were determined from nitrogen adsorption and desorption isotherm data obtained at 77 K with a constant-volume adsorption apparatus (Micromeritic Tristar II) using N_2 gas (99.995% pure; obtained from Praxair, Canada). The prepared samples were degassed at 150°C overnight before measurements. Structural analysis of the samples was performed using an X-ray powder diffractometer (Rigaku Miniflex XRD, Texas, U.S.A.), fitted with a rotating sample holder, a scintillation counter detector and a divergent beam utilizing a Cu K source of X-rays (= 1.5418 °A). The XPS analysis was carried out with a Kratos Axis Ultra spectrometer using a monochromatic Al K (alpha) source (15mA, 14kV). Photocurrent performance of the DSSCs was tested under Oriel solar simulator (92250A, AM 1.5 G) equipped with a 150 W Xe lamp and intensity of 100 mW/cm^2 measured by a Keithley 2420 programmable SourceMeter.

6.3 Results and Discussion

Bismuth titanate nanowires were successfully prepared by the $ScCO_2$ sol-gel process at different loadings of bismuth using bismuth (III) acetate in addition to undoped TiO_2 nanowires using the same methodology. The nanowires morphology was examined by SEM, with a typical result shown in Figure 6-1a for TiO_2 nanowires. The TEM image of bismuth titanate nanowires shown in Figure 6-1b demonstrates clear uniformity with a high aspect ratio. Figure 6-1c is a high TEM image magnification of selected tips showing the high porosity of these nanowires.
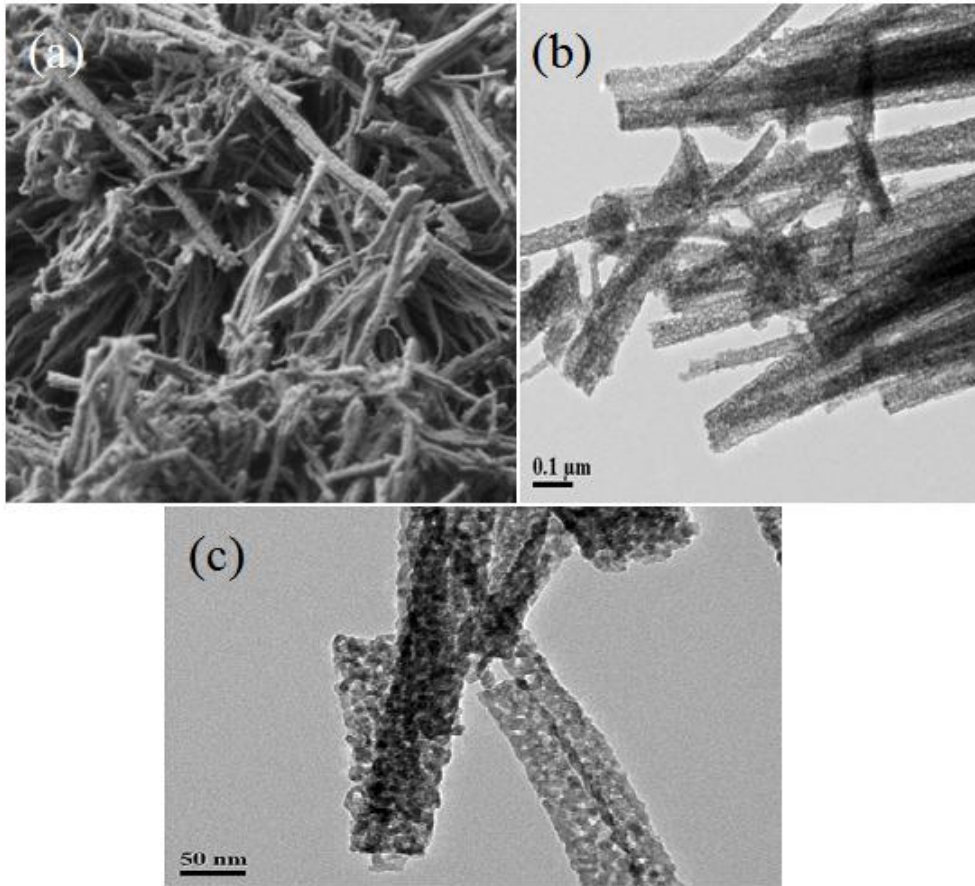
Figure 6-1: SEM images of TiO_2 nanowires (a), and TEM images of single nanowire (b), High resolution TEM of (c).

The selectivity of producing bismuth titanate nanowires or TiO_2 nanowires over nanoparticles is dictated by the alkoxide to acetic acid ratio. Nanowires can be produced with alkoxide to acetic acid ratios 4.5 according to earlier research conducted in our group.[20]

To illustrate the degree of metal dopant dispersion throughout the nanowires, TEM mapping using energy dispersive X-ray spectroscopy (EDS) is shown for the bismuth titanate nanowires in Figure 6-2. The nanowires show uniform dispersion of bismuth metal throughout the nanowires, with a bismuth loading of 1, 2, and 2.5 atomic %. This excellent dispersion of bismuth throughout the nanowires is attributed to the synthesis methodology using $ScCO_2$ as a solvent and drying agent. Sc-CO_2 will enhance the

precursors' solubility, preventing the collapse of formed networks during the gelation stage due to the zero surface tension of ScCO$_2$ during the aging and washing stages as described in detail previously.[20]
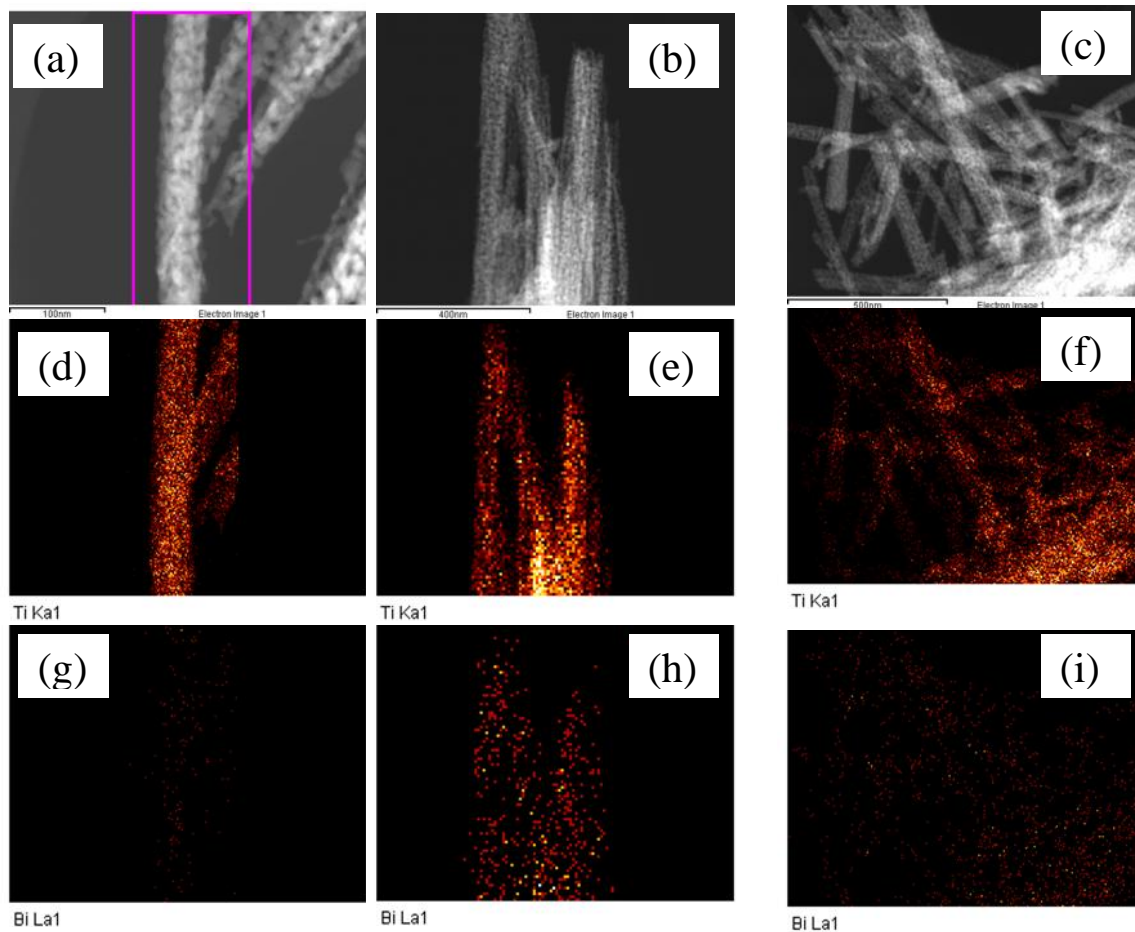
Figure 6-2: STEM image of bismuth titanate nanowires showing porosity of nanowire. EDS mapping shows the dispersion of titanium and bismuth within a nanowire.

The BET surface areas of the prepared bismuth titanate nanowires Bi1, Bi2, Bi3, and Bi4 were measured as 80, 85, 84 and 99 m^2/g, respectively. It is known that the surface area increases as a material's dimensionality increases. For example, nanoparticles have higher surface areas compared to nanorods and nanowires.[21, 22] Despite the formation of nanowires, the produced undoped TiO$_2$ nanowires had comparable surface areas to Degussa P25 nanoparticles (also examined in this work) which we measured as 58 and 50

m^2/g, respectively. The relatively high surface area of the bismuth doped nanowires can be attributed to pores formation during their sol-gel synthesis retaining the pores by scCO$_2$ drying as shown by the dark field STEM images in Figure 6-2.

 The XRD patterns of the bismuth titanate nanowires were compared with XRD spectra of the anatase TiO$_2$ phase with characteristic peaks at 25^0, 38^0, 48^0, 53^0, 55^0, 63^0, 70^0 and 76^0 shown in Figure 6-3a, which are an excellent match to anatase (PDF 01-086-1157). X-Ray diffraction of bismuth titanate showed broad peaks in addition to the anatase peaks with 2 = 27^0 and 30^0, and 36^0 which increased as the bismuth doping level increased as shown in Figure 6-3b. A shift to a lower angle of the anatase peak of 2 = 25.5^0 was observed with bismuth doping, which is in line with reported literature. Due to the larger ionic radius of Bi^{3+} (0.103 nm) compared to Ti^{4+} (0.061 nm), it replaces the Ti ions in the nanostructure. However, as the bismuth level increased only a slight shift to a higher angle is observed as shown in Figure 6-3c. This can be attributed to the increased amount of bismuth. One characteristic bismuth peak is around 27^0, corresponding to the plane [012] of rombohedral bismuth. In addition, a gradual change of intensity ratio between peaks at 54^0 and 55^0 occurs, with these two peaks merging into one peak at 54.5^0, as more bismuth is added into the nanowires. This was also the case for peaks at 68.9^0 and 70.4^0 as shown in Figure 6-3d. Moreover, no change was observed for peaks at 48^0 and 62^0 except a drop in intensity of the peak at 48^0 compared to peak at 54.5^0,which is in agreement with literature.[23]
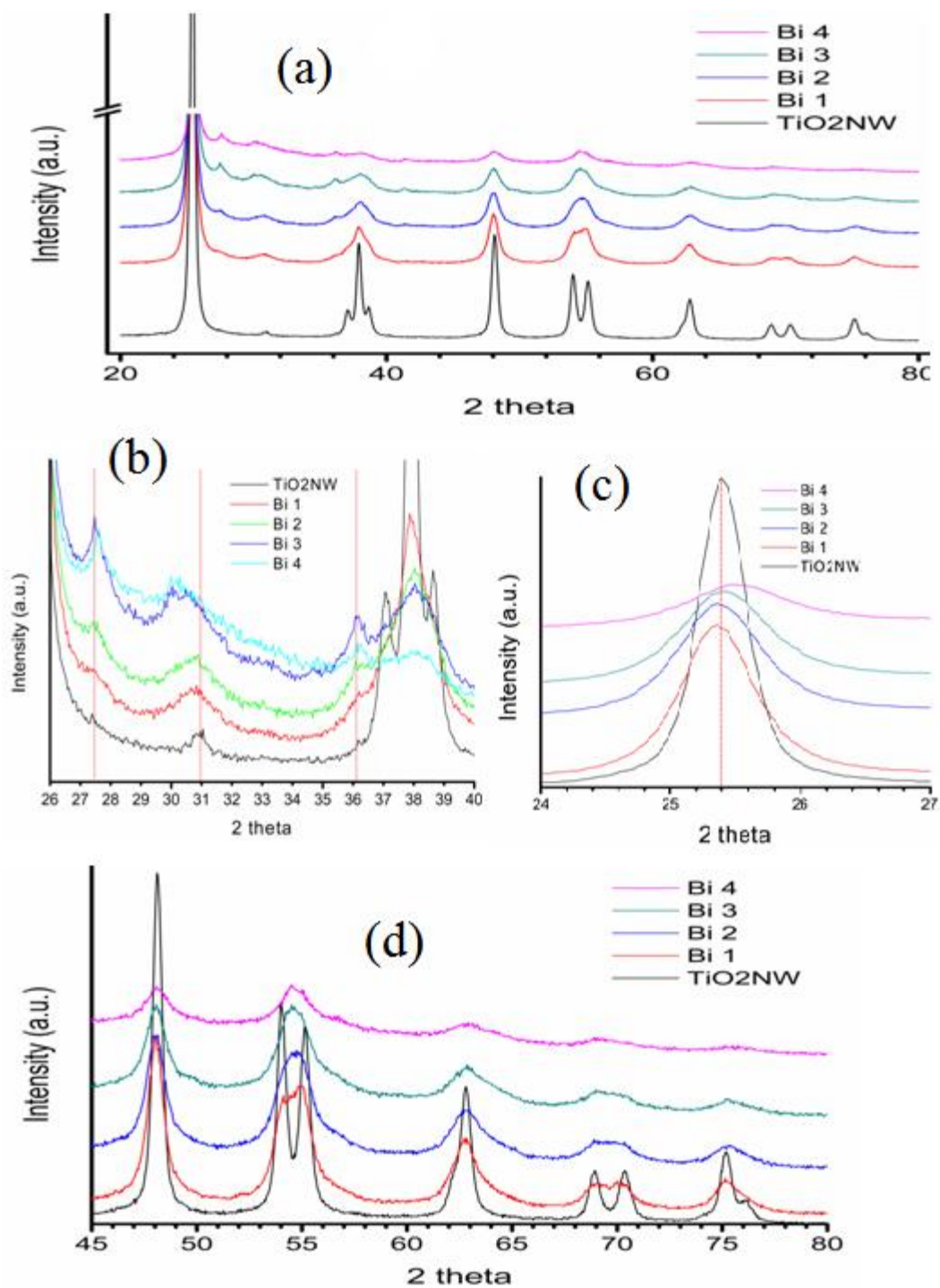
Figure 6-3: XRD results of titanium dioxide nanowires, bismuth titanate nanowires (a) XRD overview (b, c, and d) selected ranges of magnification.

Both the chemical oxidation states of bismuth and titanium elements and their concentrations within the nanowires were determined by XPS analysis. In all the prepared bismuth titanate nanowires, the chemical state of titanium is (IV) with a binding energy peak at 458.85 eV, depending on its interaction with the dopant metal as shown in Figure 6-4. The XPS analysis showed a characteristic binding energy peak of Bi 4f 7/2 at 159.46 eV, which indicates the existence of Bi (III).
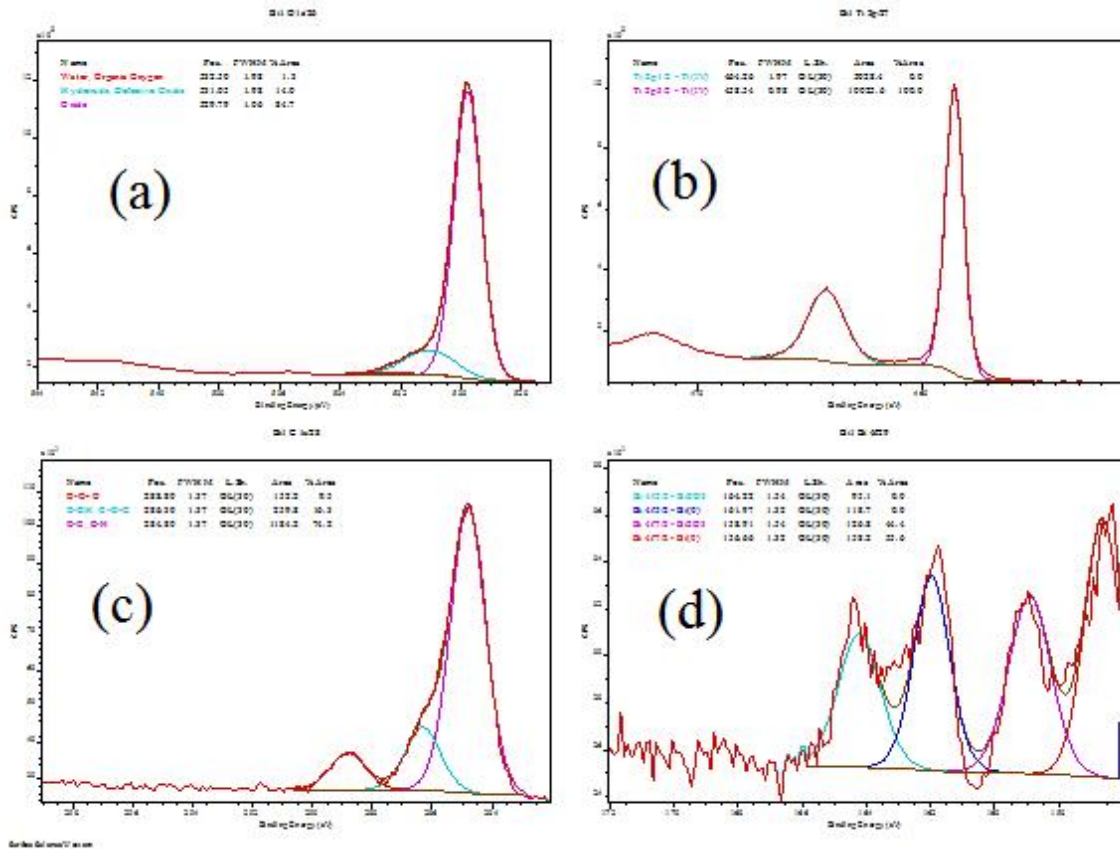
Figure 6-4: XPS results of bismuth titanate nanowire high resolution scan for the following elements (a) oxygen (b) Titanium (c) carbon (d) bismuth.

6.3.1   Photocurrent measurements

To evaluate the effectiveness of this synthesis method to produce highly dispersed bismuth dopant, its effect on DSSC's photocurrent density- voltage (J-V) curves were measured for P25 TiO_2, undoped TiO_2 nanowires, and bismuth titanate nanowires Bi1,

Bi2, Bi3 and Bi4 as shown in Figure 6-5. The open-circuit voltages (Voc) for P25 TiO_2 and sample Bi1 are comparable with values of 0.70 and 0.71 V, respectively. However, the undoped TiO_2 nanowires showed a lower Voc value of 0.63 V with the rest of the dye sensitized solar cells measured as 0.67,0.67,0.65 V for Bi2, Bi3, and Bi4, respectively. Although Voc is an indication of the chemical potential of the cell, which is a function of the nanocrystalline materials at the photoanode with respect to the chemical potential of the redox electrolyte, the voltage at zero short circuit current (V_{max}) is used to evaluate the DSSC overall electrical efficiency. The V_{oc} for all the cells were comparable except for the best performing ones are P25 and Bi1 as shown in Table 6-1.

The cell efficiency ( ) was calculated using the equation below:

$$ =Jsc*Voc \; X \; FF \; / \; I \qquad\qquad \textbf{6-1} $$

where, Jsc is the short current density (mA/cm^2), the maximum cell voltage is Vmax (volt), Fill factor (FF) and I represents the incident light intensity (mW/cm^2). It is clear from these results that bismuth doping increased the efficiency compared to the undoped TiO_2 NW by 7.5 times. This tremendous improvement can be attributed to bismuth doping at 1.4 atomic % for sample Bi1 had 8 times less series resistance than the undoped titanium nanowires and has about 5.5 times the photocurrent density. However, as bismuth doping increased, the Rs resistance also increased while the photocurrent dropped, which negatively impacted the cell performance. The total power produced in a dye sensitized cell is a critical factor, which reflects the total electrochemical productivity of each cell. Similar results can be observed for cell power, which are shown in Figure 6-6. The Bi1 and P25 TiO_2 showed the highest cell powers while the TiO_2 NW is the lowest. Power generation behaved in the same manner as photocurrent, with increasing concentration of bismuth the power output decreased.

Table 6-1: Photoelectric performance parameters for P25 TiO$_2$, undoped TiO$_2$ nanowires, and bismuth titanate nanowires Bi1, Bi2 , Bi3 and Bi4 and irradiation of 100 mW/cm^2.

Sample	Voc (V)	Jsc(mA/cm^2)	V$_{max}$(V)	Fill Factor (%)	(%)	Rs ( )	Rsh ( )
P25	0.70	2.23	0.57	70	1.09	50	20473
TiO$_2$ NW	0.63	0.59	0.50	57	0.21	724	27411
Bi 1 (1.4 %)	0.71	3.22	0.56	69	1.58	90	24338
Bi 2 (2.5 %)	0.67	1.37	0.52	64	0.59	261	26374
Bi 3 (5 %)	0.67	1.08	0.50	62	0.45	357	30032
Bi 4 (7 %)	0.65	0.71	0.49	61	0.28	535	33409
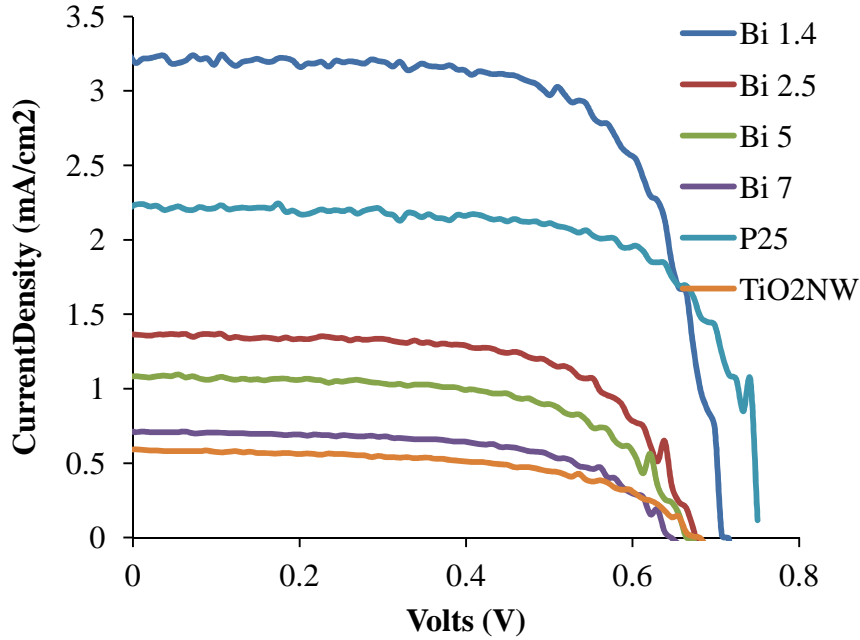
Figure 6-5: Photocurrent density- voltage (J-V) curves for P25 TiO_2, undoped TiO_2 nanowires, and bismuth titanate nanowires Bi1, Bi2 , Bi3 and Bi4 at irradiation of 100 mW/cm^2.
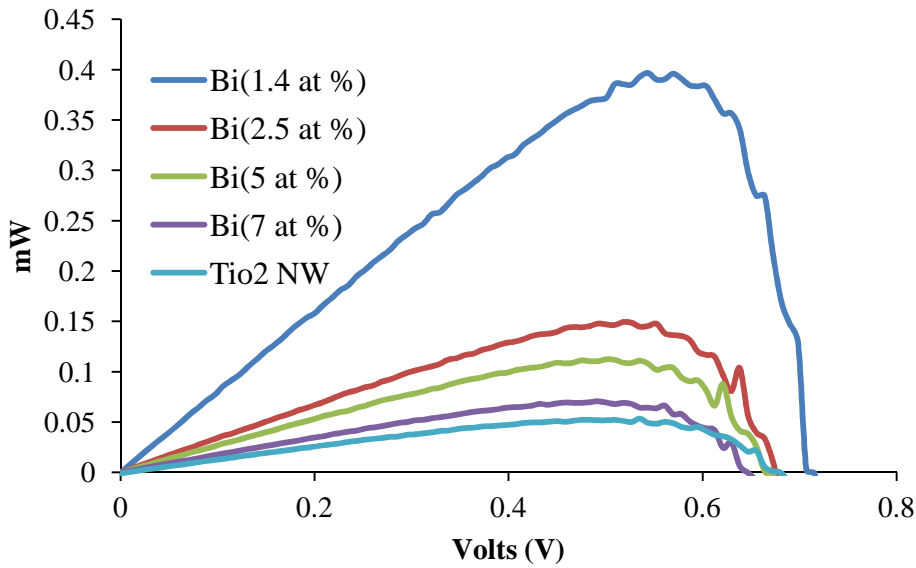
Figure 6-6: Power curves for undoped TiO_2 nanowires, and bismuth titanate nanowires Bi1, Bi2 , Bi3 and Bi4 and irradiation of 100 mW/cm^2.

6.3.2   Electrochemical Impedance Spectroscopy Analysis

Internal evaluation of dye sensitized solar cells is critical as it deepens our understanding of the competing processes that occur within our novel nanowire photoanode materials. The knowledge of the kinetics of the photoelectrochemical processes is critical for determining the limitations and evaluating proposed enhancement approaches. A well established method is electrochemical impedance spectroscopy (EIS), which can provide detailed knowledge of these competing reactions.[24] Charge transfer resistance is a limiting factor for the dye sensitized solar cell. Two interfaces in DSSCs where this can take place, namely, charge transfer resistance at the Pt/electrolyte interface and at the bismuth titanate (nanocrystalline material)/dye/ electrolyte interface, are referred to as R_{Pt} and R_{ct}, respectively.

EIS spectra of bismuth titanate nanowires, shown in Figure 6-7, were collected using 200 mV AC, -0.5 DC V, and signal frequency 0.1 to 1 x 10^5 Hz, while the cell was under 1 sun illumination at 100 mW/cm^2. Two semicircles were observed at low levels of bismuth doping in sample Bi1. The smaller semicircle was at a high frequency region with corresponding information about the Pt/electrolyte interface resistance R_{Pt}. The second circle was at the middle frequency region, corresponding to bismuth titanate nanowires/dye/electrolyte interface resistance R_{ct}. However, no semicircle was observed at low frequency which indicated insignificant electron diffusion limitation within the electrolyte. [25] The drop in DSSCs efficiency with increasing bismuth doping concentration can be explained by the EIS spectra results. The increase in charge transfer of DSSCs Bi1, Bi2, Bi3, and Bi4 was observed in the EIS spectra as the magnitude of these semicircles increased in Figure 6-7. These EIS results are in a good agreement with the decreasing efficiency and increased resistance values Rs at open circuit conditions of the corresponding DSSCs. The increased efficiency of Bi1 DSSC compared to undoped TiO$_2$ nanowires DSSC prepared using the same synthesis method is attributed to the reduced recombination rate and enhanced light harvesting efficiency, and lower Rs resistance value of 90   for Bi1 compared to 724   for TiO$_2$ NW. However, as the bismuth doping concentration increased, charge transfer within the solar cells also increased. The disappearance of the small semicircle at low frequency's corresponding to

R_{Pt} in samples Bi2, Bi3 and Bi4 is attributed to the fact that R_{ct} being the predominant resistance for these dye sensitized solar cells.
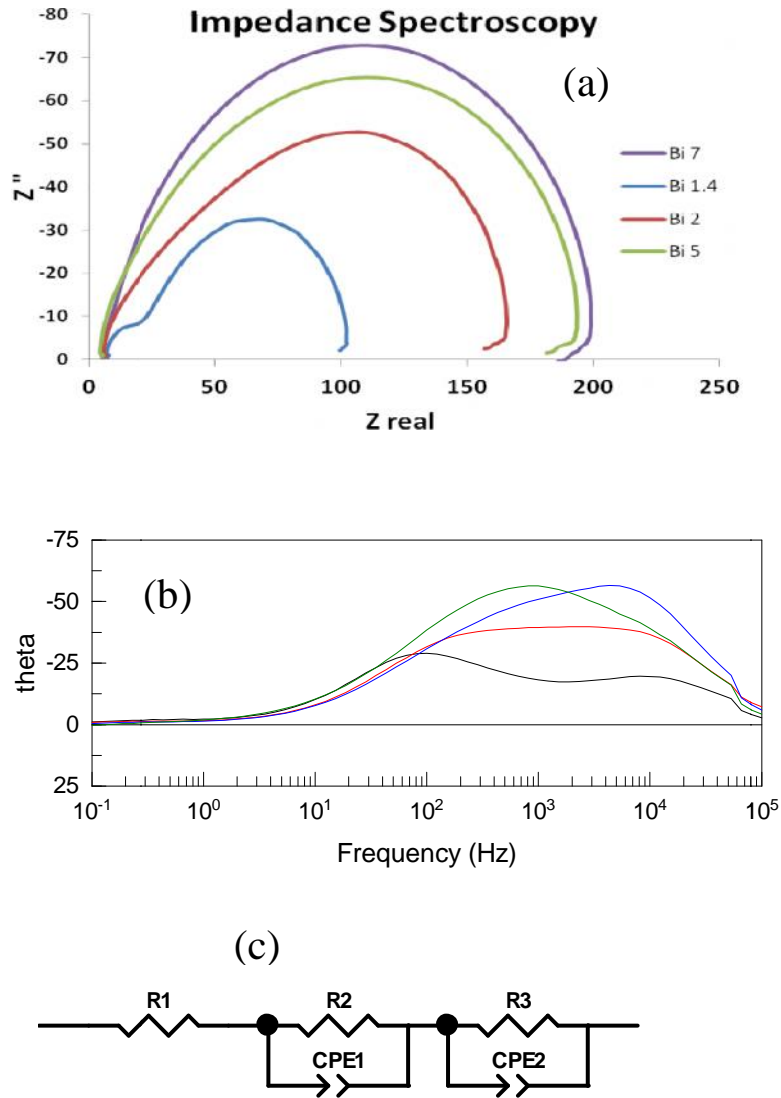
Figure 6-7: Nyquist plot (a) and the Bode plots (b) measured with EIS analyzer for the DSSCs of bismuth titanate nanowires, and (c) equivalent circuit.

Fitting the electrochemical impedance spectra to an equivalent circuit enables determination of each internal resistance of these DSSCs. The equivalent electrical model consists of resistors that are connected in series with parallel capacitors to reflect chemical capacitance at different interfaces as shown in Figure 6-7c. In this model R1, R2 and R3 represents series resistance, resistance at the counter electrode, and resistance at the photoanode, respectively. CPE1 and CPE2 represent the chemical capacitance at

the counter electrode/electrolyte and the photoanode (nanocrystalline /dye/electrolyte), respectively. The resistance and chemical capacitance results were calculated from the spectra using Z-view software with typical results summarized along with the efficiency of each DSSC presented in Table 6-2.

Table 6-2: Typical EIS parameters calculated by fitting the data to equivalent circuit for P25 TiO$_2$, undoped TiO$_2$ nanowires, and bismuth titanate nanowires Bi1, Bi2 , Bi3 and Bi4.

Sample	R1	R2	R3	Efficiency (%)	Rs ( )	Rsh ( )
P25	4.67	15.16	120	1.09	50	20473
TiO$_2$ NW	4.15	7.98	202	0.21	724	27411
Bi 1 (1.4 %)	6.67	7.30	52.4	1.58	90	24338
Bi 2 (2.5 %)	4.99	12.40	115	0.59	261	26374
Bi 3 (5 %)	4.50	21.29	167	0.45	357	30032
Bi 4 (7 %)	4.42	0.61	202	0.28	535	33409

EIS results are in agreement with the J-V measurements, which showed that bismuth doping improved the DSSC efficiency in general compared to undoped TiO$_2$ NW and dropped as bismuth doping increased. EIS showed that R1 which is the sheet resistance did not change much, except for sample Bi1. However, the resistance at the counter electrode was affected by the bismuth titanate doping and the transition of morphology from nanoparticles as in P25 to nanowires. The most critical resistance is the photoanode resistance (R3), which showed bismuth doping at 1.4 % caused 4 times less resistance compared to undoped titanium nanowires. This lower resistance enhances electron flow reducing the chances for recombination to take place. This resistance also increased as a function of bismuth concentration; having comparable resistance to the undoped titanium dioxide at 7% bismuth doped titanium nanowires.

Electron lifetimes in DSSCs is a critical parameter that greatly influences its performance. The photogenerated electrons with longer lifetime can be more effectively transported through the active nanocrystalline phase to FTO glass, then to the counter electrode to reduce the electrolyte and help in regeneration of the dye; thereby completing their cycle lifetime and generating power. Shorter life-time electrons are due to recombination with dye or electrolyte negatively affecting the DSSC performance. Electron lifetimes can be calculated from the middle peak of the Nyquist plot using a characteristic frequency (ω_{max}) with the following equation 6-2.

$$\tau_e = 1/\omega_{max} \qquad\qquad 6\text{-}2$$

The shift of the peak frequency of the middle semicircle to a lower frequency is an indication of a longer electron life-time, as easily seen in the Bode-phase plot shown in Figure 6-7b. Doping with bismuth at the lowest (Bi1) level showed the longest electron lifetime of 3.7 ms, followed by both P25 and Bi2 with 2.4 ms, 1.6 ms and 2.0 ms for Bi3 and Bi4, respectively. In addition, we noticed that pristine TiO_2 NW's showed a lower electron lifetime compared to P25.

Table 6-3: Electron lifetime P25 TiO_2, undoped TiO_2 nanowires, and bismuth titanate nanowires Bi1, Bi2 , Bi3 and Bi4.

Sample	τ_e (ms)	ω_{max} (Hz)	Efficiency (%)
P25	2.4	413.4	1.09
TiO_2 NW	1.6	628.3	0.21
Bi 1 (1.4 %)	3.7	272.0	1.58
Bi 2 (2.5 %)	2.4	413.4	0.59
Bi 3 (5 %)	1.6	628.3	0.45
Bi 4 (7 %)	2.0	509.6	0.28

6.4   Conclusions

Bismuth titanate nanowires with high aspect ratios and various loadings of Bi were successfully synthesized using sol-gel in $ScCO_2$, a green solvent. The performance of the produced bismuth doped nanowires for dye sensitized solar cell application was evaluated. A bismuth doping level of 1.4 mol % was found as the most effective in reduction of recombination of electron compared to pristine TiO_2 nanowires and P25 nanoparticles. The electron life time of 1.4 mol % Bi-titanate nanowire, P25 nanoparticles, and pristine TiO_2 nanowires was 3.7 ms, 2.4 ms, and 1.6 ms, respectively, with corresponding solar cell efficiency of 1.58%, 1.09%, and 0.21%. In addition, bismuth enhanced charge transfer at low levels of doping. It was also noticed that bismuth doping at 2.5 mol % showed lower charge resistance of 115   compared to P25 at 120   and TiO_2 NW at 202   . These improvements are attributed to better bismuth dispersion while having a high surface area. These were found to improve electron transport due to lower resistance within the bismuth titanate layers, and reduced recombination time as shown by the electron lifetime. Doping of titanium dioxide with less expensive transition metals such as bismuth is a promising choice for enhancing the dye sensitized solar cell performance compared to pristine TiO_2. The nanowires provided a direct transport pathway which improved electron collection of photogenerated electrons.

6.5 References

1. Chong, M.N., B. Jin, C.W. Chow, and C. Saint, *Recent developments in photocatalytic water treatment technology: a review.* Water Res, 2010. **44**(10): p. 2997-3027.

2. Linsebigler, A.L., G.Q. Lu, and J.T. Yates, *Photocatalysis on Tio2 Surfaces - Principles, Mechanisms, and Selected Results.* Chemical Reviews, 1995. **95**(3): p. 735-758.

3. Anpo, M. and M. Takeuchi, *The design and development of highly reactive titanium oxide photocatalysts operating under visible light irradiation.* Journal of Catalysis, 2003. **216**(1-2): p. 505-516.

4. Mahlambi, M.M., A.K. Mishra, S.B. Mishra, R.W. Krause, B.B. Mamba, and A.M. Raichur, *Metal doped nanosized titania used for the photocatalytic degradation of rhodamine B dye under visible-light.* J Nanosci Nanotechnol, 2013. **13**(7): p. 4934-4942.

5. Kim, S., S.J. Hwang, and W. Choi, *Visible light active platinum-ion-doped TiO2 photocatalyst.* J Phys Chem B, 2005. **109**(51): p. 24260-24267.

6. Jia, Y.S., S. Shen, D.G. Wang, X. Wang, J.Y. Shi, F.X. Zhang, H.X. Han, and C. Li, *Composite Sr2TiO4/SrTiO3(La,Cr) heterojunction based photocatalyst for hydrogen production under visible light irradiation.* Journal of Materials Chemistry A, 2013. **1**(27): p. 7905-7912.

7. Solis-Casados, D.A., L. Escobar-Alarcon, A. Arrieta-Castaneda, and E. Haro-Poniatowski, *Bismuth-titanium oxide nanopowders prepared by sol-gel method for photocatalytic applications.* Materials Chemistry and Physics, 2016. **172**: p. 11-19.

8. Ismail, A.A. and D.W. Bahnemann, *Efficient Mesoporous Semiconductor Materials for Environmental Applications*, in *Environmental Photochemistry Part III*. 2015, Springer. p. 221-266.

9. Shang, J., W.C. Hao, X.J. Lv, T.M. Wang, X.L. Wang, Y. Du, S.X. Dou, T.F. Xie, D.J. Wang, and J.O. Wang, *Bismuth Oxybromide with Reasonable Photocatalytic Reduction Activity under Visible Light.* ACS Catalysis, 2014. **4**(3): p. 954-961.

10. Wang, L., W. Ma, Y. Fang, Y. Zhang, M. Jia, R. Li, and Y. Huang, *Bi 4 Ti 3 O 12 Synthesized by High Temperature Solid Phase Method and it's Visible Catalytic Activity.* Procedia Environmental Sciences, 2013. **18**: p. 547-558.

11. Yao, W.F., X.H. Xu, H. Wang, J.T. Zhou, X.N. Yang, Y. Zhang, S.X. Shang, and B.B. Huang, *Photocatalytic property of perovskite bismuth titanate.* Applied Catalysis B-Environmental, 2004. **52**(2): p. 109-116.

12. Hu, D., X. Kong, K. Mori, Y. Tanaka, K. Shinagawa, and Q. Feng, *Ferroelectric mesocrystals of bismuth sodium titanate: formation mechanism, nanostructure, and application to piezoelectric materials.* Inorg Chem, 2013. **52**(18): p. 10542-10551.

13. Nogueira, A.E., E. Longo, E.R. Leite, and E.R. Camargo, *Synthesis and photocatalytic properties of bismuth titanate with different structures via oxidant peroxo method (OPM).* J Colloid Interface Sci, 2014. **415**: p. 89-94.

14. Moula, G., M. Mumin, and P. Charpentier, *Enhancement of Photocurrent in Dye-Sensitized Solar Cells Using Bismuth Doped TiO2-Graphene as a Hot Carrier Transport. J Nanomater Mol Nanotechnol S1: 002.* of, 2013. **6**: p. 30-33.

15. De Silva, R.C.L., V. Perera, and L. Liyanage, *Study of charge transport and carrier lifetime in dye-sensitized solar cells made from gold particles embedded SnO2 films.* 2015.

16. Yu, C., X. Meng, X. Song, S. Liang, Q. Dong, G. Wang, C. Hao, X. Yang, T. Ma, and P.M. Ajayan, *Graphene-mediated highly-dispersed MoS 2 nanosheets with enhanced triiodide reduction activity for dye-sensitized solar cells.* Carbon, 2016.

17. Farhangi, N., R.R. Chowdhury, Y. Medina-Gonzalez, M.B. Ray, and P.A. Charpentier, *Visible light active Fe doped TiO2 nanowires grown on graphene using supercritical CO2.* Applied Catalysis B-Environmental, 2011. **110**: p. 25-32.

18. Garcia-Gonzalez, C.A., M.C. Camino-Rey, M. Alnaief, C. Zetzl, and I. Smirnova, *Supercritical drying of aerogels using CO2: Effect of extraction time on the end material textural properties.* Journal of Supercritical Fluids, 2012. **66**: p. 297-306.

19. Lucky, R.A., Y. Medina-Gonzalez, and P.A. Charpentier, *Zr doping on one-dimensional titania nanomaterials synthesized in supercritical carbon dioxide.* Langmuir, 2010. **26**(24): p. 19014-19021.

20. Sui, R., A. Rizkalla, and P.A. Charpentier, *Experimental study on the morphology and porosity of TiO2 aerogels synthesized in supercritical carbon dioxide.* Microporous and Mesoporous Materials, 2011. **142**(2-3): p. 688-695.

21. You, M., T.G. Kim, and Y.-M. Sung, *Synthesis of Cu-Doped TiO2Nanorods with Various Aspect Ratios and Dopant Concentrations.* Crystal Growth & Design, 2010. **10**(2): p. 983-987.

22. Susha, A.S., A.A. Lutich, C. Liu, H. Xu, R. Zhang, Y. Zhong, K.S. Wong, S. Yang, and A.L. Rogach, *Comparative optical study of colloidal anatase titania nanorods and atomically thin wires.* Nanoscale, 2013. **5**(4): p. 1465-1469.

23. Pei, L.Z., H.D. Liu, N. Lin, and H.Y. Yu, *Bismuth titanate nanorods and their visible light photocatalytic properties.* Journal of Alloys and Compounds, 2015. **622**: p. 254-261.

24. Kim, J.H., K.P. Kim, D.H. Kim, and D.K. Hwang, *Electrospun ZnO Nanofibers as a Photoelectrode in Dye-Sensitized Solar Cells.* J Nanosci Nanotechnol, 2015. **15**(3): p. 2346-2350.

25. Zheng, D.J., M.D. Ye, X.R. Wen, N. Zhang, and C.J. Lin, *Electrochemical methods for the characterization and interfacial study of dye-sensitized solar cell.* Science Bulletin, 2015. **60**(9): p. 850-863.

Chapter 7

7 Synthesis of polysulfone membrane materials for photocatalytic membrane reactor

7.1 Introduction

Limited and contaminated water resources are a serious current problem that the world is facing. Challenges of both high and oscillating energy costs, reuse of contaminated water, efficiency of water treatment and emerging pollutants such as endocrine disruptors are global concerns.[1] In both developed and developing countries, reliable low cost water treatment technologies are required for sustainability. In addition to supplying treated water for use in municipalities, natural disasters such as earthquakes and flooding create additional need for economical, efficient and portable water treatment technologies that can also be used in remote areas.

In many parts of the world, sea water is a source of relatively clean water except for the high salinity content. Desalination of sea water is often used for producing potable water in many coastal cities, especially in middle-eastern countries. [2] Many traditional methods for desalination, especially thermally driven ones such as multiple effect distillation, multi stage flash, vapor compression distillation, have shown their limited cost efficiency compared to membrane based processes such as reverse osmosis and nanofiltration. According to General Des Eaux and US Filter, the world wide desalination market is estimated to be $70 billion by 2020. [3]

Membrane technology offers many advantages over the conventional thermal methods for desalination, although the application of membrane technology faces the major challenge of fouling.[4] Fouling causes deterioration of the membrane performance characterized by declining flux and water permeability by reversible or irreversible blockage of membrane pores from the fouling materials such as natural organic matter, extra cellular polymeric substances and microbial cells. In order to overcome membrane fouling, various approaches have been taken including developing new membrane materials or membrane cleaning processes using mechanical means such as the

application of shear. The current methods to reduce membrane fouling focus on enhancing their hydrophilicity to reduce deposition of the hydrophobic fouling component. [5-7] Based on this approach, several studies have been conducted to improve the hydrophilicity of polymeric membranes by surface modification, bulk modification, and the addition of inorganic nanostructured fillers such as zeolites, titanium, aluminum oxide and zirconium oxide nanoparticles. [8-14] Hybrid materials that combine both the flexibility of the polymer component and the strength of the inorganic component provide a new promising route to next generation membrane materials. These well-ordered nanostructured materials provide a promising route for developing next-generation photocatalytic membrane materials that could reduce fouling and reduce cost of operation.

New nanostructured membrane materials are required to deal with emerging pollutants such as endocrine disrupting hormones, while complying with stringent drinking water qualities such as the new limits for boron in seawater desalination. [15-17] The challenge in preparing these next-generation hybrid membranes is to synthesize these materials with a well defined structure while uniformly dispersing the inorganic component throughout the polymer membrane. Here the challenges include the dispersion of the inorganic component, forming well aligned nanostructures, controlling the pore size and distribution while reducing any aggregation of nanoparticles. [18] Current approaches in nanotechnology are extremely expensive involving multi-step synthetic approaches that are difficult to scale up. However recent advances in nanoscience, using one pot-synthetic technique with supercritical fluids, provide a new low cost scalable route to prepare these materials.

 Organic-inorganic hybrid membranes which combine the advantages of conventional polymeric membranes used in water treatment, with the advantages of the latest development of inorganic nanomaterials are useful for such application. Titanium dioxide (TiO_2) at the nanostructure level can be utilized as the inorganic component of the proposed hybrid. The various nanostructures will include TiO_2 nanoparticles, nanowires or nanotubes with a chemical linkage to the polymer backbone rather than physical entrapping within the polymer. It is expected that introducing inorganic nanomaterials

will improve the membrane's physical and chemical characteristics such as enhanced mechanical strength, operating temperature and ability to reduce fouling. [19, 20] Synthesizing polymeric membranes with predesigned specific sites (-COOH, OH) to coordinate TiO_2 is critical for development of this dual functional membranes. Monomers with carboxylic and hydroxyl functional groups will be utilized for subsequent step-growth polymerization of the desired polymers.

There are many types of polymers to synthesize membranes with variable chemical and physical properties driven by the target application. Polyethersulfone (PES) is widely used as an organic membrane due to its advantages such as high thermal stability and mechanical strength over other types of polymers. However, it suffers high fouling rates and low permeability due to its low hydrophilicity. Lee et al. (2007) conducted a series of experiments to study the relationship between hydrophobicity and fouling by natural organic matter. [6] Fouling by organic matter is strongly observed with hydrophobic membranes compared to hydrophilic ones. It is widely accepted that improving hydrophilicity will reflect positively on membrane flux and reduce adsorption of fouling materials to the membrane surface.[21] By copolymerization with hydrophilic compounds, improvements were made to enhance membrane resistance to fouling through improving hydrophilicity. [7, 22, 23]

The addition of inorganic nanoparticles such as titanium dioxide (TiO_2), a semiconductor photocatalyst, has been examined to enhance permeability and antifouling due to unique photocatalytic properties.[24] Most current methods involve physical entrapping of TiO_2 in the membrane by physical blending during the casting stage or deposition on the surface of the membrane. These approaches result in membranes with lower performance compared to membranes that have chemical bonding of TiO_2 to the polymer part of the membrane.[25] The benefits of such approach were demonstrated by polyamide membranes with carboxylic acid groups and functionalized with TiO_2 nanoparticles. These membranes showed photo-bactericidal effect on E-coli during UV light illumination and possessed self cleaning properties. [26-28]

One of the most challenging aspects of current nanotechnology is how to synthesize a well defined nanostructured material with accuracy and low cost. These two concerns drive the most current research on the synthesis of nanostructured materials. Significant success has been achieved in synthesizing inorganic and metallic nanostructure materials such as nanoparticles, nanotubes, nanorods, nanofibers, nanopillar, nanowires, and nanosheets in recent years. [29-34] The template approach was utilized successfully for nanofabrication of cylindrical polystyrene-block-poly (ethylene oxide) (PS-b-PEO) copolymers. [35] They utilized anodic aluminum oxide (AAO) membranes with pore diameters in the range of 150-400 nm, and a thickness of 60 µm purchased from Whatman. The membrane was placed on top of 5% diluted PS-b-PEO solution which was placed on top of a glass slide. Membrane pores were wetted with polymer solution by capillary forces. Filled membrane was kept at room temperature to allow slow room temperature evaporation of solvent (benzene) and subsequent vacuum drying for complete removal of the solvent. PS-b-PEO nanotubes were obtained by removal of the membrane template using a 5% wt sodium hydroxide solution for about 20 minutes. In this research polysulfone polymers were prepared to be modified into nanotubes, functionalize with photocatalyst using available carboxylic and hydroxlyic groups on the polymer backbone. These polymers were selected based on available functional groups and with rigid backbone provided by aromatic rings compared to traditional membrane such as polyether sulfone.

7.2   Experimental details

7.2.1   Chemicals and Materials

4,4-bis(4-hydroxyphenyl) valeric acid, bis(4-chlorophenyl) sulfone, 4,4-bis(4-hydroxyphenyl) valeric acid, 2-[Bis(4-hydroxyphenyl)methyl]benzoic acid, terephthaloyl chloride, Sodium Hydroxide, toluene (HPLC grade), N-Methyl-2-pyrrolidone (NMP), P25, and bisphenol A, hydrochloric acid (37%), anhydrous tetrahydrofuran (THF, 99.9%), potassium carbonate (K_2CO_3) was dried in vacuum over overnight at 60 ºC to remove moisture. All chemicals were purchased from Sigma-Aldrich Canada and used as received, except for potassium carbonate. Anodic aluminum membrane (AAO), Anodisc 47 was purchased from Whatman.

7.2.2   Characterization

Scanning electron microscopy images were collected using a Leo (Zeiss) 1540XB SEM. Imaging was performed at either low voltage (1 kV) for morphology or at 10 kV for backscatter imaging. Samples were coated with osmium metal in a Filgen OPC80T. Attenuated total reflection-Fourier transform infrared (ATR-FTIR) spectra were measured using a Nicolet 6700 FTIR spectrometer (Thermo Scientific) equipped with a smart iTR (diamond ATR). The spectra were recorded in the range of 600-4000 cm^{-1} with a resolution of 4 cm^{-1} over 32 scans. Thermogravimetric analysis (TGA) was performed using a TA Q500 TGA at a heating rate of 10 ℃/min under an inert (nitrogen) atmosphere. The molecular weight and PDIs of produced polyether sulfone polymers were measured by gel permeation chromatography (GPC) with a Viscotek instrument using triple detectors (RI, LS, and V) referenced to PS standards (1 ml/min, at 30 ℃).

7.2.3   Results and discussions

Different starting materials to be reacted with bis (4-chlorophenlyl) sulfone were selected to synthesize a novel polymer that has specific functional groups such as -COOH groups to enable coordination with TiO_2 nanoparticles. Condensation copolymerization approach was utilized due to its ability for design of specific backbone of polymer and functional groups from condensation reactions of starting monomers bearing target functional groups.

7.2.4   Synthesis of Polysulfone using 4,4-bis(4-hydroxyphenyl) valeric acid

4,4-bis(4-hydroxyphenyl) valeric acid and bis (4-chlorophenyl) sulfone were used to synthesize polymer containing -COOH groups. In a typical procedure, 5.08 g of 4,4-bis (4-hydroxyphenyl) valeric acid was dissolved into 30 ml NMP, 20 ml of toluene, 5.1 g of bis(4-chlorophenyl) sulfone, and 6g of potassium carbonate was dried in a vacuum oven were added into a 3 neck flask. The mixture was heated to about 120°C after the addition of toluene to remove water by azeotropic distillation under inert gas (N_2) and continuous mixing. The mixture was cooled to room temperature and bis (4-chlorophenyl) sulfone was added. The mixture was heated gradually to 170°C for about 24 hours. The reaction

produced a viscous material which was diluted with 3:1 tetrahydrofuran (THF) and hydrochloric acid (HCl) mixture to remove inorganic salt. Polycondensate was precipitated into water; the filtrate was re-dissolved into THF then precipitated again into methanol. The product was dried for 24 hours under reduced pressure at 60°C. The reaction scheme is shown in Figure 7-1. From GPC measurements (with polystyrene standard) it was shown that the average molecular weight (Mw) of the produced polymer was 10674 Da. with polydispersity (Mw/Mn) of 1.544. GPC detail results are shown in Table 7-1. The FTIR measurement in Figure 7-2 shows comparative spectra of the starting materials and the produced polymer. Observed bands at 1095-1030 cm^{-1} are in the stretching vibrations range of O=S=O. Vibration in range of 1715-1685 cm^{-1} and 1628-1622 cm^{-1} are typical of C=O of carboxylic acid groups and C=C respectively. While, weak stretching in 3070-3010 cm^{-1} and 1590-1480 cm^{-1} can be assigned to C-H and aromatic ring vibrations, respectively. Titanium dioxide nanoparticles of 21 nm size was used to functionalize 4,4'-Bis(4-hydroxyphenyl) valeric acid using by refluxing it in isopropanol solution for 12 hours. The resulted functionalized monomer FTIR spectra was compared to its produced polymer showing reduced carboxylic acid stretching at 3300 cm^{-1} and 1715 cm^{-1} ranges in Figure 7-3.

Figure 7-1: A reaction scheme of polycondensation of 4.4'-bis(4-hydroxyphenyl) valeric acid and bis(4-chlorophenyl) sulfone.
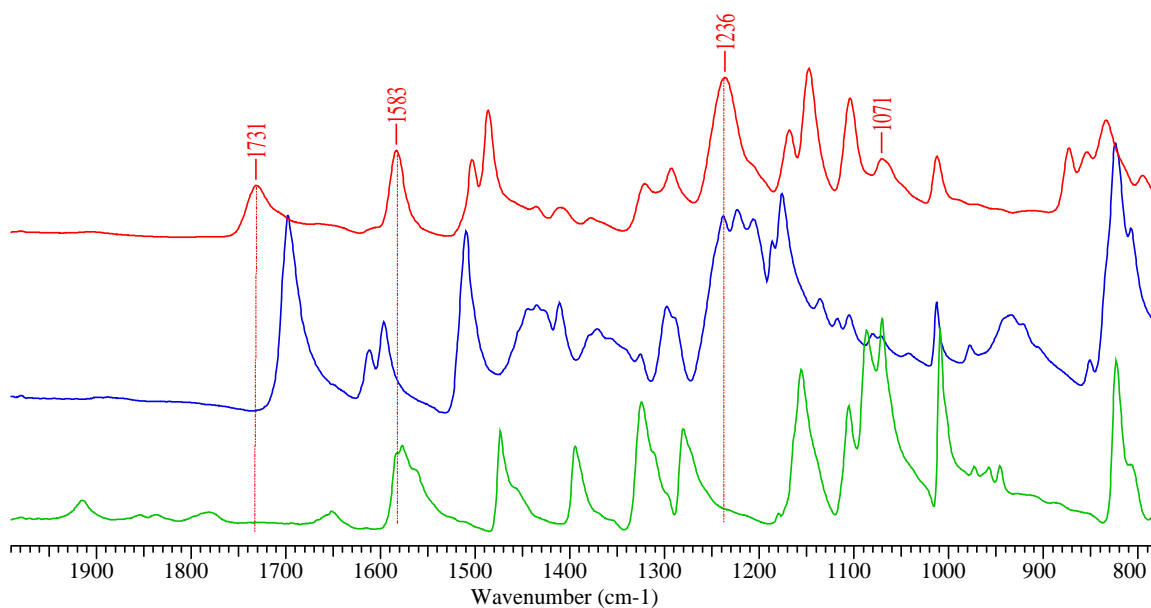
Figure 7-2: FTIR spectra of starting materials Bis(4-chlorophenyl) sulfone (blue), 4,4' Bis(4-hydroxyphenyl) valeric acid (green) and produced polymer (red).
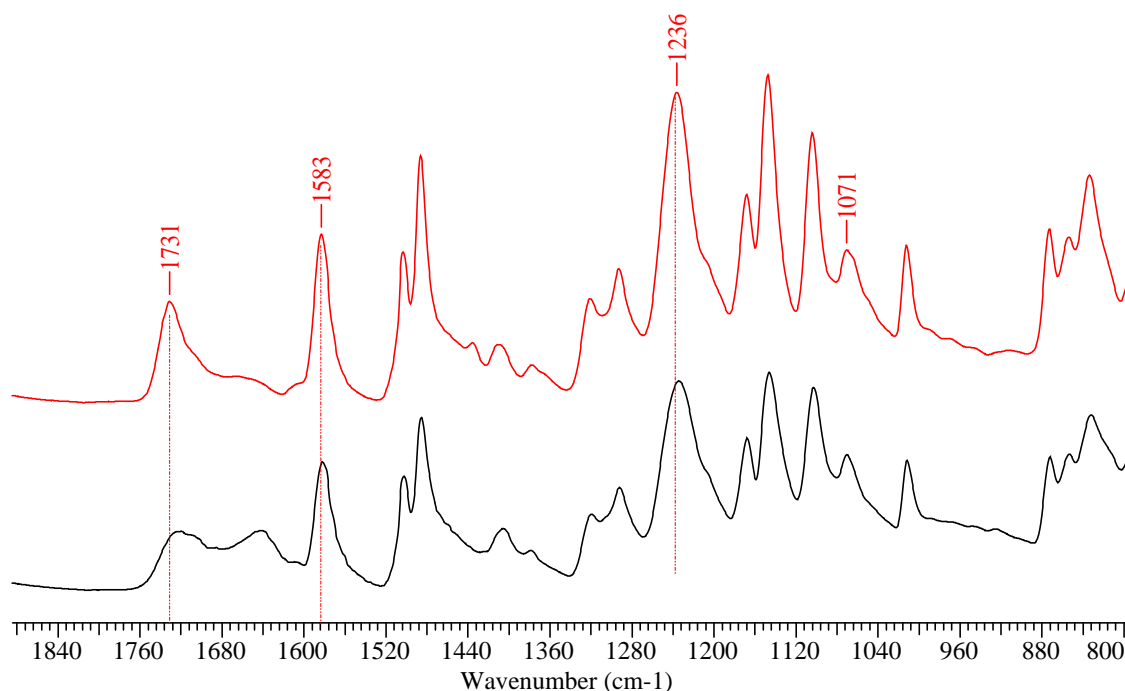
Figure 7-3: FTIR spectra of produced polymer formed from Bis (4-chlorophenyl) sulfone with 4,4' Bis (4-hydroxyphenyl) valeric acid (red) and TiO_2 of 21nm functionalized 4,4' Bis(4-hydroxyphenyl) valeric acid (black).

Table 7-1 : GPC Analysis Results for bis (4-chlorophenyl) sulfone polymerizing with 4,4'-bis(4-hydroxyphenyl) valeric acid.

Parameter	Value
Peak RV	15.78 (ml)
Weight-average Molecular Number (Mn)	10764 Daltons
Number -average Molecular Weight (Mw)	16620 Daltons
Z-average molecular weight (Mz)	24117 Daltons
Peak molecular weight (Mp)	16199 Daltons
Polydispersity Pd (Mw/Mn)	1.544

7.2.5 Synthesis of polysulfone using 2-[Bis(4-hydroxyphenyl)methyl]benzoic acid (Phenolphthalin)

Following a similar procedure as mentioned above, 6.3 mmoles of 2-[Bis(4-hydroxyphenyl)methyl]benzoic acid dissolved in 30 ml NMP, 14.5 mmoles of potassium carbonate, and 20 ml toluene were added into a 3 neck flask. The mixture was then heated to 120°C to remove water by azeotropic distillation under inert gas and continuous mixing for 4 hours. The mixture was then cooled to room temperature and 6.3 mmoles of bis(4-chlorophenyl) sulfone were added. The mixture was heated gradually to 170°C then the temperature was fixed for about 24 hours. The reaction produced a viscous material which was diluted with 3:1 tetrahydrofuran (THF) and hydrochloric acid (HCl) mixture to remove the inorganic salt. The produced polymer was precipitated into water; the filtrate was re-dissolved into THF, andthen was re-precipitated into methanol. The product was dried for 2 days under reduced pressure at 60°C. GPC analysis was carried out by dissolving 3 mg/l of produced polymer in THF to determine the degree of polymerization. The reaction scheme is shown in Figure 7-4. The produced polymer showed three times the molecular weight (36730 Da) and with less polydispersion index (1.276) than the polymer prepared with 4,4'-Bis(4-hydroxyphenyl) valeric acid as shown in Table 7-2. The FTIR showed a typical C=O at 1713 cm^{-1}, ring medium stretching at 1583-1486 cm^{-1}, O=S=O at 1070 cm^{-1}, and C-O-C in the range of 1293-1230 cm^{-1} as shown in Figure 7-5. While functionalized monomer with TiO2 nanoparticles spectra is shown in Figure 7-6 compared to produced polymer and the monomer after calcination at 500 ºC.
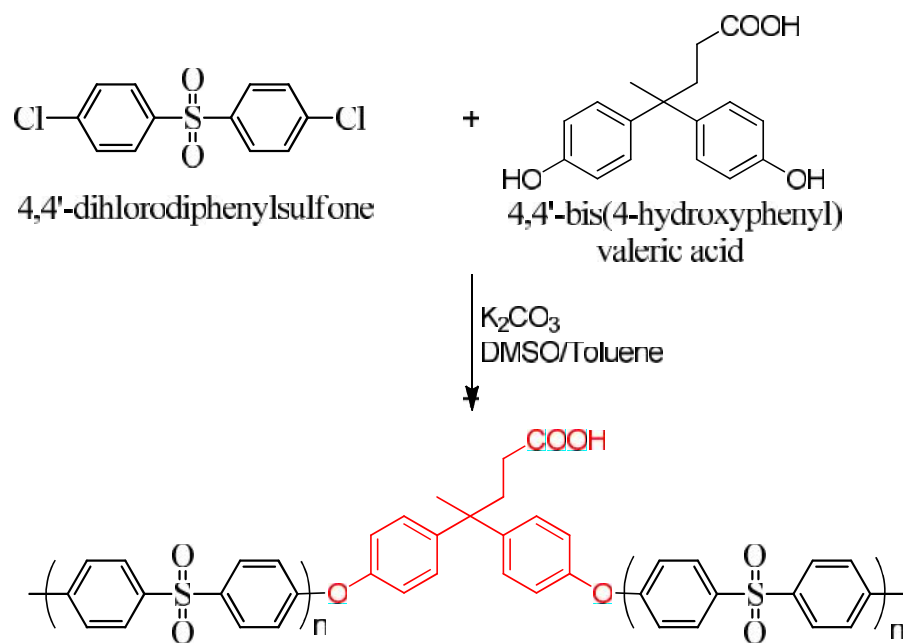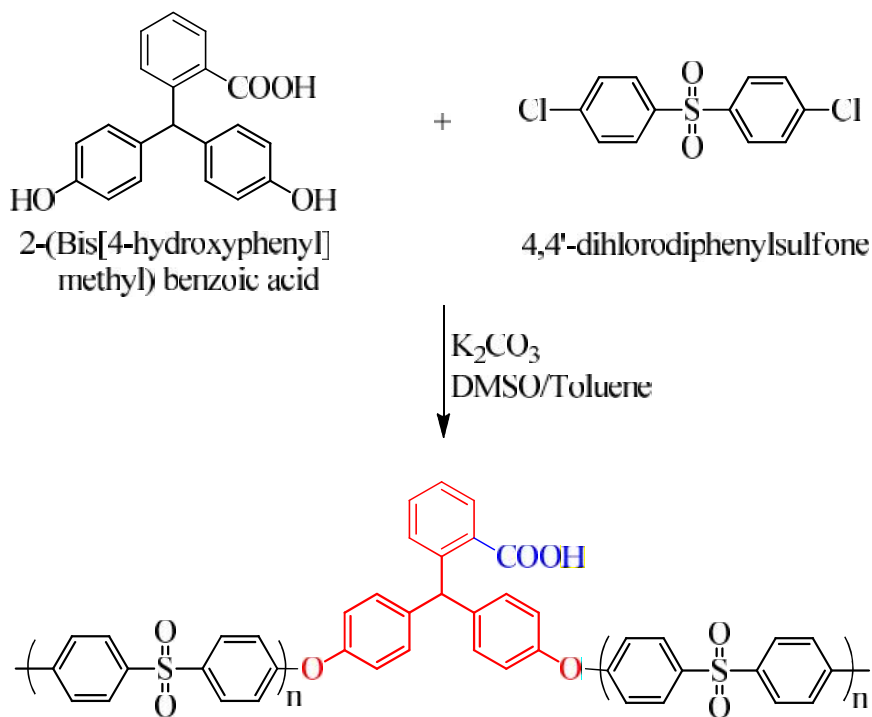
Figure 7-4: A reaction scheme of polycondensation of 2-[Bis(4-hydroxyphenyl)methyl]benzoic acid and bis(4-chlorophenyl) sulfone.

Figure 7-5: FTIR spectra of starting materials Bis(4-chlorophenyl) sulfone (black), 2-[Bis(4-hydroxyphenyl)methyl] benzoic acid (blue) and their produced polymer by condensation reaction (red).
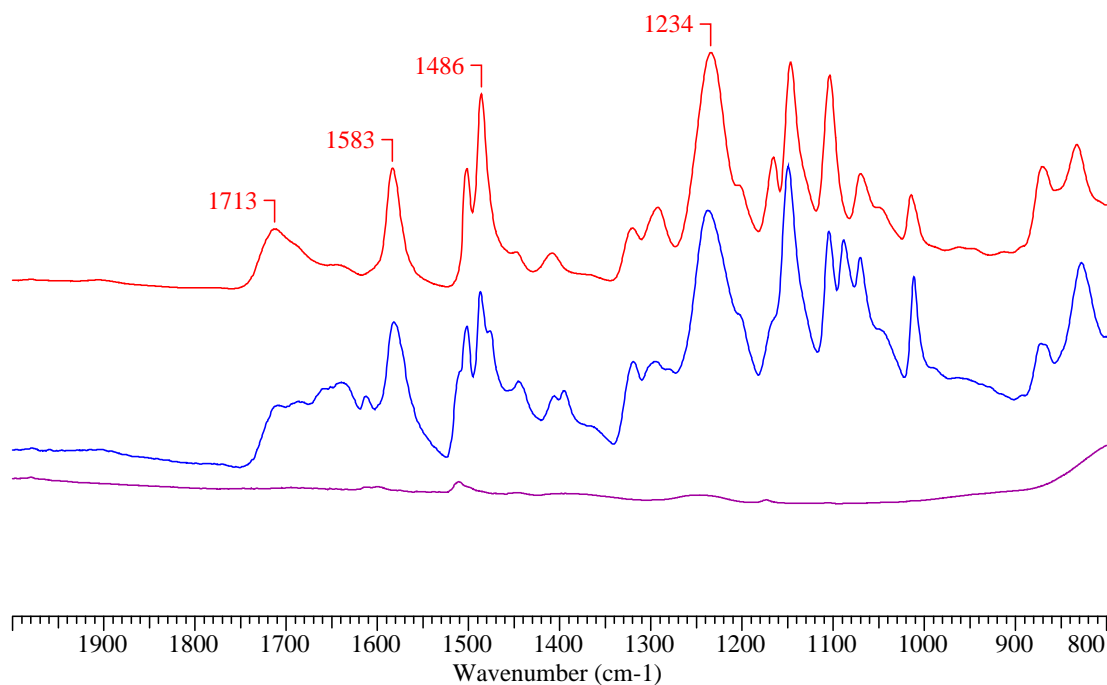
Figure 7-6: FTIR spectra of formed from of Bis(4-chlorophenyl) sulfone with 2-[Bis(4-hydroxyphenyl)methyl] benzoic acid (red), TiO$_2$ functionalized 2-[Bis(4-hydroxyphenyl)methyl] benzoic acid (blue) and calcined at 500 ºC (purple).

Table 7-2: GPC Analysis Results for produced polysulfone polymer by reacting bis(4-chlorophenyl) sulfone with 2-[Bis(4-hydroxyphenyl) methyl] benzoic acid.

Parameter	Value
Peak RV	15.00 (ml)
Weight-average Molecular Number (Mn)	36730 Daltons
Number -average Molecular Weight (Mw)	46855 Daltons
Z-average molecular weight (Mz)	55681 Daltons
Peak molecular weight (Mp)	54179 Daltons
Polydispersity Pd (Mw/Mn)	1.276

7.2.6 Synthesis of polysulfone using mixture of 4,4'-Bis(4-hydroxyphenyl) valeric acid and 2-[Bis(4-hydroxyphenyl)methyl]benzoic acid

A mixed carboxylic acid bearing groups was introduced into polysulfone polymer by reacting a mixture of 10 mmoles of 4,4'-Bis(4-hydroxyphenyl) valeric acid and 5 mmoles of 2-[Bis(4-hydroxyphenyl)methyl]benzoic acid dissolved in 60 ml NMP and 40 ml toluene. The reaction was catalyzed by adding 32 mmoles of potassium carbonate, and was carried in a 200 ml three-neck flask. The mixture was then heated to 120°C to remove water by azeotropic distillation under inert gas and continuous mixing for 4 hours. The mixture was then cooled to room temperature and 15 mmoles of bis (4-chlorophenyl) sulfone were added. The reaction scheme is shown in Figure 7-7. The mixture was heated gradually to 170°C, and the temperature was kept constant for about 24 hours. The reaction produced a viscous material which was diluted with 3:1 tetrahydrofuran (THF) and hydrochloric acid (HCl) mixture to remove inorganic salt. The produced polymer was precipitated into water; the filtrate was re-dissolved into THF followed by re-precipitation of methanol. The product was dried for 2 days under reduced pressure at 60°C. GPC analysis was used to determine produced polymer molecular weight (Mw=4526 Da) and showed that under these reaction conditions, wide range molecular distributions was obtained by having a polydispersion value of 2.5 as shown in Table 7-3. Figure 7-8 shows the C=O vibration peak in the produced polymer shifted to lower value o 1583 cm^{-1} and the rest of peaks were observed within the expected values discussed above.

Figure 7-7: Reaction schematic of Bis(4-chlorophenyl) sulfone, with 2-[Bis(4-hydroxyphenyl)methyl] benzoic acid, and 4,4'-Bis(4-hydroxyphenyl) valeric acid.
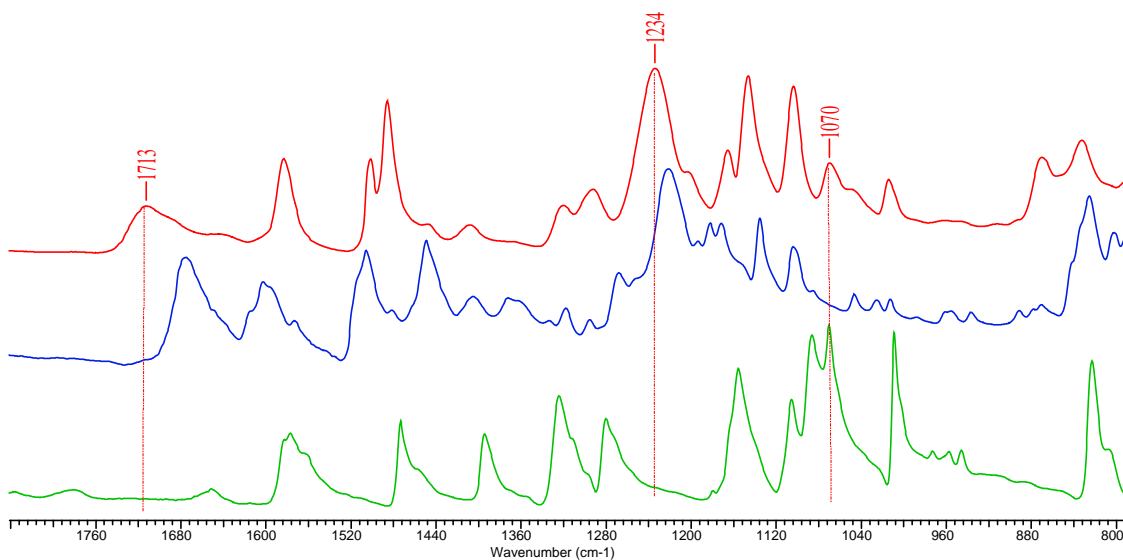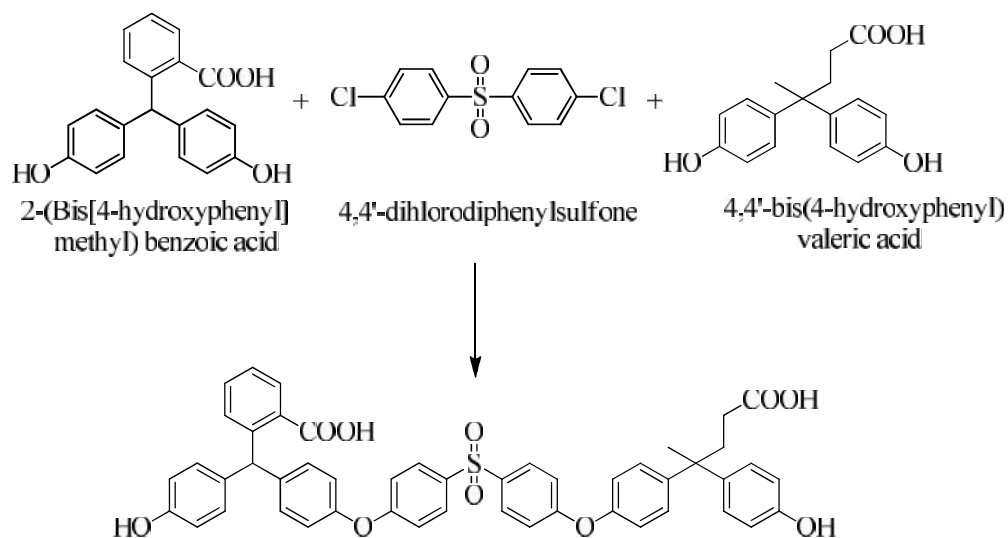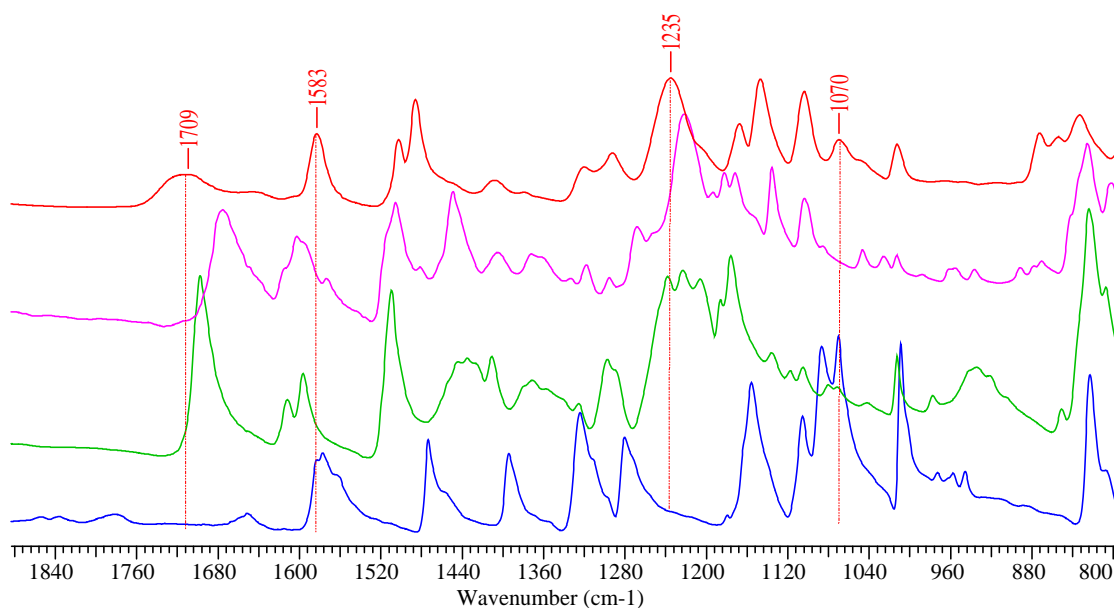

Figure 7-8: FTIR spectra of starting materials Bis(4-chlorophenyl) sulfone (blue), 2-[Bis(4-hydroxyphenyl)methyl] benzoic acid (pink), 4,4'-Bis(4-hydroxyphenyl) valeric acid (green) and their produced polymer (red).

Table 7-3: GPC Analysis Results for mixed polysulfone prepared by reacting bis(4-chlorophenyl) sulfone with 2-[Bis(4-hydroxyphenyl) methyl] benzoic acid and 4,4'-Bis(4-hydroxyphenyl) valeric acid mixture.

Parameter	Value
Peak RV	19.400 (ml)
Weight-average Molecular Number (Mn)	4625 Daltons
Number -average Molecular Weight (Mw)	11897 Daltons
Z-average molecular weight (Mz)	28169 Daltons
Peak molecular weight (Mp)	3376 Daltons
Polydispersity Pd (Mw/Mn)	2.572

7.2.7   Synthesis of polysulfone using Terephthaloyl Chloride , bis(4-chlorophenyl)sulfone, and 4.4'-bis(4-hydroxyphenyl) valeric acid

This approach was used to strengthen the backbone of the polysulfone polymer while still controlling the amount of carboxylic group of the final polymer. Terephthaloyl chloride was used to introduce more aromatics with carboxylic group and reactivity for condensation polymerization with hydroxyl groups. Typical condensation synthesis procedure was carried out in a 200 ml three-necked flask, which was equipped with a refluxing dean-stark condenser to eliminate condensation by-products under constant nitrogen flow. The reaction mixture was 21 mmoles of 4,4'-Bis(4-hydroxyphenyl) valeric acid, 44 mmoles of potassium carbonate dissolved into a mixture of 60 ml NMP and 40 ml toluene. The mixture was then heated to 120°C to remove water by azeotropic distillation under inert gas and continuous mixing for 4 hours. The mixture was then cooled to room temperature and 10.5 mmoles of terephthaloyl chloride, and 10.5 mmoles bis(4-chlorophenyl) sulfone were added. The mixture was heated gradually to 170°C, keeping the temperature fixed for about 24 hours and the reaction scheme is shown in Figure 7-9. The produced viscous material was diluted with 3:1 tetrahydrofuran (THF)

and hydrochloric acid (HCl) mixture then was precipitated into water and filtered. The polymer then was re-dissolved into THF followed by reprecipitation in methanol and dried for 2 days under reduced pressure at 60°C. FTIR analysis for this polymer showed two different C=O stretching peaks at 1732, and 1709 cm^{-1} and stretching vibration of aromatic rings at 1661 cm^{-1} as shown in Figure 7-10. Wide range molecular weight distribution was also observed as the polydispersity value showed in Table 7-4.
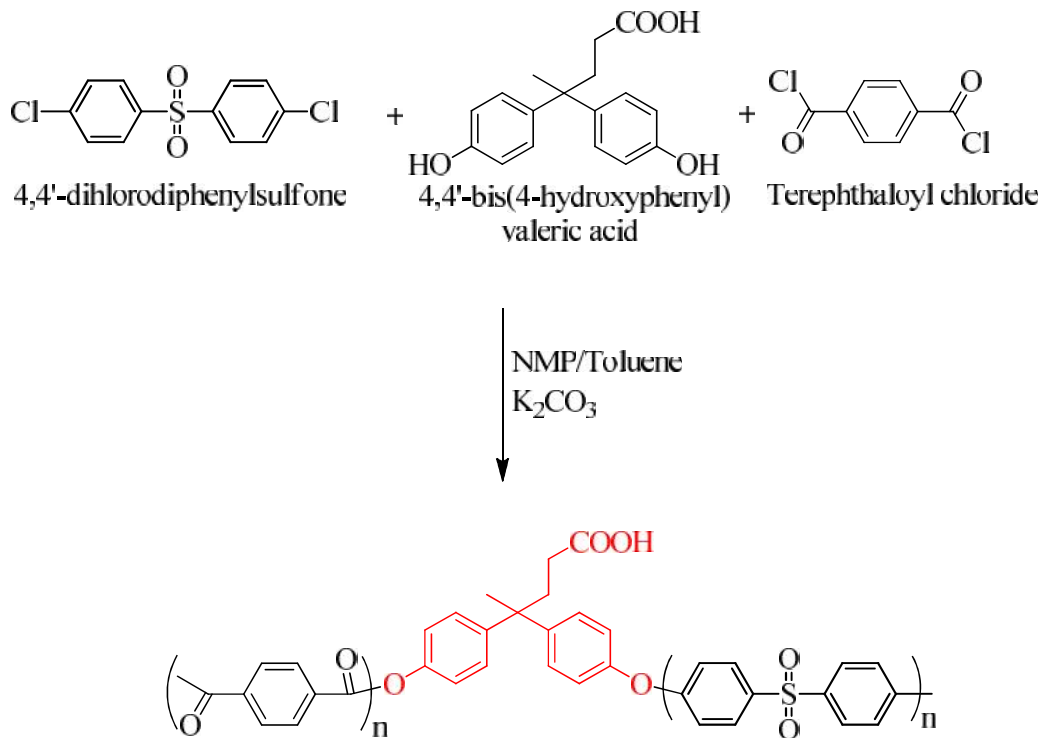
Figure 7-9: Reaction schematic of polysulfone by reacting terephthaloyl chloride, 4,4'-dichlorodiphenylsulfone and 4,4'-bis(4-hydroxyphenyl) valeric acid.
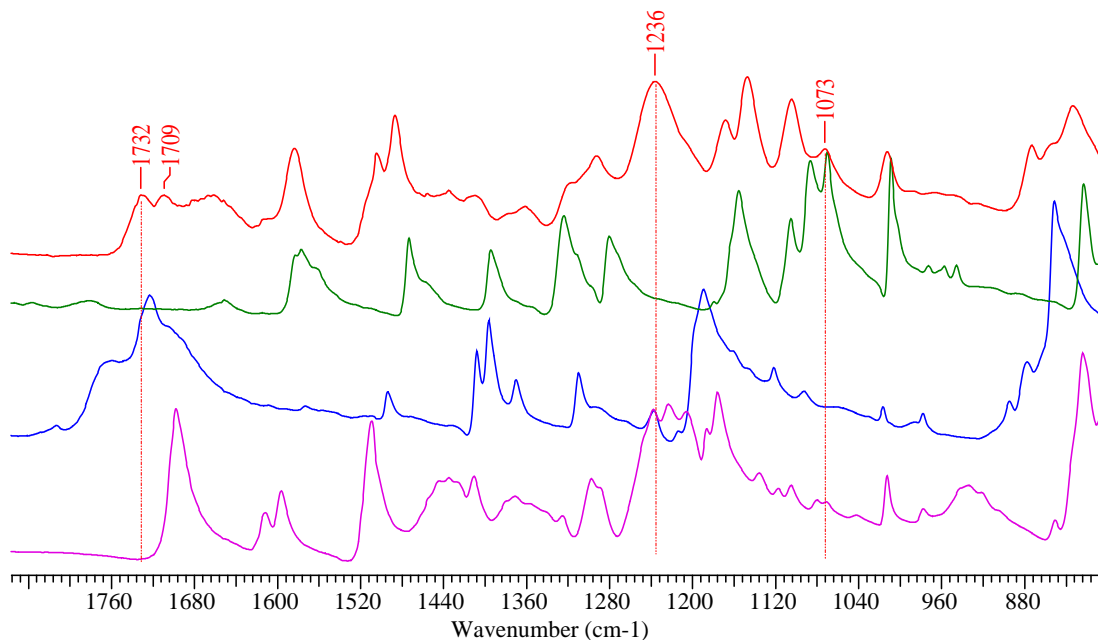
Figure 7-10: FTIR spectra of mixed produced polysulfone (red) prepared by reacting bis(4-chlorophenyl) sulfone (green), terephthaloyl chloride (blue), with 4,4'-Bis(4-hydroxyphenyl) valeric acid (pink).

Table 7-4: GPC Analysis Results of synthesized mixed polysulfone prepared by reacting terephthaloyl chloride, bis(4-chlorophenyl) sulfone with 4,4'-Bis(4-hydroxyphenyl) valeric acid.

Parameter	Value
Peak RV	18.693 (ml)
Weight-average Molecular Number (Mn)	3826 Daltons
Number -average Molecular Weight (Mw)	11526 Daltons
Z-average molecular weight (Mz)	194741 Daltons
Peak molecular weight (Mp)	2909 Daltons
Polydispersity Pd (Mw/Mn)	3.013

7.2.8   Preparation of polymeric Nanotubes

The synthesis of polymeric nanotubes was investigated to produce membrane that can be used for filtration and functionalized with TiO_2 for photoactive membrane. Initially, nanotubes of produced polysulfone were synthesized using the melt-wetting approach. Here, polysulfone pellets were heated to the polymer T_g and sandwiched between two glass slides to make a polymer film. Then anodic aluminum oxide (AAO) membrane template with an average pore size of 200 nm and thickness of about 60 μm (see Figure 7-11) was placed on top of the polymer. The polymer was introduced into the pore channels of the aluminum oxide membrane by capillary forces using two approaches. First approach was by using heated vacuum oven for about 24 hours. The second approach was by preparing 30 % polymer solution in a Petri dish and placed the AAO into it. Capillary forces draw the polymer solution into AAO template and coated the internal walls of the membrane. Removal of the aluminum oxide template was carried out using 5 % NaOH solution for about 15 minutes. The sample was then washed with deionized water several times. Figure 7-12 summarizes the different steps involved in the polymer nanotube synthesis using AAO template.

The resulting free standing nanotubes were prepared for examination by scanning electron microscope (SEM). The samples were prepared by a deposition of a thin layer of osmium nanoparticles using sputtering over the polymer surface to enhance conductivity while facilitating a high quality image. The SEM images showed an array of highly ordered nanotubes with density of the polysulfone nanotubes similar to the density of nonpores in the original AAO template with almost complete filling of all the nanopores with no or minimum deformation as shown in Figure 7-13. Furthermore, SEM image of a single nanotube provided more morphological information about its internal diameter of about 100 nm and tubes thickness of about 40 nm as shown in Figure 7-14.
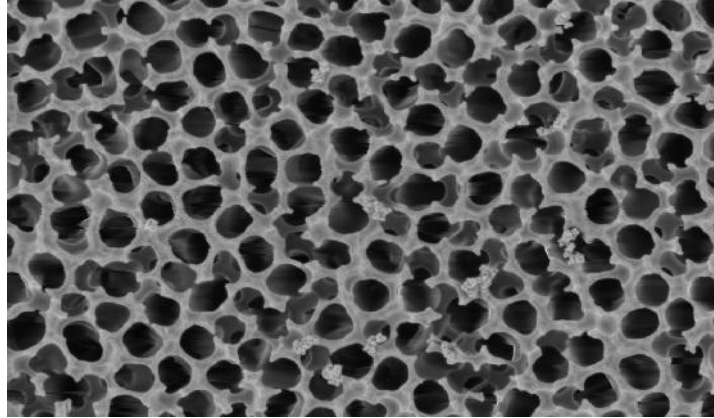
Figure 7-11: SEM image of Aluminum Oxide membrane coated with platinum nanoparticles part of imaging requirement.
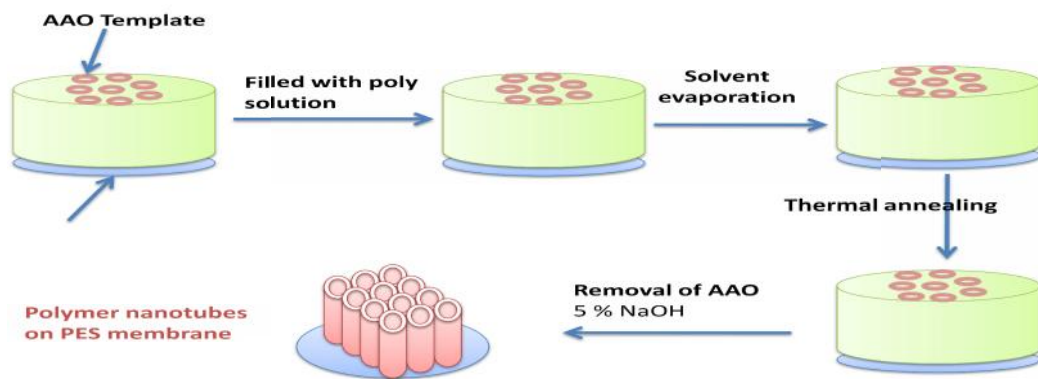
Figure 7-12: Aluminum oxide membrane template approach to prepare polymeric nanotubes.
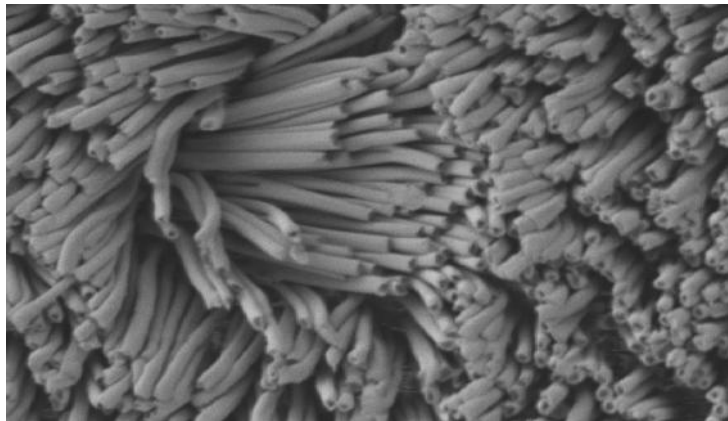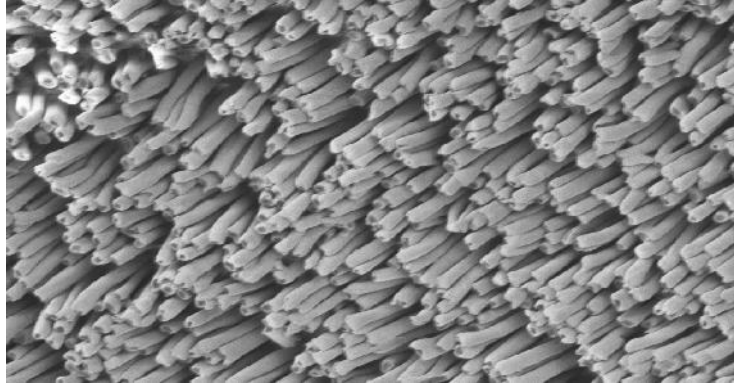
Figure 7-13: An overview of polysulfone nanotubes prepared by the template assisted method.
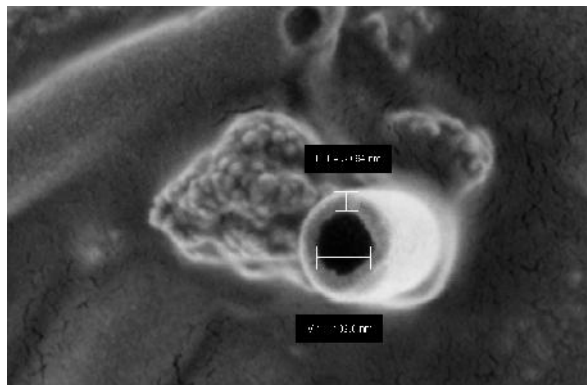
Figure 7-14: SEM of an individual polysulfone nanotubes showing opening of 100 nm and wall thickness of 50 nm. Scale on image is 100 nm.

7.3 Conclusions

Four novel polysulfone polymers were prepared using two different sulfonated reagents (bis(4-chlorophenyl)sulfone, and terephthaloyl chloride) and two reagents to introduce required carboxylic groups for TiO_2 coordination (4,4'-Bis(4-hydroxyphenyl) valeric acid and 2-[Bis(4-hydroxyphenyl)methyl]benzoic acid). Gel permeation chromatography (GPC) confirmed the polymerization by determining average molecular weight of all the produced polymers. In addition, successful synthesis of polymeric nanotubes using AAO template method using these produced polysulfone polymers with specific sites for titanium nanoparticles coordination, will pave the way for organic-inorganic hybrid membrane for photocatalytic membrane applications to degrade organic pollutants and reduce fouling on its surface. Polysulfone polymer produced by reacting 2-[Bis(4-hydroxyphenyl)methyl]benzoic acid with bis(4-chlorophenyl) sulfone would be the best of all the four produced polysulfone due to its higher molecular weight that would make it strong polymer can with stand high filtration pressure. Photocatalytic evaluation for membrane with functionalized TiO_2 or other suitable photocatalyst should be carried out in a reactor that enables both filtration and light irradiation.

7.4 References

1. Acero, J.L., F. Javier Benítez, F.J. Real, and E. Rodriguez, *Influence of membrane, pH and water matrix properties on the retention of emerging contaminants by ultrafiltration and nanofiltration.* Desalination and Water Treatment, 2015: p. 1-14.

2. Sowers, J., A. Vengosh, and E. Weinthal, *Climate change, water resources, and the politics of adaptation in the Middle East and North Africa.* Climatic Change, 2010: p. 1-29.

3. Matsuura, T., *Progress in membrane scince and technology for seawater desalination - A review.* Desalination, 2001. **134**(1-3): p. 47-54.

4. Yu, W., N.J. Graham, and G.D. Fowler, *Coagulation and oxidation for controlling ultrafiltration membrane fouling in drinking water treatment: Application of ozone at low dose in submerged membrane tank.* Water Res, 2016. **95**: p. 1-10.

5. Yu, C.H., C.H. Wu, C.H. Lin, C.H. Hsiao, and C.F. Lin, *Hydrophobicity and molecular weight of humic substances on ultrafiltration fouling and resistance.* Separation and Purification Technology, 2008. **64**(2): p. 206-212.

6. Lee, S. and C.H. Lee, *Effect of membrane properties and pretreatment on flux and NOM rejection in surface water nanofiltration.* Separation and Purification Technology, 2007. **56**(1): p. 1-8.

7. Boussu, K., C. Vandecasteele, and B. Van der Bruggen, *Relation between membrane characteristics and performance in nanofiltration.* Journal of Membrane Science, 2008. **310**(1-2): p. 51-65.

8. Luo, M.L., J.Q. Zhao, W. Tang, and C.S. Pu, *Hydrophilic modification of poly(ether sulfone) ultrafiltration membrane surface by self-assembly of TiO₂ nanoparticles.* Applied Surface Science, 2005. **249**(1-4): p. 76-84.

9. Lind, M.L., A.K. Ghosh, A. Jawor, X. Huang, W. Hou, Y. Yang, and E.M. Hoek, *Influence of zeolite crystal size on zeolite-polyamide thin film nanocomposite membranes.* Langmuir, 2009. **25**(17): p. 10139-10145.

10. Raj, S.A., S. Rajesh, K. Lakshmi, K.H. Shobana, and D. Mohan, *Effect of functionalisation on polysulfone-based ultrafiltration membranes.* International Journal of Nuclear Desalination, 2010. **4**(1): p. 18-27.

11.   Steen, M.L., A.C. Jordan, and E.R. Fisher, *Hydrophilic modification of polymeric membranes by low temperature H$_2$O plasma treatment.* Journal of Membrane Science, 2002. **204**(1-2): p. 341-357.

12.   Gilron, J., S. Belfer, P. Väisänen, and M. Nyström, *Effects of surface modification on antifouling and performance properties of reverse osmosis membranes.* Desalination, 2001. **140**(2): p. 167-179.

13.   Maximous, N., G. Nakhla, W. Wan, and K. Wong, *Preparation, characterization and performance of Al2O3/PES membrane for wastewater filtration.* Journal of Membrane Science, 2009. **341**(1-2): p. 67-75.

14.   Maximous, N., G. Nakhla, W. Wan, and K. Wong, *Performance of a novel ZrO$_2$/PES membrane for wastewater filtration.* Journal of Membrane Science, 2010. **352**(1-2): p. 222-230.

15.   Benotti, M.J., R.A. Trenholm, B.J. Vanderford, J.C. Holady, B.D. Stanford, and S.A. Snyder, *Pharmaceuticals and endocrine disrupting compounds in U.S. drinking water.* Environmental Science and Technology, 2009. **43**(3): p. 597-603.

16.   Bolong, N., A.F. Ismail, M.R. Salim, and T. Matsuura, *A review of the effects of emerging contaminants in wastewater and options for their removal.* Desalination, 2009. **238**(1-3): p. 229-246.

17.   Greenlee, L.F., D.F. Lawler, B.D. Freeman, B. Marrot, and P. Moulin, *Reverse osmosis desalination: water sources, technology, and today's challenges.* Water Res, 2009. **43**(9): p. 2317-2348.

18.   Alberti, G., M. Casciola, M. Pica, and G. Di Cesare, *Preparation of nano-structured polymeric proton conducting membranes for use in fuel cells.* Ann N Y Acad Sci, 2003. **984**: p. 208-225.

19.   Nayak, R.K., R. Padhye, L. Arnold, and B.K. Behera, *The promising future of Polymer nanocomposites.* Textile Asia, 2010. **41**(2-3): p. 25-29.

20.   Kim, S.-Y.K.S.H.K.S.S., *Hybrid Organic Inorganic Reverse Osmosis (RO) Membrane for Bactericidal Anti-Fouling Preparation and Characterization of TiO$_2$ Nanoparticle Self-Assembled Aromatic Polyamide Thin-Film-Composite (TFC) Membrane.* Environmental Science & Technology, 2001. **35**(11).

21.   Rahimpour, A., S.S. Madaeni, A. Shockravi, and S. Ghorbani, *Preparation and characterization of hydrophile nano-porous polyethersulfone membranes using synthesized poly(sulfoxide-amide) as additive in the casting solution.* Journal of Membrane Science, 2009. **334**(1-2): p. 64-73.

22.   Blanco, J.F., Q.T. Nguyen, and P. Schaetzel, *Novel hydrophilic membrane materials: Sulfonated polyethersulfone Cardo.* Journal of Membrane Science, 2001. **186**(2): p. 267-279.

23.   Gullinkala, T. and I. Escobar, *Study of the hydrophilic-Enhanced ultrafiltration membrane.* Environmental Progress, 2008. **27**(2): p. 210-217.

24.   Choi, H., S.R. Al-Abed, D.D. Dionysiou, E. Stathatos, and P. Lianos, *Chapter 8 TiO₂-Based Advanced Oxidation Nanotechnologies for Water Purification and Reuse*. 2010. p. 229-254.

25.   Mansourpanah, Y., S.S. Madaeni, A. Rahimpour, A. Farhadian, and A.H. Taheri, *Formation of appropriate sites on nanofiltration membrane surface for binding TiO₂ photo-catalyst: Performance, characterization and fouling-resistant capability.* Journal of Membrane Science, 2009. **330**(1-2): p. 297-306.

26.   Bai, S., A.C. Mo, S.Q. Xian, Y. Zuo, Y.B. Li, and W. Xu, *[Characterization and antibacterial effect of Ag-nHA-nTiO2/polyamide 66 nanocomposite membrane on oral bacteria]*. Hua Xi Kou Qiang Yi Xue Za Zhi, 2008. **26**(4): p. 358-361.

27.   Kwak, S.Y., S.H. Kim, and S.S. Kim, *Hybrid organic/inorganic reverse osmosis (RO) membrane for bactericidal anti-fouling. 1. Preparation and characterization of TiO2 nanoparticle self-assembled aromatic polyamide thin-film-composite (TFC) membrane.* Environ Sci Technol, 2001. **35**(11): p. 2388-2394.

28.   Kim, S.H., S.-Y. Kwak, B.-H. Sohn, and T.H. Park, *Design of TiO$_2$ nanoparticle self-assembled aromatic polyamide thin-film-composite (TFC) membrane as an approach to solve biofouling problem.* Journal of Membrane Science, 2003. **211**(1): p. 157-165.

29.   Bae, C., Y. Yoon, W.S. Yoon, J. Moon, J. Kim, and H. Shin, *Hierarchical titania nanotubes with self-branched crystalline nanorods.* ACS Appl Mater Interfaces, 2010. **2**(6): p. 1581-1587.

30.   Ouyang, M., R. Bai, Q. Chen, M. Wang, and H.Z. Chen, *Fabrication of a novel copper phthalocyanine/titania nanocomposite film and its photoconductive properties.* Gongneng Cailiao/Journal of Functional Materials, 2008. **39**(3): p. 503-506.

31.   Rao, C.N., S.R. Vivekchand, K. Biswas, and A. Govindaraj, *Synthesis of inorganic nanomaterials.* Dalton Trans, 2007(34): p. 3728-3749.

32.   Agnus, G., A. Filoramo, S. Lenfant, D. Vuillaume, J.P. Bourgoin, and V. Derycke, *High-Speed Programming of Nanowire-Gated Carbon-Nanotube Memory Devices.* Small, 2010.

33.   Pang, C., B. Yan, L. Liao, B. Liu, Z. Zheng, T. Wu, H. Sun, and T. Yu, *Synthesis, characterization and opto-electrical properties of ternary Zn($_2$)SnO($_4$) nanowires.* Nanotechnology, 2010. **21**(46): p. 465706.

34.   Wang, H., J.C. Wu, Y. Shen, G. Li, Z. Zhang, G. Xing, D. Guo, D. Wang, Z. Dong, and T. Wu, *CrSi($_2$) Hexagonal Nanowebs.* J Am Chem Soc, 2010.

35.	Chen, J.T., M. Zhang, L. Yang, M. Collins, J. Parks, A. Avallone, and T.P. Russell, *Templated nanostructured PS-b-PEO nanotubes.* Journal of Polymer Science, Part B: Polymer Physics, 2007. **45**(20): p. 2912-2917.

Chapter 8

8 Conclusions, and Recommendations for Future work

This research used a sol-gel method catalyzed by acetic acid in supercritical CO_2 to prepare highly active metal oxide nanowires with high aspect ratios and surface areas that contributed to their inproved photocatalytic activities. The advantage of this preparation method is simplicity and scalability to produce larger quantities of nanowires without the use of harmful solvents.

A novel selective method was presented to produce copper (I) titania nanowires using supercritical CO_2 ($scCO_2$) synthesis methodology suitable for hydrogen production using a sacrificial agent. The doped titania nanowires were prepared using a unique sol-gel methodology in $scCO_2$ using titanium alkoxide, metal dopant, and acetic acid as the polycondensation agent. This sol-gel methodology produced uniformly dispersed dopants integrated into nanowires having diameters of 80 -100 nm and aspect ratios from 15-25 as observed by SEM. XPS and XANES results confirmed a single oxidation state of Cu (I). The photocatalytic activity of the prepared nanowires was tested using formaldehyde as a sacrificial agent for hydrogen production in water under solar light irradiation (100 mW/cm^2). The copper doped titania showed superior performance for hydrogen production of about 10 times compared to Degussa P25, and out 47 times compare to undoped titanium dioxide nanowires. The results are attributed to the Cu (I) oxidation state and high aspect ratio nanowires and providing access to active sites for reactions due to higher dopant dispersion.

Using indium acetate and titanium isopropoxide as precursors for sol-gel synthesis in supercritical CO_2 resulted in high aspect ratio and high surface areas of indium titanate nanowires that has more than double the surface area of P25. The methodology produced uniformly dispersed dopants integrated into nanowires was confirmed by EDS and TEM images. XPS results confirmed formation of indium doping and its oxidation state. The Dye Sensitized Solar Cells (DSSC) performance under solar light irradiation (100

mW/cm^2) was evaluated using different levels of indium doping. At 1 atomic % indium with respect to Ti, photoelectric current was double and DSSC efficiency was improved by a factor of 2.5 times compared to pristine titanium nanowires as a result of indium doping into these nanowires. Sacrifical hydrogen production under solar light irradiation (100 mW/cm^2) was also evaluated using different indium doped titania nanowires. Indium doping at 1.0 atomic % showed improved hydrogen production which was 5.7 and 26 times higher than that produced by commercially P25 and undoped TiO_2 nanowires, respectively.

The bismuth titanate nanowires were prepared using a unique sol-gel methodology in supercritical CO_2 using titanium alkoxide, bismuth acetate, and acetic acid as the polycondensation agent. The methodology produced uniformly dispersed dopants integrated into nanowires with diameters of 80 -100 nm and aspect ratio from 15-25 as observed by SEM. XPS results confirmed formation of bismuth titanate nanowires and their levels of bismuth doping. The Dye Sensitized Solar Cells (DSSC) performance under solar light irradiation (100 mW/cm^2) was evaluated using different levels of bismuth. Bismuth doping level of 1.4 mol % with respect to Ti showed superior performance 1.5, 7.5 times higher efficiency compared to P25 and undoped TiO_2 nanowires, respectively. In addition, the produced photocurrent was 1.5 and 5.5 times higher than that produced by P25 and pristine titanium nanowires. These results confirm the added advantage of bismuth into these nanowires by enhancing visible light harvesting and electron-hole reduced recombination. Sacrifical hydrogen production under solar light irradiation (100 mW/cm^2) was also evaluated using different mol% bismuth doped titania nanowires. Bismuth doping at 1.4 mol % produced 8 times more hydrogen than P25 photocatalyst and 40 times more hydrogen compared to undoped Ti nanowires. These results are attributed to enhanced visible light harvesting and reduced electron-hole recombination. Contrary to the other studies, this study reports for the first time that bismuth titanate is capable of photocatalytic hydrogen production without noble metal or transition metals doping. This work showed that doping titanium nanowires enhanced their performance as photocatalyst or active photoanode for solar cells. However, the enhancement level depends on the type of dopant and its doping concentration as shown in this research.

Furthuermore, four polysulfone were synthesized using condensation polymerization to be utilized in photocatalytic membrane reactor using these metal oxide nanowires. The focus was to create a strong backbone polymer with carboxylic functional groups for titanium dioxide nanowires to coordinate to. The formed polysulfone polymer from reaction of 2-[Bis(4-hydroxyphenyl)methyl] benzoic acid with bis(4-chlorophenyl) sulfone produced high molecular weight that makes it an excellent material with high mechanical strength for further development in photocatalytic membrane reactor.

To summarize this research work, copper, indium and bismuth doping in general improved hydrogen production and DSSC performance at optimized metal doing concentration compared to undoped TiO_2 nanowires prepared using the same approach. In addition, utilizing sol-gel $ScCO_2$ enabled sucessful synthesis of nanowires with high aspect ratios and high surface areas as it improved dispersion of precursors and prevented collapse of formed nanostructures. Figure 8-1 compares the three metals doping improvements over undoped TiO_2 nanowires for both hydrogen production and solar cell performance. However, bismuth doping would be an excellent choice for DSSC application and copper (I) metal doping would be for hydrogen application.

Future work should focus on exploring the synthesis and applications of trimetallic nanowires using sol-gel in supercritical CO_2, which can provide a unique combination of metal oxides at different levels to have a wide range of photocatalysts for applications such as hydrogen production, remediation of contaminated water streams, industrial wastewater, battery applications by using trimetallic lithium based nanowires, electrothermal nanomaterials, and dye sensitized solar cell. In addition, more detailed studies need to be undertaken to understand the mechanism of metal oxide nanowire formation. In addition, although the presented methodology is scalable, detailed reaction engineering studies are required to show how to scale-up this methodology and demonstrate it using continuous reactor processes.
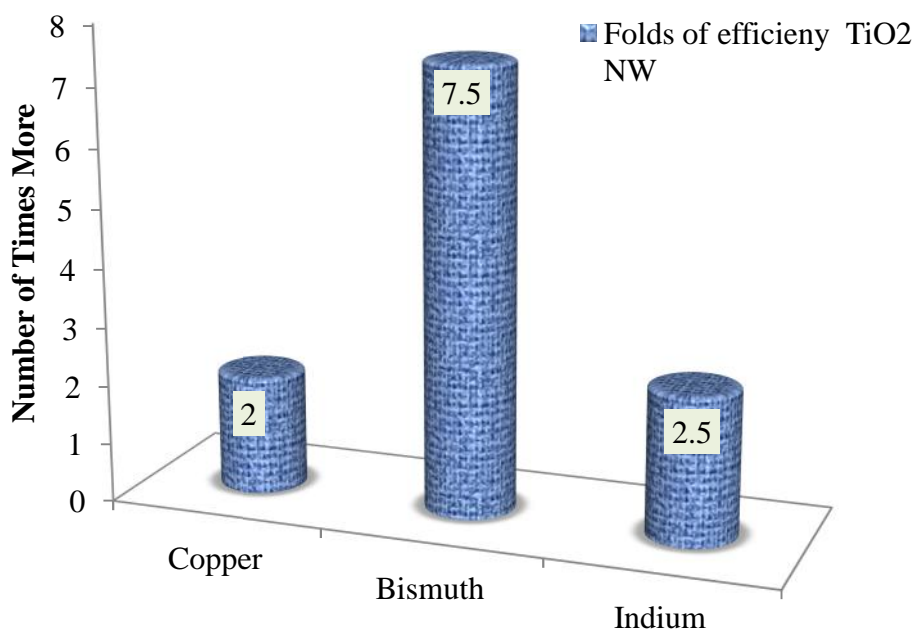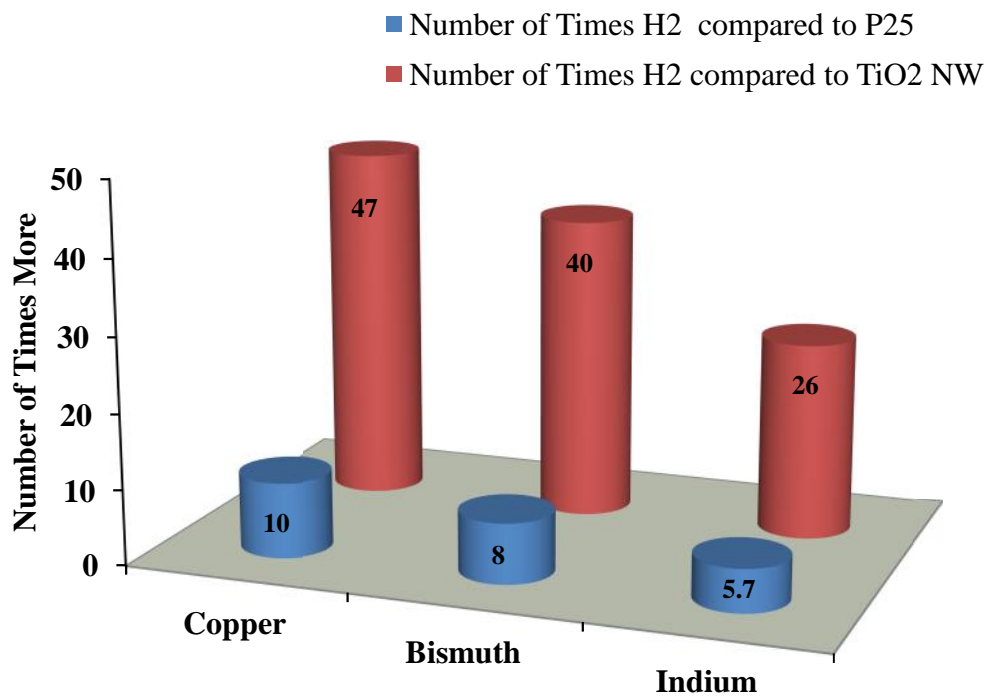
Figure 8-1: Shows the number of folds of hydrogen produced of the three different metal doping into nanowires compared to commercial P25 and undoped TiO_2 nanowires (a) and folds of efficiency of DSSC compared to undoped TiO_2 nanowires.

Appendices

Appendix A: Copyright release

![Copyright Clearance Center logo] **Welcome, Qasem**
Not you?

Log out | Cart (0) | Manage Account | Feedback | Help | Live Help

Get Permission / Find Title

Publication Title or ISBN/ISSN   Go

Advanced Search Options

Order History

View Orders   View Order Details   View RIGHTSLINK Orders

View: Completed | Pending | Canceled | Credited | Denied

Sort orders by: Order Date ▾   ○ Ascending   ● Descending

LICENSE #: 3842831338861
Order Date: 04/05/2016

Journal of Polymer Science Part B: Polymer Physics

Title: Templated nanostructured PS-b-PEO nanotubes
Type of use: Dissertation/Thesis

View printable order   **Fee:** 0.00 CAD

LICENSE #: 3842831181303
Order Date: 04/05/2016

Polymer Journal

Title: Nanocables Prepared from Polyamide 66 nanotubes Enveloping Pt nanowires by a Secondary-template Method
Type of use: reuse in a dissertation / thesis

View printable order   **Fee:** 0.00 CAD

LICENSE #: 3842821241945
Order Date: 04/05/2016

European Polymer Journal

Title: Comparison of redox initiated graft polymerisation and sulfonation for hydrophilisation of polyethersulfone nanofiltration membranes
Type of use: reuse in a thesis/dissertation

View printable order   **Fee:** 0.00 CAD

LICENSE #: 3842821049042
Order Date: 04/05/2016

Journal of Membrane Science

Title: New UV-photografted nanofiltration membranes for the treatment of colored textile dye effluents
Type of use: reuse in a thesis/dissertation

View printable order   **Fee:** 0.00 CAD

LICENSE #: 3791611011344
Order Date: 01/17/2016

Catalysis Today

Title: A review on TiO2-based nanotubes synthesized via hydrothermal method: Formation mechanism, structure modification, and photocatalytic applications
Type of use: reuse in a thesis/dissertation

View printable order   **Fee:** 0.00 CAD

LICENSE #: 3790980025128
Order Date: 01/16/2016

Journal of Photochemistry and Photobiology A: Chemistry

Title: Direct growth of F-doped TiO2 particulate thin films with high photocatalytic activity for environmental applications
Type of use: reuse in a thesis/dissertation

View printable order   **Fee:** 0.00 CAD

LICENSE #: 3790971400442
Order Date: 01/16/2016

Powder Technology

Title: Combustion synthesis of TiO2 nanoparticles as photocatalyst
Type of use: reuse in a thesis/dissertation

View printable order   **Fee:** 0.00 CAD

LICENSE #: 3790940009206
Order Date: 01/16/2016

Journal of Environmental Sciences

Title: Review of the progress in preparing nano TiO2: An important environmental engineering material

Fee: 0.00 CAD

View printable order | **Type of use:** reuse in a thesis/dissertation

---

LICENSE #: 3740501341961
Order Date: 11/01/2015

Physical Chemistry Chemical Physics

Title: CuOx–TiO2 junction: what is the active component for photocatalytic H2 production?
Type of use: Thesis/Dissertation   **Fee:** 0.00 CAD

View printable order

LICENSE #: 3740470559076
Order Date: 11/01/2015

Nanoscale

Title: Non-noble metal Cu-loaded TiO2 for enhanced photocatalytic H2 production
Type of use: Thesis/Dissertation   **Fee:** 0.00 CAD

View printable order

LICENSE #: 3410940705601
Order Date: 06/16/2014

Surface Science

Title: "In situ" XPS study of band structures at Cu2O/TiO2heterojunctions interface   **Fee:** 0.00 USD
Type of use: reuse in a journal/magazine

View printable order

About Us | Privacy Policy | Terms & Conditions | Pay an Invoice

Copyright 2016 Copyright Clearance Center

Curriculum Vitae

Name: Qasem Alsharari

Post-secondary Education and Degrees:

KFUPM
Dharan, Saudi Arabia
1997, BSc. Industrial Chemistry

KFUPM
Dhahran, Saudi Arabia
2007, MSc. Environmental Sciences

The University of Western Ontario
London, Ontario, Canada
2016 , Ph.D.

Honours and Awards:

Saudi Aramco Scholarship
1993-1997, 2005-2007

Ministry of Higher Education, Saudi Arabia
Doctoral scholarship
2009-2014

Related Work Experience

Teaching Assistant
The University of Western Ontario
2010-2013

Quality Manager, Saudi Aramco Refinery
Senior Lab Scientist, RT Laboratory
1997-2008